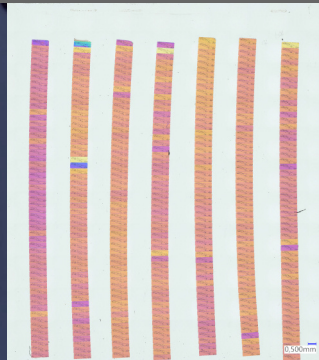


Julian Hoffmann

Automation of section acquisition for Array Tomography

Dissertation



Impressum

Autor / Author : Julian Hoffmann

1. Auflage / 1st edition

2023 Karlsruhe

DOI: 10.5445/IR/1000154925



This document is licensed under a Creative Commons Attribution-ShareAlike 4.0 International License (CC BY-SA 4.0):
<https://creativecommons.org/licenses/by-sa/4.0/deed.en>

Automation of section acquisition for Array Tomography

Zur Erlangung des akademischen Grades eines

**DOKTORS DER INGENIEURWISSENSCHAFTEN
(Dr.-Ing.)**

bei der KIT-Fakultät für Maschinenbau des Karlsruher Instituts für Technologie
(KIT)

angenommene

DISSERTATION

von

M.Sc. Julian Hoffmann

Tag der mündlichen Prüfung:

22.06.2022

Hauptreferent:

Prof. Dr. Veit Hagenmeyer

Korreferent:

Prof. Dr. Rasmus Schröder

Kurzfassung

Array Tomography hat großes Potential, um die dreidimensionale Struktur von Proben bis zu Nanometer Größenordnungen aufzulösen. Dabei wird eine Probe mechanisch geschnitten um so innen liegende Strukturen freizulegen. Die Schnitte schwimmen zunächst auf einer Wasseroberfläche und werden dann auf starren Substraten zur Bildaufnahme abgelegt. Die Flexibilität und Vielseitigkeit der zur Verfügung stehenden bildgebenden Verfahren ist einzigartig für Array Tomography. Zur Zeit wird eine intensive Nutzung jedoch durch den hohen Arbeitsaufwand und Anspruch an die Bedienung eingeschränkt. Existierende maschinelle Systeme zur Schnittaufnahme schränken entweder die zur Verfügung stehenden Bildgebungsverfahren oder das Probenvolumen ein.

In dieser Dissertation wird ein maschinelles Verfahren zur Schnittaufnahme vorgestellt, welches die gleiche Flexibilität und Vielseitigkeit ermöglicht wie die konventionelle manuelle Schnittaufnahme. Fluidkanäle bilden ein mikrofluidisches System mit geringer Reynolds Nummer, in dem sich Schnitte und Substrat gemeinsam bewegen. Die Fluidkanäle formen sich auf der Substratoberfläche durch eine lokale Modifikation der Benetzbarkeit. Die Oberflächenfunktionalisierung wird durch Abscheiden einer hydrophoben Beschichtung und anschließender Plasmastrukturierung erreicht. Das neu entwickelte System umfasst eine maschinelle Probenausrichtung, Schnittaufnahme und Schnittüberwachung. Die Schnitte können auf den für Array Tomography üblichen Substraten abgelegt und somit mit einer Vielzahl von mikroskopischen Verfahren untersucht werden. Durch die maschinelle Schnittaufnahme können große Volumen effizient geschnitten werden, wodurch die Anwendung der Array Tomography in neuen Forschungsgebieten möglich wird. Die maschinelle Schnittaufnahme ist an zwei repräsentativen Proben mit jeweils 1000 Schnitten validiert.

Abstract

Array Tomography has a great potential to enable the three dimensional structural reconstruction of samples across many length scales down to nanometer resolution. In Array Tomography a sample is mechanically sliced in ultra-thin sections to expose the inner structures. In the conventional process the sections are freely floating on a water surface and collected on solid substrates for imaging. The flexibility and versatility of imaging modalities in Array Tomography provide a key advantage in scientific research. Currently the amount of work and skill level to acquire large numbers of sections from extensive volumes limit the application of conventional manual Array Tomography to further research fields. Machine-based section acquisition systems are available or have been proposed but each system either restricts the possible imaging modalities or the sectionable volume.

This dissertation demonstrates a machine-based section acquisition system that offers the same versatility as the conventional Array Tomography workflow. Fluid channels are employed, that form in combination with the floating sections a microfluidic system with a low Reynolds number in which substrate and sections move in unison. The fluid channels are formed on the substrate surface by a site-selective modification of wettability. The surface functionalization is performed by chemical vapour deposition of a hydrophobic coating and plasma induced structuring. The newly developed system includes a machine-based sample alignment, section collection and section monitoring. The system collects sections on common substrates that offer the same versatile imaging modalities as conventional Array Tomography. Sections of large sample volumes are acquired efficiently which opens new fields of research where Array Tomography can be applied. The machine-based acquisition is validated on two representative samples from which each more than 1000 sections were obtained.

Preface

To date the largest dense synaptic reconstruction of brain tissue covers a volume of $96\ \mu\text{m} \times 96\ \mu\text{m} \times 64\ \mu\text{m}$. It is clear that this volume does not suffice to reconstruct the long synaptic connections in more complex and bigger organisms [1]. During this dissertation an important person in my life was diagnosed with Alzheimer's, a brain disease which is still largely not understood by science. My great hope is that the work on new tools to study our environment will help to improve the life of people that still suffer from diseases without any known therapy. Reaching for bigger volumes in Array Tomography bears many challenges. Starting from the growing imaging time, which requires modified microscopes, to the storage and automated processing of the acquired data. This dissertation concerns itself with sample section acquisition prior to imaging. Although this step seems trivial, because it "simply" involves slicing and collection of sample sections, the challenges arise from the necessarily incredibly thin section thickness. Improvements and automation of the section acquisition step have been subject of many scientific studies. This dissertation hopes to enable a step towards larger volumes and new fields of application for Array Tomography.

Acknowledgements

Throughout this dissertation I received a great deal of support and assistance. First I would like to express my sincere thanks to Prof. Dr. Veit Hagenmeyer for enabling me to follow my ambition for this dissertation project. I especially thank my supervisor, Dr. Ulrich Gengenbach, for his insightful feedback which pushed me to sharpen my thinking and provided motivation on dark days. My thanks also go to Andreas Hofmann for his expertise in micro manipulation devices, to Liyu Huang for picking up on the project and assisting in the lab, to Daniel Moser for manufacturing and consultancy on mechanical design, to Klaus-Martin Reichert for the help with the lab infrastructure, to Dr. Martin Ungerer and Peter Stiller for your help and enjoyable discussions – also to the students who contributed to this project especially Sofia Madrigal, Joscha Erbis and Philipp Schmidt. Working with you was fun and provided stimulating conversations as well as happy distractions.

I would like to thank the University of Heidelberg, especially Prof. Dr. Rasmus Schröder and Dr. Irene Wacker for their comprehensive knowledge in the field of imaging and sample preparation. I would like to extend my thanks to Lisa Veit and Ronald Curticean for their expertise and assistance at the microscopes. The KIT Institute for Functional Interfaces (IFG) in the form of Dr. Hartmut Gliemann and Dr. Alexander Welle for their consultancy on surface functionalization. The company RMC Boeckeler for providing an ultramicrotome and assistance on the ultramicrotomy process, as well as Helmut Gnägi and Stefan Schöffberger for the customized diamond knives and Ian Lamswood for his feedback. I acknowledge funding by the KIT technology transfer fund and the program material systems engineering of the Helmholtz association and in that regard I also thank Dr. Rainer Körber.

In addition, I would like to thank my parents for their support throughout my life. In particular my mother for always believing in me. Finally, I could not have completed this dissertation without the support of my friends and family. Especially I thank my girlfriend for all her love and support.

Contents

Kurzfassung	i
Abstract	iii
Preface	v
Acknowledgements	vii
Acronyms and symbols	xiii
1 Introduction	1
1.1 Introduction to Array Tomography	2
1.2 Distinguishing Features from other High Resolution Tomography Methods	7
1.3 Motivation	10
1.4 Objective	12
2 State of the art	15
2.1 Conventional Section Acquisition for Array Tomography	16
2.1.1 Instrument and Tools	16
2.1.2 Sample Trimming	18
2.1.3 Manual Sample Alignment & Advance	19
2.1.4 Sectioning	21
2.1.5 Manual Serial Section Collection	26
2.1.6 Manual Section Monitoring	30
2.2 Automated Solutions for Serial Section Acquisition	33
2.2.1 Automated Collection on Tape – ATUMTome	33

2.2.2	ARTOS 3D	34
2.3	Solution Space for Machine-based Section Acquisition	37
2.3.1	Sample Advance and Alignment	37
2.3.2	Section Collection	39
2.3.3	Section Monitoring	43
3	Methodology	47
3.1	Machine-based Sample Advance	48
3.2	Machine-based Serial Section Collection	54
3.2.1	Model of the Channel Wetting	58
3.2.2	Description of the Fluid Mechanics inside Water Channels	68
3.2.3	Fluid Evaporation	70
3.2.4	Site-selective Modification of Wettability	74
3.3	Machine-based Section Monitoring	77
4	Results & Discussion	87
4.1	Integrated System for Machine-based Section Acquisition	88
4.1.1	Machine-based Sample Advance	92
4.1.2	Machine-based Serial Section Collection	99
4.1.3	Machine-based Section Monitoring	104
4.2	Section Deposition Results – Case Studies	108
4.3	Conclusion	114
4.4	Outlook	115
	List of Figures	119
	List of Tables	127
	Bibliography	129
	List of Publications	145
	Journal articles	145
	Patents	145
A	Appendix	149
A.1	Preparation of the sample block	149

A.2	Ribbon Curvature	153
A.3	Evaporation Model	154
A.4	Software Architecture and System components	157

Acronyms and symbols

Acronyms

AT	Array Tomography
AT – TEM	Array Tomography on TEM grids
CAT	Correlative Array Tomography
CVD	Chemical Vapor Deposition
EM	Electron Microscopy
FDTS	Perfluorodecyltrichlorosilane
FEP	Tetrafluorethylen-Hexafluorpropylen-Copolymer
FFF	Fused Filament Fabrication
FM	Fluorescence Microscopy
FIB – SEM	Focused Ion Beam Scanning Electron Microscopy
LM	Light Microscopy
PCB	Printed Circuit Board
PLA	Polylactic acid
PSF	Point Spread Function
ROI	Region Of Interest
SBF – SEM	Serial Block-Face Scanning Electron Microscopy
SFE	Surface Free Energy
STORM	Stochastic Optical Reconstruction Microscopy
STEM	Stimulated Emission Depletion Microscopy
ssTEM	Serial-Section Transmission Electron Microscopy

Symbols and variables

φ_o	Optics angle
φ_c	Clearance angle
d	Sample distance to cutting plane
w	Width of illuminated band
ϵ_c	Camera rotation angle
ϵ_k	Knife rotation angle
η_0	Feature rotation
N	Discrete image shifts
n	Interpolated image shifts
b	Width of image
l	Lobe width of Gauss model
h_c	Channel height
w_c	Channel width
l_c	Channel length
r_c	Channel radius
w_o	Channel opening width
l_o	Channel opening length
h_i	Immersion depth
A_c	Channel cross section area
V_c	Channel volume
S_c	Channel surface area
L	Characteristic length
γ	Surface tension
ρ	Density
θ	Contact angle
Δp	Pressure difference

r_1, r_2	Principal radii of curvature
k_1, k_2	Principal curvature
H_f	Mean curvature
Re	Reynolds number
μ	Dynamic viscosity
G	Evaporation rate
p_v	Vapor pressure
M	Molar mass
t_e	Evaporation time
T	Temperature
z	Length of liquid/air interface
v_z	Air flow speed
I	Irradiance
R	Reflection
α	Angle of incidence
β	Angle of refraction
λ	Wavelength
h	Section thickness
δ	Optical path difference
φ	Phase shift
ΔE	Perceived color difference
p_0, p_1, p_2	Interference model parameters

Physical and Material Constants

Physical Constants

g Free-fall acceleration at ground level : $9.81 \frac{\text{m}}{\text{s}^2}$ [2]

Water properties

M_{water} Molar mass : $18 \frac{\text{g}}{\text{mol}}$ [2]

γ_{water} Surface tension at 20 °C : $72.75 \times 10^{-3} \frac{\text{N}}{\text{m}}$ [2]

ρ_{water} Density at 20 °C : $998.2 \frac{\text{kg}}{\text{m}^3}$ [2]

n_{water} Refractive index at 20 °C : 1.333 [2]

μ_{water} Dynamic viscosity at 20 °C : $1 \frac{\text{kg}}{\text{m s}}$ [2]

$v_{p,water}$ Vapor pressure at 20 °C : 2.34 kPa [2]

Ethylene glycol properties

M_{glycol} Molar mass of ethylene glycol : $62 \frac{\text{g}}{\text{mol}}$ [2]

ρ_{glycol} Density at 20 °C : $1113.5 \frac{\text{kg}}{\text{m}^3}$ [2]

γ_{glycol} Surface tension at 25 °C : $48.02 \times 10^{-3} \frac{\text{N}}{\text{m}}$ [2]

$v_{p,glycol}$ Vapor pressure at 25 °C : 0.01 kPa [2]

FDTS properties

θ_{FDTS} Contact angle of water on FDTS coating : 116° [3]

1 Introduction

This dissertation presents a novel machine-based section acquisition for the Array Tomography (AT) workflow. Tomography methods have a wide field of application from material science to life science. Tomography methods in general describe a volume by acquiring image sections of the sample. The acquired image sections are aligned and stacked to provide a three-dimensional representation of the sample. Array Tomography visualizes the three-dimensional ultrastructure in samples, which is below the Abbe resolution limit of standard optical microscopes. Through a mechanical slicing process the inner structure of samples is made accessible to high resolution imaging modalities.

Section 1.1 of this chapter provides an introduction to the origins, applications and characteristics of Array Tomography. The second Section 1.2 compares Array Tomography to other high resolution tomography methods. Section 1.3 covers the motivation for further automation and shortly describes the section handling problem which is a key challenge. Section 1.4 describes the objectives in more detail and how the presented machine-based section acquisition is distinct from previous approaches.

The structure of the introduction follows the overall structure of the dissertation and references to chapters which discuss topics in more detail. Chapter 2 covers the available and proposed solutions for the section acquisition in Array Tomography. The developed methods and materials are described in Chapter 3. The last Chapter 4 discusses the results in general as well as exemplary on two case studies and provides an outlook.

1.1 Introduction to Array Tomography

As tomography implies, the focus of Array Tomography is the study of samples in all three dimensions. The terminology refers to an arrangement of serial sample sections in a spatial "array" on a planar solid surface. While "tomography", from ancient Greek "tomos" as "slice" and graphō as "to describe", refers to the reconstruction of a three-dimensional structure from two-dimensional image "slices" [4].

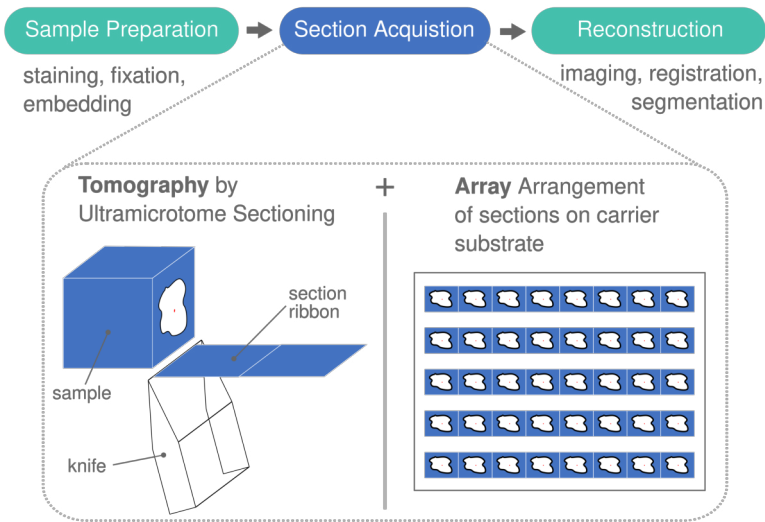


Figure 1.1: Array Tomography process with a schematic depiction of the two characteristic steps. "Tomography" meaning a slicing of the sample and "Array" from the arrangement of the slices in an array on a carrier substrate used for imaging.

Array Tomography originates from ultramicrotomy and is as such a sample preparation method for high resolution imaging. In principle, Array Tomography uses ultramicrotomy to mechanically slice an object into thin sections. Obtained section arrays are imaged and finally recombined to derive a three-dimensional

computer model. The key strength of Array Tomography is its versatility, as it "encompasses light and electron microscopy modalities that offer unparalleled opportunities to explore three-dimensional cellular architectures in extremely fine structural and molecular detail" [4]. The term Array Tomography describes the complete process from sample preparation to acquisition of sections and finally imaging of sections and recombination to a three dimensional model. Figure 1.1 shows the characteristic steps of the section acquisition in the context of the complete Array Tomography process.

Array Tomography was first proposed by Micheva and Smith in 2007 as a new tool to visualize the ultrastructure of neural circuits [5]. The principle is to collect large numbers of serial sections and thus increase the scope for 3D reconstruction compared to previous methods in ultramicrotomy. In order to correctly reconstruct the three dimensional structure from the two dimensional image information of each section, it is important to preserve the sections in the correct order during the acquisition process. The acquisition of large numbers of serial sections is a crucial aspect in Array Tomography and also objective of this dissertation. An overview of existing section acquisition approaches is given in Chapter 2.

The collection of small sets of serial sections on TEM grids for three dimensional reconstruction is well known and referred to as serial-section Transmission Electron Microscopy (ssTEM) [6, 7]. Although Array Tomography might apply to all forms of serial-section microscopy, including ssTEM, the terminology is, according to Smith, restricted "to arrays placed on stable solid substrates such as glass coverslips, flexible tape, or silicon wafers, as opposed to the open grid slots or delicate, ultra-thin electron-transparent support films required for ssTEM imaging" [4].

The samples suitable for Array Tomography range from material science to life science [4, 8]. A certain rigidity of the samples is necessary as the sections are formed through a mechanical slicing process. This often requires a pretreatment and embedding in a support matrix of epoxide resin especially for biological samples. Cutting of very hard samples such as metals and even ceramics is possible [9].

Array Tomography relies on ultramicrotomy as the majority of high resolution imaging methods in Electron Microscopy (EM) or Light Microscopy (LM) only provide structural information from small volumes or – in some cases – only the topmost layer or surface of a sample. In cases where the region of interest is not directly accessible on the surface or the sample is too thick to be penetrated by the selected imaging method, a sample preparation method like ultramicrotomy is required.

Ultramicrotomy makes structures deep in a sample accessible for later imaging by mechanically slicing the sample into sections and preserving them on a carrier substrate. Ultramicrotomy is the branch of microtomy used to obtain ultra-thin sections. The term ultra-thin is not well defined and this dissertation uses the definition of sections with a thickness smaller than 200 nm [7, 10]. The sectioning of the sample is performed with a very sharp physical knife edge. The knife is typically made of a sharp polished diamond having almost atomic thickness and a radius of curvature of 0.8 nm to 1 nm at the edge [10, 7]. The sections have a typical thickness in the range of 50 nm to 200 nm and then expose the before hidden structures on their surface. Ultramicrotomy was first used to prepare samples for Transmission Electron Microscopy (TEM), where ultra-thin sample sections are required that can be penetrated by the electron beam. Nowadays also SEMs are used to image ultra-thin sections. SEMs allow thicker sections as a penetration of the electron beam is no requirement. The imaging benefits however from the fact that electrons can quickly dissipate in the carrier substrate and thus ultra-thin sections of the usually non-conductive sample material prevent charging. The capability of three dimensional reconstruction with native ultramicrotomy is limited as it works with a small set of not necessarily ordered sections deposited on TEM-grids. Details of the sectioning process in ultramicrotomy can be found in Section 2.1.4.

Ultramicrotome sectioning is used in Array Tomography to obtain section ribbons, by successively attaching sections to each other. These section ribbons are floating on a water surface contained by a trough mounted adjacent to the knife. The handling of ribbons is advantageous, as they already contain multiple sections in determined order, which can be manipulated as a unit. For the reasons of

the limited deposition space and work intense handling of TEM grids, solid carrier substrates such as pieces of silicon wafer are used in Array Tomography. Multiple ribbons are arranged in an array like structure and deposited on the carrier substrate, as seen in Figure 1.1. This section acquisition principle defines the term "Array Tomography".

Ultramicrotome sections have a thickness of only a fraction of the wavelength of visible light. This still makes actually transparent sections visible in vibrant colors with conventional microscopes because of light interference. The interference color depends on the section thickness and is used by operators to monitor the sectioning process. A description of these interference colors as a means to interpret the section thickness is given in Section 2.1.6. A picture of section ribbons with different interference colors floating in the water trough of a knife is shown in Figure 1.2.

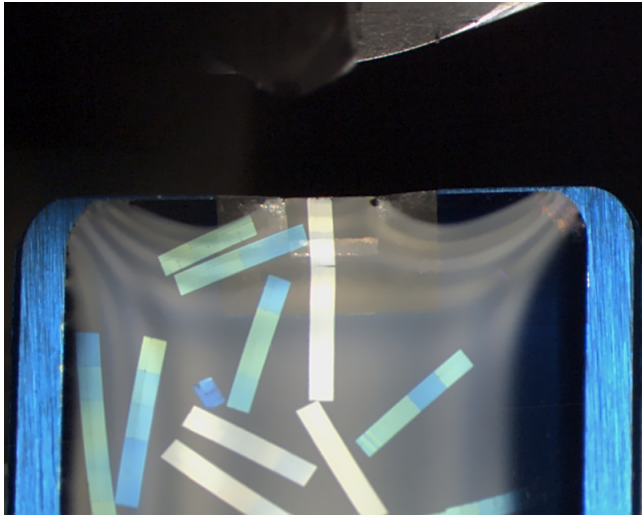


Figure 1.2: Picture taken through the microscope of an ultramicrotome. The picture shows freely floating sections in the water trough of an ultramicrotome knife. Blue interference colors occur for 200 nm and silverish/golden colors for 80 nm to 100 nm thick sections. The last section ribbon is still attached to the diamond knife. The sections have a width of approx. 800 μm .

After an array of sections is obtained, the section can be imaged on the carrier substrate in subsequent imaging steps on external instruments. The obtained images are aligned, stacked and segmented to generate a three dimensional representation of the sample.

The selection of the carrier substrate defines the applicable imaging modalities. Solid carrier substrates cannot be penetrated by a TEM electron beam, as it is originally used to image ultra-thin sections. Therefore high resolution imaging is often performed by Scanning Electron Microscopy (SEM) for which sections on silicon wafers are well suited. Despite TEM offering the highest electron microscopic resolution, SEM resolution is still adequate for a wide range of scientific applications and a recently developed hybrid variant AT-TEM enables TEM imaging by a film transfer from the solid carrier substrates [4, 11].

Nevertheless it is the versatility of applicable imaging methods, that is a key strength of Array Tomography. Sectioning and imaging are performed on two different instruments with the substrate as a carrier which can be loaded into a variety of microscopes. The sections are preserved on the carrier substrate and thus it is possible to re-image them with different imaging modalities. These modalities can for example also include the application of post slicing staining methods and allow correlative imaging approaches.

Targeting the location and orientation of a desired region of interest is a well known problem in microscopy. The time spent for targeting can be greatly reduced by using Light Microscopy (LM) or Fluorescence Microscopy (FM) to locate the regions of interest inside the sample [12]. The application of multiple imaging techniques on the same sample is sometimes also referred to as Correlative Array Tomography (CAT). Correlative techniques allow for example the targeting of ROIs by fluorescence markers [1], to link functional information derived from fluorescent markers to their structural localization [13] or the combination of complementary information for the segmentation and identification of sample components [14]. Further image modalities include for example the super-resolution imaging of Stochastic Optical Reconstruction Microscopy (STORM) and Stimulated Emission Depletion Microscopy (STED) [15].

The versatility of imaging modalities distinguishes Array Tomography from other highly integrated tomography methods such as Serial Block-Face Scanning Electron Microscopy (SBF-SEM) or Focused Ion Beam Scanning Electron Microscopy (FIB-SEM). This versatility comes to date with a plus in required manual work and expertise of the operators. A comparison of Array Tomography to other high resolution tomography methods is provided in the following Section 1.2.

1.2 Distinguishing Features from other High Resolution Tomography Methods

This section compares Array Tomography to two other well established methods for high resolution three-dimensional reconstruction, Serial Block-Face Scanning Electron Microscopy (SBF-SEM) and Focused Ion Beam Scanning Electron Microscopy (FIB-SEM).

Likewise as for Array Tomography, the study of neural circuits has also been a key interest in the development of SBF-SEM demonstrated by Denk and Horstmann in 2004 [16]. FIB-SEM was first used in the semiconductor industry in the 1980s and later introduced to the study of materials and life science samples [17].

Both methods make inner structures of the sample accessible by successively removing the topmost layer of the sample. A SBF-SEM is basically an ultramicrotome mounted inside a SEM chamber. The diamond knife is used to cut the sample and subsequently exposes deeper structures, while the cut sections are discarded and only the block-face is imaged. A FIB-SEM is a dual beam system, where the ion beam is used to mill a sample and exposes a new cross section. Whereas the electron beam is used to scan the cross sections.

SBF-SEM and FIB-SEM offer highly automated acquisition methods. The acquisition of sample sections in Array Tomography to date is also in machine-based acquisition far less automated and requires supervision. The high integration level of SBF-SEM and FIB-SEM limits however the imaging modalities compared to Array Tomography. Access to the inner sample structures is provided only very

briefly and inside the vacuum chamber of a specialized SEM. In Array Tomography the sections can be imaged in various standalone microscopes which offer light and electron based imaging or spectroscopic methods. In SBF-SEM and FIB-SEM the removed sample material is permanently lost. This prohibits the re-imaging of sample sections with heavy-metal poststaining or immunolabeling for Fluorescence Microscopy, which are established in Array Tomography as the sections are preserved on solid substrates. Array Tomography enables also correlative approaches where the information of differently obtained images is included in the reconstruction [5, 18, 19, 20].

Charging effects due to the electrons not dissipating in a non-conductive sample material can cause problems during the imaging and limit the acquisition speed. The ultra-thin sections on conductive substrates in Array Tomography allow a quick dissipation of introduced charges. Acquired sections can also be imaged in multiple instruments in parallel to further speed up the acquisition process. In SBF-SEM and FIB-SEM sample material remains underneath the surface that is imaged. For non conductive samples a risk of charging during the SEM operation must be addressed by a lower vacuum or increased cycle times [16]. Because of the longer acquisition cycles FIB-SEM and SBF-SEM target smaller volumes for reconstruction compared to Array Tomography [18].

Array Tomography requires that the sample produces well-defined sections when being cut without delamination or destruction of the structures of interest by the mechanical cutting process with a diamond knife. This generally requires that the sample is not too soft and can require sample pre-treatments. Further the sections show a noticeable compression along the cutting direction which must be considered in the reconstruction. In SBF-SEM delamination and compression are a smaller problem as the block face is imaged which provides more structural integrity. In FIB-SEM neither delamination nor mechanical influence of sectioning is present but the ion beam milling causes a thermal influence that may cause sample degeneration. For this reason, sensitive samples must also be fixated, stained and embedded in resin [7, 16, 17].

The thickness of the sample sections defines the z-resolution of the reconstruction. Array Tomography requires the formation of well-defined sections as they are collected for imaging. This limits the z-resolution to 60 nm to 80 nm depending on how well the sample can be sectioned. The z-resolution is better in SBF-SEM, with 20 nm to 25 nm as the block face is imaged and no requirement for well defined sections exists. A nanometer z-resolution is possible with the ion beam milling in FIB-SEM [5, 7, 17, 18].

It is not possible to give a general statement which tomography method is superior. Destructive tomography methods are useful if the sample is difficult to section and sample loss can be tolerated. The high amount of manual work in Array Tomography is justified by the versatile imaging modalities, which are unmatched by destructive methods [4, 5]. A combination of methods such as FIB-SEM on ultramicrotome sections has also been demonstrated [21]. Mainly the large amount of manual work and expertise currently limit the application of Array Tomography in scientific research. Thus, the need for further automation of the serial section acquisition in Array Tomography arises which is the motivation for this dissertation.

Table 1.1: Comparison of the three commonly used tomography techniques used in life and material science

Feature	SBF-SEM	FIB-SEM	AT
Post imaging	not possible	not possible	possible
Mech. influence	less present	none	present
Thermal influence	none	beam damage	none
Depth resolution	20 nm to 25 nm	<10 nm	60 nm
Imaging modalities	SEM	SEM	SEM/LM/FM/...
Integration level	high	high	low
automation	high	high	low

1.3 Motivation

Although Array Tomography is a versatile tool, the achievable results in terms of quality and scope depend significantly on the operator. A high skill level and training is required during the sophisticated steps of instrument setup, section acquisition and process monitoring. The workflow is very demanding, as it requires the operator to focus on the task and muscles need to remain tensed during the extensive manual manipulation tasks in the micrometer range. To master Array Tomography, many years of experience are required and operators with these skills are getting more and more difficult to find. This is the motivation to bring the Array Tomography workflow closer to an automated solution, as the high amount of manual labor to acquire large sets of serial sections to date limits the application as a scientific research tool.

An analogy which is used between ultramicrotommists is helpful in understanding the challenges of Array Tomography by transferring the dimensions into a realm that is easier accessible to intuitive understanding. Acquiring ultramicrotome sections is comparable to ordering loose pages of a book floating on a water surface. The loose book pages resemble the sample sections. The original book holds the information in a similar way, as the sample does prior to the slicing. As with a book, the information of each individual section must be recomposed in the correct order to reconstruct the intrinsic information. The handling is difficult because the cross section provides no rigidity as the lateral dimensions are orders of magnitude bigger compared to the thickness. The surface tension dominates the form of the pages, so by simply picking up the sections, they fold and rupture. To transfer the aspect ratio to the book analogy, with a typical page thickness of 100 μm , the pages would have lateral dimensions of more than three meters. In the world of Array Tomography the section handling is accomplished by a handheld toothpick with an attached eyelash as described in detail in Section 2.1.5. This technique can be compared to trying to arrange the floating book pages through pushing and pulling with a stick. Applying too much pressure will damage the pages. Flow and turbulence of water and air cause already arranged pages to change positions. The arrangement has to be performed for hundreds of pages

without losing track of the correct order. For section acquisition in Array Tomography these tasks are performed with micrometer precision and handheld tools.

It is not just the section acquisition that challenges the operator. During the instrument setup the sample has to be advanced to the knife edge. This also includes a complete alignment of the sample front face, the so called block face, to the virtual cutting plane in all three dimensions. These tasks are performed with sub micrometer precision only by visual interpretation of a light reflection on the sample block face as described in Section 2.1.3. The sectioning process itself is supervised by visual interpretation of the interference colors of the floating sections. The correct thickness and variations in the cutting process must be detected by small and subjective color changes as described in Section 2.1.6.

People having the required skill and calmness to handle these microscopic objects need to undergo excessive training and are difficult to find. Further, the acquisition process is very prone to human error and it is easy to lose single or multiple sections for later reconstruction. Moreover, incorrect operation can easily damage the expensive and fragile diamond knife or the instrument itself. These factors currently limit the application in scientific research despite the unmatched image modalities that Array Tomography offers.

Recently many new methods have been proposed to automate the section acquisition for Array Tomography [4, 22, 23, 24, 25, 26, 27, 28]. Each of the proposed methods has its unique benefits and limitations in terms of reliability, volume and feasibility which are discussed in detail in Section 2.3.2. Bringing together the versatility in available image modalities offered by conventional Array Tomography and a highly automated and reliable section acquisition process to extend the possible applications, is still subject of ongoing research and motivation for this dissertation.

1.4 Objective

Array Tomography offers great potential to enable new scientific insights in the ultrastructure of large volumes. This potential is currently limited by a number of described restrictions that restrain its application. New fields of research can be claimed by making bigger sample volumes accessible for Array Tomography. The objective of this dissertation is to overcome these restrictions and to make the analysis of bigger volumes easily accessible through novel methods and a higher degree of automation. The requirements of an automated solution for Array Tomography are:

- Integration into an existing ultramicrotome.
- Reduction of the skill level required for operation.
- Reduction of operator influence on the section quality.
- Reduction of manual workload.
- Increase of section acquisition reliability.
- Increase of the number of sections that can be acquired economically.
- Prevent damage to the instrument by incorrect operation.
- Enable the automated imaging in microscopes.
- Sustain the versatility of imaging modalities by conventional Array Tomography.

By means of automation the workload on the operator is reduced and the reliability of section acquisition increased. In Array Tomography this requires a new methodology for a machine-based process in the sophisticated steps of:

- Sample alignment and advance (Section 3.1)
- Section acquisition (Section 3.2)
- Section monitoring (Section 3.3)

The new methodology is integrated into an ultramicrotome (Section 4.1) and the performance is evaluated on two case studies where in each more than 1000 sample sections are acquired (Section 4.2).

2 State of the art

The following sections describe and analyse the state of the art in Array Tomography and build the basis for the developed methods and realized system. The chapter begins in Section 2.1 with the conventional Array Tomography workflow proposed by Micheva and Smith which requires extensive manual labor during section acquisition. Tools and modified workflows are presented that support the operator in the manual collection and allow the collection of intermediate sized sets of serial sections (100-1000 sections). The second Section 2.2 presents commercially available solutions for the automated section acquisition. The third Section 2.3 lays down the possible solution space proposed in literature for the section acquisition divided into key tasks.

2.1 Conventional Section Acquisition for Array Tomography

The conventional Section Acquisition for Array Tomography uses ultramicrotome sectioning and employs special section collection techniques to deposit the sections on solid substrates [5]. The ultra-thin sample sections are obtained by ultramicrotome sectioning with a diamond knife. Ultramicrotomy is a sample preparation method that cuts a sample into ultra-thin sections for subsequent, typically electron microscopic, imaging methods. In cases where the region of interest is not directly accessible on the sample surface and the sample is too thick to be penetrated by the selected imaging method, a sample preparation method like ultramicrotomy is required. Microtomy comprises methods for obtaining sections of a sample by cutting. The word originates from ancient greek "micro" as "small" and "tomy" as "to cut". Ultramicrotomy is the branch of microtomy that cuts ultra-thin sections.

2.1.1 Instrument and Tools

In this section a description of the main instrument and the tools for the section acquisition in Array Tomography is provided. An illustration of a setup suitable for Array Tomography is shown in Figure 2.1.

The instrument used to section ultra-thin sections is the ultramicrotome. The working principle of ultramicrotomes is similar to conventional microtomes, with modifications that allow the high precision sample advance required for cutting in the nanometer range. First ultramicrotomes accomplished this advance by a controlled thermal expansion. Today's ultramicrotomes use a cantilever system with precision bearings to allow nanometer feed over up to one millimeter cutting ranges [29].

The sample is mounted in a specimen holder. Specimen holders are changeable and designed to fit the sample dimension. The knife stage sits in front of the

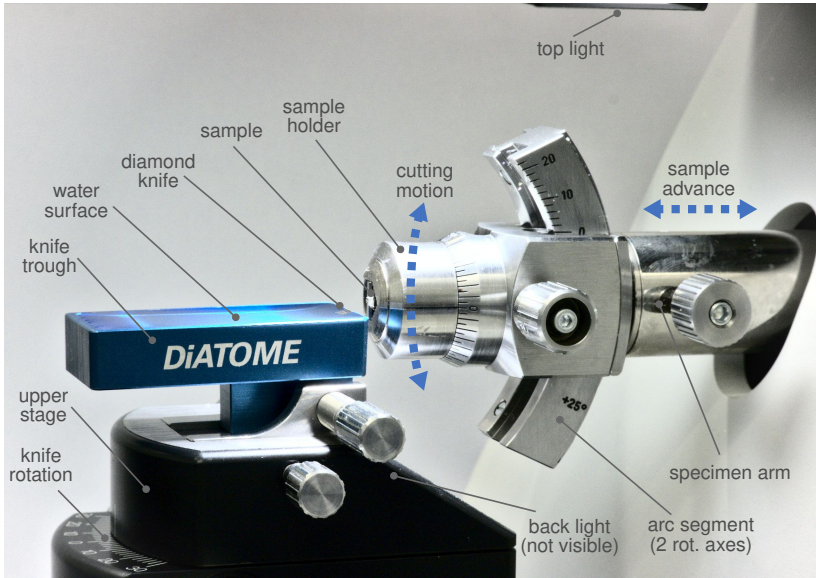


Figure 2.1: Side-view of an ultramicrotome with annotations of the main components. The arm motions are indicated with dashed blue lines.

sample and can be rotated along the vertical axis as well as moved back and forth. The face of the sample block facing towards the knife is called block face and defines the shape of the sections [7]. The specimen holder is affixed to the arc-segment holder. The arc-segment has two rotational axes for sample alignment. The rotational axes include the rotation along the arm axis and the rotation along the axis of the knife edge. These four axes are used to align and advance the block face to the virtual cutting plane of the knife as described in Section 2.1.3. The specimen arm performs the cutting motion and advances the sample. The sectioning is described in more detail in Section 2.1.4. The knife stage holds the sectioning knife and also contains a back light that illuminates the back facet of the knife. The knife consists of a knife trough filled with water and a diamond knife edge used for sectioning. The sections are collected from the water surface inside the knife trough as described in Section 2.1.5.

An established manipulation tool in ultramicrotomy is a thin hair, typically an eyelash, attached to toothpick. The toothpick is handheld and passes the hand motion to a nearly point sized tip of the eyelash. Forces transmitted by physical contact can be adjusted precisely due to the flexibility of the hair. Also the water surface can be manipulated as the hair creates a water meniscus when it comes in contact with the water surface.

To monitor the sectioning process, a top light is fixed above the specimen arm to observe the sections in the reflection on the water surface as described in Section 2.1.6. A stereo microscope is mounted in front of the ultramicrotome facing towards the knife trough and sample holder to magnify the microscopic objects.

2.1.2 Sample Trimming

A small size and suitable shape of the sample block are requirements for a proper sectioning of the sample. To fulfill these requirements, trimming of the sample is necessary. The trimming usually also ensures that the region of interest sits just below the block face, so that it is quickly sectioned.

For Array Tomography the samples are typically embedded in epoxide resin as a formation of ribbons is desired as described in Section 2.1.4. For a smaller block size, the excess resin is usually in a first step trimmed with a razor blade. Then special trimming knives can be used to trim the sample mounted in the ultramicrotome or the trimming can be performed in an external trimming device [7].

Trimming ensures that the sample is centered inside the block face. This is required for the reconstruction and sectioning. A smaller block face generally shows less compression of the sections [7]. An imperfect trimming may also cause damage to the knife edge when sections are being pulled back over the knife edge [7].

For a good sectioning the trimming must ensure that,

- Left and right side of the block are equal in length to form a straight ribbon.
- The block face separates the previous section over the complete length from the knife edge. Therefore lower and upper side of the block face must match.

After a sample is trimmed, the block face can be advanced to the sectioning knife as described in the next Section 2.1.3.

2.1.3 Manual Sample Alignment & Advance

Despite being made of diamond, the fragile knife edge is easily damaged by collisions or the sectioning of too thick sections. This requires, that the sample block face must be aligned and advanced to the virtual cutting plane of the diamond knife before the sectioning starts [7]. For manual alignment and advance a challenging visual interpretation of a reflection is used. The procedure requires multiple iterations and targets a final distance of the sample block face to the virtual cutting plane of less than 1 μm . An operator error during this procedure might cause damage to the expensive diamond knife.

The degrees of freedom in the knife stage and arc-segment allow for alignment correction in three rotational axes and sample advance. The stage contains a back light that illuminates the back facet of the sectioning knife. The operator observes the reflection of the back light on the block face through the stereo microscope. When the inclination of the stereo microscope is correctly set, the reflection of the back light is visible as a band of light. A detailed analysis of the light path is provided in Section 3.1. By manually moving the specimen arm up and down, the operator observes the reflection change. This information is used to stepwise adjust the rotation of each axis to align the block face to the virtual cutting plane.



Figure 2.2: Diffraction colors visible in the vicinity of the knife edge for a diminishing gap between block face and knife edge. The back light is reflected on the block face and passes through the gap between sample and knife edge. The knife edge is slightly misaligned to the sample block face and the decreasing gap creates a rainbow like color pattern. On the left side a blue hue is visible before the light vanishes completely. A gap is still present on the left side but too small to allow light to pass. The correct identification of these reflections can be difficult for operators.

The procedure for block face alignment was described in 1977 by Gorycki [30] in four steps:

1. Aligning the horizontal edges of the block face to the knife edge.
2. Aligning the knife edge parallel to its reflection in the block face.
3. Tilting the arc-segment to make the block face parallel to the direction of sectioning.
4. Bringing the knife edge as close as possible to the aligned block face so that sectioning can begin quickly.

The first three steps need to be repeated multiple times because each correction influences the other adjustments. During the adjustments the sample is manually

advanced repeatedly as precise perception during the first three steps is only possible in proximity to the knife edge, while adjustments require a safe distance. Very fine differences require a narrow gap of less than $1\ \mu\text{m}$ between sample and knife edge to observe diffraction colors as visible in Figure 2.2. With these diffraction colors an alignment and advance with a deviation of less than $1\ \mu\text{m}$ over the complete block face from the cutting plane can be achieved. Identifying necessary corrections to the instrument is the challenge of this technique, especially when multiple alignment errors are present simultaneously. Other structures on the instrument, for example the lower facet on the diamond knife, reflect light as well. This creates multiple reflections on the block face and the operator has to identify the correct reflection of the knife facet.

The remaining distance between block face and cutting plane must be bridged with empty cuts until the knife sections the sample. This distance should be kept as small as possible and the alignment performed as precise as possible. A significant deviation does not only increase the waiting time but also causes a loss of sample material due to incomplete sample sections [7, 30].

2.1.4 Sectioning

After the initial advance of the sample to the cutting plane is completed, the sectioning process can start. The sectioning process removes the first layer of the sample block face with the help of a physical knife edge. In Array Tomography typically diamond knives are used because of their superior sectioning quality. The knife is mounted in a trough filled with water and the sections float on the water surface.

The specimen arm performs the cutting motion and sample advance in the sectioning process. The downward motion is used to cut the sample, while during the upward motion the arm retracts to bring the sample back above the knife. The retract maintains a safe distance to the knife during the upward motion and thus prevents possible damage by a collision. After the arm is moved up, the advance system moves the arm forward by the selected section thickness. When the sample

passes the knife in the following downward motion, a section of the sample is formed by removing the first layer of the sample block. The cutting motion and the sample feed are fully automated, so that the ultramicrotome can perform a series of cuts without user interaction. The arm speed during the sectioning, typically close to $1 \frac{\text{mm}}{\text{s}}$, differs greatly from the speed during the retraction, which can be as high as $100 \frac{\text{mm}}{\text{s}}$ [7, 31]. The instrument performs the speed transition based on a cutting window, which the operator has to set manually and is compared to the encoder position of the specimen arm.

The claimed section thickness in ultramicrotomy lies in the range from 8 nm to 200 nm [7, 32]. For Array Tomography the section thickness determines the z-resolution of the reconstructed model. The section thickness can also influence the imaging process, for example in SEMs thinner sections allow a quicker dissipation of electrons in the carrier substrate. The achievable section thickness is limited by the following factors:

- Compressability and homogeneity of the sample
- Quality of the knife edge
- Thermal stability of the ultramicrotome
- Mechanical precision of the ultramicrotome

For the Array Tomography process it is important to reliably obtain well defined sections. The thinner the section the higher is the risk of an imperfect cut or a delamination of structures inside the sections. Therefore the optimal section thickness in Array Tomography is a compromise between reliability and z-resolution of the reconstruction. A section thickness of 100 nm is typically used [4, 33]. A practical minimal limit is around 60 nm thickness but strongly depending on sample properties [13, 19]. Very inhomogenous or not well embedded samples may require a section thickness of 200 nm to prevent delamination as described in Section 4.2.

Ultramicrotome sections show a variation in thickness due to instrument, process and environment related influences. The thickness variations can be introduced by vibrations, thermal drift, relaxation processes in the sample material, a poor

mounting of the sample, remaining backlash of the system, calibration state of the instrument, sharpness of the knife and incorrect cutting parameters, as too high cutting speed tends to fracture hard samples [7, 34]. The thickness variations are created by a displacement of the knife or sample and can occur in between subsequent sections or within a single section. The variation between sections is typically bigger than the variation within a section [35]. The often periodic thickness variation within sections is referred to as chatter or chatter marks. Chatter marks are perpendicular to the cutting motion and a common problem in mechanical material processing [36, 37]. Variations in the section thickness have a negative impact on the imaging process by influencing the penetration of the electron beam and cause artefacts in obtained images [34]. In Array Tomography, thickness variations between sections cause a distortion during the reconstruction. It is therefore required that the operator monitors the section thickness and takes countermeasures as soon as possible during the sectioning process, such as reducing the cutting speed to minimize possible chatter. Thickness variations can be visibly observed while the sections are still floating on the fluid surface as described in Section 2.1.6.

The sections float on a fluid contained in the knife trough wetting the knife up to the knife edge as displayed in Figure 2.3A. The fluid has two important tasks in the sectioning process:

1. Through capillary forces the fluid forms a thin film on which the section slides away from the knife edge **during sectioning**.
2. The fluid surface acts as a buffer **after sectioning** from which sections are collected onto carrier substrates.

For the trough fluid to assist **during the sectioning** process, the fluid level is a crucial parameter that must be correctly set and continuously controlled. A too high level causes wetting of the block face, as the fluid is picked up by the block face during the sectioning process. A too low level causes improper section formation because the fluid is dewetting on the knife and sections stick on the knife face. Sections need to be removed manually from the knife, as drying of sections on the knife can cause permanent adhesion, which renders the part of

the knife edge inoperable [7]. The optimal fluid level for sectioning is specific to the sample and lies within the extremes of block face wetting and knife edge dewetting. A practice to find the correct fluid level is according to Hayat [7] to overfill the trough and then remove fluid until a slightly negative meniscus forms, but the knife edge does not start dewetting. The sectioning is then performed and the fluid level increased until the sections slide smoothly away from the knife. The level of the trough fluid might decrease through evaporation over time. The fluid level must therefore be monitored by the operator or by an automated fluid level control system [29].

For the trough fluid to act as a buffer for sections **after sectioning**, further properties are important. The fluid's surface tension stretches the sections and thus preserves the shape of the sections. At the same time, the surface tension must be low enough to not rupture the structures within sections. The trough fluid should not wet the section to allow the section to float on the surface.

Hayat [7] describes the most desirable characteristics of the trough fluid as that it should:

- Not damage the sample
- Easily wet the knife up to the knife edge
- Act as a release agent and separate the section from the knife facet
- Reduce the force necessary to move the section away from the knife edge
- Absorb the heat generated as the section rubs on the knife facet
- Eliminate electrostatic charges that accumulate during the cutting process as attractive forces cause sections to fold
- Have a moderate surface tension
- Not wet the section
- Not damage any materials present in the trough.

At room temperature the most common trough fluid is distilled water as it fulfills all of the requirements satisfactorily. The high surface tension of water prevents wetting of the block face and allows sections to float on the surface. Also the

surface tension is high enough to stretch the sections and preserves the shape. The low viscosity of water allows sections to slide along the knife facet and on the water surface and prevents section compression. Water does not wet the most commonly used epoxy resins and is not a strong solvent that would dissolve most samples [7, 38]. Other trough fluids are mainly used for the sectioning below the freezing point of water, also referred to as cryo-ultramicrotomy. Cryo-ultramicrotomy can be done like conventional ultramicrotomy with a trough fluid that freezes below the used temperature during sectioning [39]. The most common trough fluids for cryo wet sectioning are a Dimethyl sulfoxide (DMSO) solution and ethylene glycol [7].

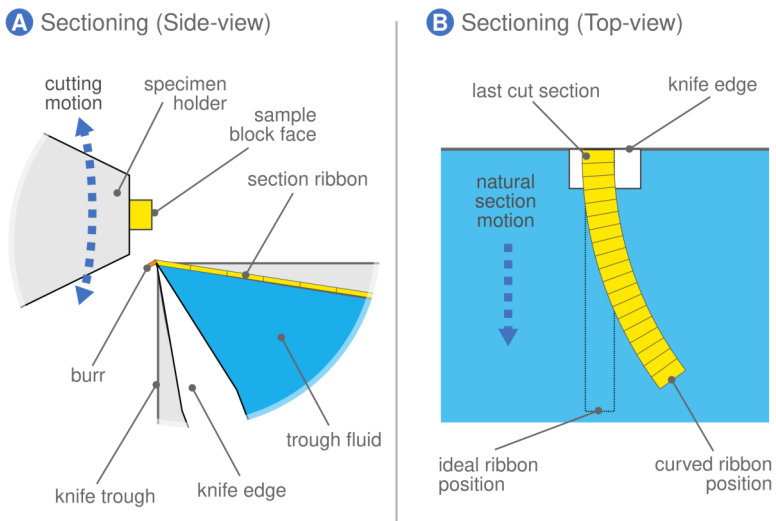


Figure 2.3: A) Formation of section ribbon by successive attachment of new to previous sections. B) Section ribbon curvature caused by imperfect trimming or compression.

To facilitate section collection in Array Tomography, sections are cut in a way that allows the formation of section ribbons as shown in Figure 2.3A. Section ribbons contain multiple sections in defined order which can be manipulated as a unit.

Stable ribbons are obtained by the application of adhesive or contact cement on the side faces of the sample block [5, 12, 40]. The attachment of new sections to the ribbon causes a natural motion of previous sections away from the knife edge as depicted in Figure 2.3B. Due to compression or imperfect trimming, unequal sides of the sections can cause a curvature of the ribbon, which can be more or less dominant. A calculation of the ribbon curvature is provided in Appendix A.2.

After the ribbon is sectioned, it is floating on the water surface and needs to be collected as described in the following Section 2.1.5.

2.1.5 Manual Serial Section Collection

In Array Tomography large numbers of serial sections are collected on solid carrier substrates. This requires that the floating section ribbons are transferred from the water surface onto the carrier substrates. The carrier substrate is placed inside the knife trough and partly immersed in the water as illustrated in Figure 2.4A. Array Tomography is a versatile method which allows the selection of carrier substrates depending on the chosen image modalities. The most common substrate types are silicon wafer, glass cover slips and indium tin oxide (ITO) coated cover slips.

The last cut section attaches to the knife edge. The attachment force comes from a burr of material that wraps around the knife edge as depicted in Figure 2.3A. This force can be higher than the binding force between sections and makes it difficult to remove a ribbon of sections from the knife edge [41]. If the adhesion to the knife is low enough, sections can be pulled away from the knife with help of the eyelash tool. To lower the adhesion the eyelash tool can be used to gently stroke along the back of the knife edge as illustrated in Figure 2.4B. The sweeping removes the burr and can lower the adhesion sufficiently, so that it detaches from the knife [7, 40]. A wrong use can damage the knife edge if too much shearing stress is transferred to the edge. Also the sections are easily damaged or stick to the eyelash which causes an irreversible section loss. It is also reported that the release of the ribbon from the knife edge can be accomplished by raising the water meniscus on the knife edge [40].

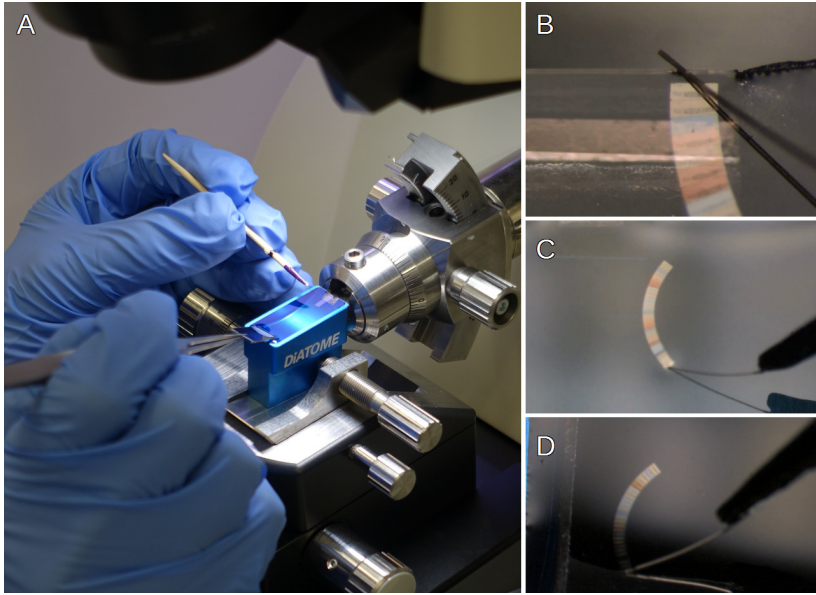


Figure 2.4: Operator performing the tasks to collect serial sections on a piece of silicon wafer from Spomer [41]. A) Knife with immersed substrate and handheld manipulation tool to collect a section ribbon. B) A ribbon is separated from the knife edge by a stroking motion. C) Dragging of a section ribbon. D) Pinning of the end of a section ribbon to immobilize it during the deposition.

The typical position manipulator for section ribbons in Array Tomography is the eyelash tool. Through physical contact of the eyelash onto the sections, as shown in Figure 2.4C, the position of the ribbon can be changed by pushing and pulling [7]. The handling of the eyelash is a delicate operation as the sections are easily damaged by contact. Another method to change the ribbon position is by striking through the water in proximity to the ribbon. This causes small water currents that change the ribbon position. The method is less precise and requires more time but safer as physical contact to the section is avoided.

The sections are deposited on the carrier substrate by retraction of the water between section and substrate. The sections should settle on the substrate without wrinkles to obtain well defined sections for reconstruction. The problem of

section wrinkles is associated to the receding contact angle of the water meniscus on the substrate [11, 27]. For a deposition without wrinkles the receding contact angle should be small and thus the surface of the carrier substrate hydrophilic. Hydrophilic carrier substrates are typically created by a glow discharge [7]. The plasma treatment creates polar OH-groups on the substrate surface that increase the surface free energy and thus wettability. The plasma treatment is performed shortly before the substrate is immersed in the knife trough as the effect decreases over time.

For the deposition on the carrier substrate the ribbon is pushed towards the interface of the substrate and the water as shown in Figure 2.4D. On contact of the beginning of the ribbon with the carrier substrate, the ribbon adheres to the surface and is partly immobilized. Ribbons can be affixed on adjacent locations to collect multiple ribbons on the same substrate [5]. When enough ribbons are collected the substrate is gently pulled out of the knife trough. The receding water meniscus settles the section ribbon on the carrier substrate. Small ribbons of serial sections are mounted on TEM grids, by similar techniques [42].

It is easy to loose ribbons during the deposition if the adhesion to the substrate is not strong enough, respectively the substrate is pulled out too fast. Also both hands are occupied by the handheld substrate and the eyelash tool, which increases the complexity of the manipulation task. Methods that assist the operator in the deposition of the ribbons have been proposed in literature and have also found their way into commercially available products. In principle, they allow a more controlled retraction of the water by either a slow lifting or by a slow draining of the trough fluid. Common to these approaches is that the second hand is not occupied with a manipulation task which reduces the complexity of the section collection.

Spomer et al. demonstrate the deposition of sections for Array Tomography with a third hand system [43]. The third hand with seven degrees of freedom is mounted on the instrument table, as displayed in Figure 2.5A. The third hand manipulates the substrate position and allows a controlled lifting of the substrate. A similar device, displayed in Figure 2.5B, with basic control of the substrate

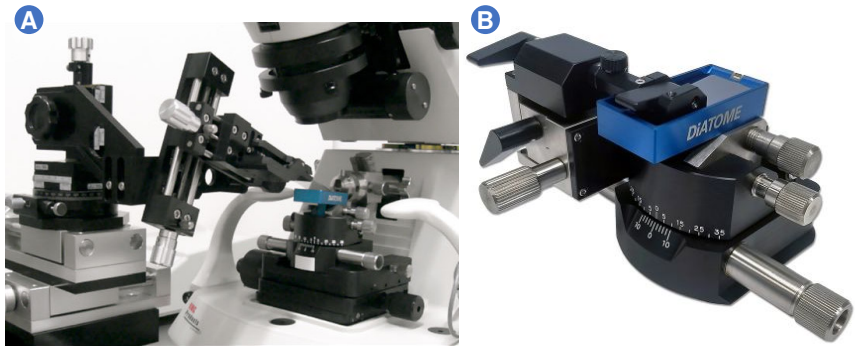


Figure 2.5: A) Picture of third hand proposed by Spomer with seven degrees of freedom to control the substrate position [12, 43]. Sections are deposited on the substrate by a manually controlled lifting motion. B) Picture of the Advanced Substrate Holder (ASH) II sold by RMC Boeckeler Instruments [44]. The ASH II has only three degrees of freedom to position the substrate but is directly mounted on the knife stage.

position but a direct mounting on the knife stage is commercially available [44]. The direct mounting provides a better decoupling from environmental vibrations compared to the mounting on the instrument table and is favourable with respect to space requirements. A simple substrate handling approach is proposed by Koike and Yamada that uses a crane-like device to slowly lift the substrate out of the trough [18].

An inverse approach to the section deposition by a controlled retraction of the water is presented by Burel et al. [45]. Instead of slowly lifting the substrate to allow a settling of the sections on the carrier substrate, the trough fluid is drained to lower the fluid level. The substrate is held in pockets manufactured into the knife and the trough is wider to provide space for bigger carrier substrates. The fluid is drained through a valve or with help of a syringe. Care has to be taken that the sections do not change position during the draining of the water. Array Tomography knives that follow this principle are commercially available from knife manufacturers.¹

¹ Diatome (Ultra ATS) and Syntek (JumboWT).



Figure 2.6: Diatome ATS knife presented by Burel et al. [45, 46]. The carrier substrate is placed in the bottom of the knife boat. After the section ribbons are positioned above the substrate, the water is drained from the boat using a syringe or valve.

Despite the aid of third hand manipulators and Array Tomography knives, manual manipulation is still required to remove the section ribbon from the knife edge and to place the ribbons above the carrier substrate. Still, compared to available completely automated solutions as described in Section 2.2, the manual section acquisition offers the most extensive image modalities, because of the available carrier substrates and sectionable volume.

2.1.6 Manual Section Monitoring

During sectioning, thickness variations can occur, as described in Section 2.1.4. These variations can be within a single section, so called chatter and/or between subsequent sections. The operator must identify variations early in order to react

by adjusting the cutting parameters to reduce these variations. Ideally, this tuning should occur inline.



Figure 2.7: A) Panel of nine exemplary views through the stereo microscope of the ultramicrotome. Floating sections with varying thickness from 50 nm to 200 nm can be observed. The ultramicrotome knife used in the image is of an old type which produces a curved water surface, thereby making it specially difficult to observe the section in the reflection. Also ambient light scattered on the bottom surface of the boat superimposes with the reflected light on the water surface and makes it difficult to see the sections. The first two images of the panel show the irregular illumination of the light source used (chess board like structure). B) Typical interference color reference chart for ultramicrotome sections.

A simple method that has been in use since the 1950s to monitor section thickness is the observation of interference colors of sections floating on the water surface directly after they have been cut, as shown in Figure 2.7A. These interference colors show a distinct sequence as the color transitions from gray (<60 nm), silver (60 nm to 90 nm), gold (90 nm to 150 nm), purple (150 nm to 190 nm) and blue (190 nm to 240 nm) [47, 48]. Ultramicrotome manufacturers supply section color reference charts as seen in Figure 2.7B, that can be used as a rough reference for visual thickness estimation. Although this method is quite effective, it bears some disadvantages. The interference colors depend on the illumination and the refractive index of the section material [49]. Further the thickness estimation is qualitative and subject to human interpretation. It is as such depending on the operator and does not provide precise absolute values. Relative thickness

variations can be seen easily as the human eye is sensitive in detecting color variations, but this perceived color difference is not uniform over the complete range of interference colors as a gradient of the section thickness. The limitation of perceived color difference and section thickness difference is demonstrated using a color perception model in Section 3.3. For example the transition from gray to silver is more subtle than the transition from purple to blue although the relative thickness change is greater in the first example. This makes it difficult to identify and quantify variations early in the cutting process. Also for the later analysis of the sections, it is in some cases of importance to know the exact section thickness. Thereby often the nominal set thickness on the instrument is trusted [50, 51]. The true section thickness may differ from the nominal thickness due to factors such as thermal influences, as described in Section 2.1.4.

2.2 Automated Solutions for Serial Section Acquisition

2.2.1 Automated Collection on Tape – ATUMTome

The Automatic Tape-collecting Ultramicrotome (ATUM) for fully automated serial section collection was patented 2014 by Hayworth et al. and is commercially available as a retrofit extension to existing ultramicrotomes [52]. The system is tailored to collect very large numbers (20,000 or greater) of large area (3 mm × 2 mm) ultra-thin sections on flexible carrier substrates [53].



Figure 2.8: ATUMtome system to collect serial sections on a flexible tape [29]. The tape collection system is mounted on the front side of the antivibration table and reaches into the knife trough on the ultramicrotome (PT-XL).

The carrier substrate is made of a flexible tape that travels through a reel-to-reel collection device. Comparable to a conveyor belt, the collection device guides the tape through the knife trough and picks up sections from below the water surface. Through the adhesion of sections to the moving tape, the sections are separated

from the knife edge and deposited on the tape. By the direct collection following sectioning, the position of the sections relative to the tape is fully defined and the sectioning can be performed in a continuous cycle without interruption [54]. While one reel dispenses empty tape, the second reel takes up the collected sections for the subsequent imaging. The reel of collected sections can as such not be imaged in conventional microscopes and requires either a manual cutting and grounding of the tape on a solid and planar substrate, such as a silicon wafer, or special reel-off devices for the microscopes [53, 55]. The density of collected sections is low, with about 200 sections per 100 mm substrate diameter [27]. The default tape material is Kapton which suffers from strong autofluorescence and thus limits the application of fluorescence microscopy for analysis [11]. The unique property of Array Tomography to offer the highest versatility of applicable image modalities is as such limited by the constraints of the tape material. The development of other tape materials is an ongoing research subject [11, 55]. The system is equipped with an automated water level control that compensates for water removed during the section collection. The ATUM system offers a highly integrated method for the high throughput section collection but the carrier substrate limits the available image modalities.

2.2.2 ARTOS 3D

The commercial ARTOS 3D (ARray TOMography Solution, Leica) as shown in Figure 2.9 can collect a medium range set of sequential sections for Array Tomography. The in 2018 introduced system sections and collects a set of section ribbons automatically on a single piece of solid carrier substrate [23].

The carrier substrate is placed in a fixed position and submerged in the knife trough similar to Array Tomography knives as described in Section 2.1.5. The novel approach of this system resides in the fact that the knife position is changed laterally after a section ribbon is obtained. On a free position of the knife edge a new ribbon can be sectioned while the previous ribbons are still attached to the knife edge. This way multiple parallel arranged section ribbons can be obtained



Figure 2.9: A) Side view of the Leica ARTOS 3D [23]. Visible is the knife trough installed inside an acrylic environmental housing with an access to operate the draining valve for a controlled fluid outflow. The three pictures on the right side are extracted from a Leica video, showing the steps of collecting 150 serial sections contained in three ribbons observed through the stereo microscope [56]. B.) Three ribbons (gray : 60 nm) for later analysis sectioned from the right to the left are attached to the extra wide diamond knife. C.) Sacrificial sections (gold : 100 nm) push the sections for analysis (gray) above the carrier substrate. D.) The trough water is drained to settle the sections on the carrier substrate.

simultaneously in the trough (see Figure 2.9B). The section ribbons positions are partly immobilized as the top of the ribbon is still attached to the knife edge. The knife trough is housed in an environmental chamber to shield external air streams that can bend the sections ribbons. The re-positioning of the knife to obtain a new ribbon on a free position of the knife edge requires a reoccurring approach of the knife towards the sample. The system does not directly measure the distance of the knife edge to the block face (compare to Section 3.1), but relies on an open loop position control that requires a set-up with a highly precise movement control. To avoid changes in the section thickness the positional accuracy must be a fraction of the claimed section thickness of 20 nm to 200 nm [23]. This implies

also the use of knives that do not vary in straightness by more than a fraction of the section thickness over the length of the knife edge. Every deviation of the targeted position causes a thickness variation at the transition to the next section ribbon. Deviations that are higher than the maximum section thickness of 200 nm can cause damage to the knife edge.

Once all ribbons for the later analysis have been obtained, the knife position is changed back to the initial position of the first ribbon. Thick (100 nm) sacrificial sections are then cut to push the section ribbon above the submerged carrier substrate. Those sections are only used to position the section ribbon above the carrier substrate and are lost for the analysis (see Figure 2.9C). This process is repeated until all sections selected for analysis are positioned above the substrate. The number of obtainable section ribbons on the area of the carrier substrate is constrained by the straightness of the ribbons and the length of the diamond knife. The straightness of the section ribbon can change during sectioning due to areas of inhomogeneous compressibility within the sample. Longer diamond knives are considerably more difficult to manufacture and the cost driving component of ultramicrotome knives.

A drain valve inside the trough allows the controlled draining of the trough fluid to settle the section ribbons on the carrier substrate (see Figure 2.9D). This is the same approach like it is used in Array Tomography knives as described in Section 2.1.5. The sacrificial sections remain in the trough during draining, are not collected on the substrate and thus lost volume for the analysis. This section loss must be considered in the planning of the analysis and may be an exclusion criterion for samples that are difficult to obtain or do not tolerate a loss of analytical volume. The beginning of the sectioned volume must be planned carefully in order to avoid loss of for the analysis interesting material in the sacrificial sections. Sacrificial sections that remain on the knife edge need to be removed manually as a drying of sections on the knife edge renders the knife edge inoperable (see Section 2.1.4). The knife trough needs careful cleaning to remove remaining sections that can contaminate subsequent collection processes.

2.3 Solution Space for Machine-based Section Acquisition

In literature different systems have been proposed and prototypes implemented for the machine-based section acquisition in Array Tomography. This section divides the proposed systems into elementary tasks that are necessary for acquiring serial sections:

- **Sample Advance and Alignment**
- **Section Collection**
- **Section Monitoring**

For each of the tasks an overview of the in literature proposed solutions is provided. The solutions are differentiated into common approaches to extract the essential ideas how section acquisition can be performed.

The conceptual separation is also the basis for the novel methods for a machine-based sample advance presented in Section 3.1, section collection in Section 3.2 and section monitoring in Section 3.3.

2.3.1 Sample Advance and Alignment

Available ultramicrotomes produce sections in well defined thickness if they run in a continuous sectioning cycle. The sample advance, the cutting motion and speed transitions are completely handled by available ultramicrotomes. With the currently available systems two problems are still unresolved or require a well trained operator:

1. The initial **alignment and advance** of the sample towards the cutting plane.
2. A completely **closed loop sample** advance between block face and cutting plane.

The initial **alignment and advance** of the sample is in conventional ultramicrotomes performed by the visual interpretation of a reflection on the block face as described in Section 2.1.3. An experienced operator achieves a final distance of less than 1 μm between the sectioning plane and the sample block face. For conventional microtomes, systems have been proposed that automate the initial alignment and advance, but these systems do not offer the precision required in ultramicrotomy [57, 58]. The challenge in implementing such a system, besides the required precision, is that a determination between two planes takes place, that both cannot integrate a measurement device. The measurement does not only include the distance but also the correct orientation of three rotational axes. To date a complete alignment and advance can only be achieved by the human-based interpretation of the reflection of the knife edge.

A **closed loop sample advance** imposes even stronger requirements on the accuracy of the measurement device. To date the sample advance is measured offset from sample block face and cutting plane and thus exposed to a permanent drift caused by thermal expansion of the system and relaxation in the sample block. To keep the influences of the advance drift small, it is desirable to have a time consistent and fast sectioning cycle. When the sectioning is interrupted the section thickness can substantially differ from the desired section thickness, as the actual sample advance is not directly measured. According to Templier this "half a century old restart issue remains unaddressed in the literature" [27]. Systems have been proposed that measure the distance offset but closer to the block face and the cutting plane with nanometer resolution using capacitive measurement principles [59] or by multi-phase interferometry [25]. This might lower the influence of a thermal drift on the sample advance, but relaxation in the block is not measured. It has been described that also the operator has a direct thermal influence on the temperature measured on the sample block [41]. A remote operation of the instrument is thus desirable to reduce thermal influences.

2.3.2 Section Collection

Section collection can be subdivided into three elementary tasks that are a requirement for the collection of sections in Array Tomography:

- **Section Separation**
- **Section Localization**
- **Section Deposition**

Section Separation

Sections remain attached to the knife edge in the ultramicrotome sectioning process. Overhanging polymer fibres on the knife edge create a form fit that is responsible for the adhesion to the knife edge [41]. For section collection the sections need to be separated from the knife edge. Separation requires that the sections are first detached and then cleared from the knife edge. The section separation from the knife can be accomplished by various techniques with an overview provided in the following paragraphs. Three main principles have been described in literature, the separation by:

1. **force**
2. **adhesion reduction**
3. **successive section pushing**

For section separating by **force**, a force needs to be applied that is bigger than the adhesion force between section and knife edge. A manual technique in conventional Array Tomography applies this force with an eyelash that drags the sections away from the knife edge as described in Section 2.1.5. Potentially damage and section loss can occur through the physical contact of the eyelash. The Allen institute proposes an ArrayBot which automates the conventional manual technique by computer-controlled motion axes [4]. Lee et al. apply an air blast which transfers a separating force without physical contact to remove sections from the knife edge [26]. The ATUMtome detaches and drags sections from

the knife edge like a conveyor belt, by the physical contact of the tape collection system to the bottom of the sections [22].

For section separation by **adhesion reduction**, the section adhesion is lowered to facilitate a separation from the knife edge. A manual technique detaches sections from the knife edge by a gentle stroke with an eyelash along the back of the knife edge to remove the overhanging polymer fibers [40]. Lee et al. use a robotic linear stage equipped with an eyelash end-effector to automate this stroking motion and apply an air stream induced circular motion of the water surface that moves the section away from the knife edge [28]. Spomer proposes the use of a cutting motion without sample feed (zero-feed) to remove overhanging polymer fibers, but observes that this technique does not reliably detach sections as the adhesion force is not always sufficiently lowered [41]. Templier places an ionizer tip close to the diamond knife which creates a soft ionized air current that randomly detaches sections from each other every few sections without physical contact [27]. The benefit of this detachment method is that it is non interrupting and thus not impairing the sectioning process as described in Section 2.3.1. Adversely the separation is not well controllable as it can not be guaranteed that a section is detached from the knife edge as a chance remains that the section is not separated by the ionizer. Spomer proposes that a coating of the sample block sides with a release agent can be used to prevent the formation of ribbons by removing the cohesion of the section ribbon [41].

For section separation by **successive section pushing**, the natural motion of a section ribbon away from the knife edge, as described in Section 2.1.4, is used. The resulting pushing of previous sections can be considered the natural motion of the sections away from the knife edge during the sectioning process. The Artos 3D (Leica) uses thick sacrificial sections to detach and separate the sections reserved for analysis from the knife edge as described in Section 2.2.2. The sacrificial sections remain attached to the sections reserved for analysis and are lost sample volume during the final collection step. Hess proposes the iTome which also uses sacrificial sections but avoids the loss of analytical volume by cutting sacrificial sections from a second block in order to preserve the original block volume for analysis [25, 60]. Spomer proposes a system that also uses the natural motion of

the section ribbon to position a section ribbon. The loss of sections is avoided by separating the section ribbon above the carrier substrate with a dispensed micro drop. The pushing sections are then the beginning of a new ribbon which can also be collected [41]. A second method he proposes performs a partial cut, followed by a reversal of the cutting motion during which the capillary force of the retracting water meniscus separates the section from the block [41].

Section Localization

Sections need to be localized after they are sectioned from the sample block, as it is a requirement for the deposition as well as subsequent imaging steps in Array Tomography. The here used localization term refers to the placement of a section, which consists of three properties:

1. **Position**
2. **Orientation**
3. **Sequence**

For each deposited section the information of position, orientation and sequence must be known to allow a reconstruction. For the reconstruction it is actually the depth at which a section was obtained that is required, but the depth can be derived from section sequence, provided that the section thickness is known (see Section 2.3.3). Free floating sections in the knife trough can change the placement on the two dimensional water surface. The section collection method must therefore either constrain, track or a posteriori determine the section placement.

The uncertainty in the placement of freely floating sections can be avoided by a direct collection subsequent to the sectioning. The cutting process initially defines the placement of all sections and the adhesion to the knife prevents a section movement. This constraint is used in the ATUM system to localize single sections and to collect them on a flexible tape directly after the sectioning as described in Section 2.2.1. A ribbon of sections is a structure that contains sequential sections in defined sequence and orientation and is used in manual and automated section

collection. The ARTOS 3D system localizes the sections in ribbons that adhere to the knife edge, while the accuracy of the section localization is limited by the curvature of the section ribbon as described in Section 2.2.2. Cheng and Liu place two baffles on the left and right side of the diamond knife to guide single sections away from the knife edge into a collection position and apply a neural network based section detection to synchronize the lifting motion of a rotating carrier substrate [61]. Campbell proposes the localization of section ribbons inside a fluidic channel enclosed by a long stainless steel tubing [62]. Spomer demonstrates an automated method by forming the bottom of the fluidic channel from the carrier substrate, which is also used for the collection [41]. The physical contact to a fluid enclosure can cause sections to get stuck and requires straight ribbons. Lee et al. define the position of sections without physical contact by a trapping technique that utilizes curvature-induced capillary-based forces and hydrodynamic Stokes-drag based forces to trap free-floating sections [28]. Templier presents a system that uses superparamagnetic nanoparticles in the embedding material to attract sections to a permanent magnet and remote magnetic actuation without physical contact allows the agglomeration of floating sections in the center of an silicon wafer [27]. Other methods actively change the position of the sections. Lee et al. use an automated loop, known from the manual collection of sections on TEM grids, to transfer single sections from a trapping point onto a piece of silicon wafer [28]. A position manipulation requires a means to identify the desirable position change (see Section 2.3.3).

To unambiguously define the section **orientation**, a rotationally asymmetric section shape can be used to provide a distinct marking [7]. Markers in the sample block can be present to allow a retrieval of the section sequence and/or orientation of individual sections after the collection. Templier applies an increasing ratio of detectable superparamagnetic nanoparticles to retrieve the section **sequence** and orientation from freely floating sections [27].

Section Deposition

In principle two different techniques for section deposition exist in Array Tomography. The substrate is either **lifted** or the fluid level **lowered** to retract the water in between section and carrier substrate.

The original technique for Array Tomography, described by Micheva and Smith, belongs to the first category, as the sections are deposited by a slow manual **lifting** of the substrate as described in Section 2.1.5. The manual third hand proposed by Spomer et al. allows for a more controlled lifting motion and a precise alignment of the substrate [43]. In the ATUM system the substrate is lifted because the tape rises above the water surface [22]. The ASUM system uses a tilted wafer which rises above the water surface due to a rotation [61].

A **lowering** of the fluid level by a draining outlet in the knife trough is demonstrated by Burel et. al [45]. A similar draining is used by the ARTOS system described in Section 2.2.2. Spomer drains the fluid through a tubing connected to the fluid reservoir [41]. Templier heats the carrier substrate to 40 °C to speed up the evaporation of the trough fluid which lowers the fluid level [27].

2.3.3 Section Monitoring

Section monitoring is required during the acquisition of serial sections for Array Tomography and in principle covers three tasks to determine:

1. Section position
2. Section shape
3. Section thickness

During the section acquisition process, it is necessary to determine the position of the sections in order to move them onto the carrier substrate. Determining the shape of the sections is necessary to identify potential issues such as partial cuts or delamination, which may indicate problems in the sectioning process.

The determination of the section thickness is required for proper tuning of the cutting parameters during sectioning and for accurate scaling during reconstruction. Thereby often the nominal set thickness on the instrument is trusted [50, 51]. For the determinations of shape and position it is sufficient to detect the sections material on the water surface. Due to the ultra-thin thickness of ultramicrotome sections, they are nearly completely transparent, making it difficult to detect them without special techniques.

For human-based section monitoring the observation of interference colors is an established technique as described in Section 2.1.6. The interference colors are observed in the reflection of a top light on the water surface of the knife trough. The thin film interference colors cover all three described determination tasks as they do not only make the transparent section visible but also relate to the section thickness. An estimation of section thickness by the observed interference color is a long known method to monitor the sectioning process but subject to human interpretation [48, 63].

Efforts have been taken to allow a machine-based online section monitoring. Spomer presents a machine-based thickness estimation based on the interference colors of already deposited sections on carrier substrates [41]. The sections are monitored by a camera and compared to a color model of pre-calculated interference colors. The estimation determines position, shape and thickness but requires external calibration and is thus not well suited for an inline monitoring of the sectioning process [41]. Cheng and Liu present a machine-based monitoring of floating sections by a machine learning-based object detection [61]. The object detection determines the position and orientation, but does not provide shape and thickness information.

Alternative methods exist that provide a quantitative thickness measurement but are not suitable for inline monitoring as they require deposited sections and are performed on external instruments. These methods are used to verify the nominal set thickness of the instrument for analysis and reconstruction. Direct measurement methods can be performed using Atomic Force Microscopy (AFM) or by the

destructive Orthogonal Re-Embedding (ORE) method [48, 64]. Moreover methods exist that model physical properties of the sections to determine the thickness. Methods that model the optical properties are for example ellipsometry, interferometry and reflectometry [47, 65, 66]. Other methods apply image statistics to model the scattering of the electron beam in the section material [67, 68]. Another method determines the average section thickness by the total reduction of a sample block after a series of sections is obtained [64].

It is also possible to measure known reference structures inside subsequent sections and conclude the true section thickness from this information. These reference structures must be present in the sample itself or can be added to the embedding material. Muscular fibres for example show a periodic structure and are successfully used as a standard measure as well as polystyrene latex spheres mixed in the embedding material [35, 69]. Especially for biological samples the staining and embedding procedures introduce a shrinkage compared to the *in vivo* sample which might require reference structures for a correct interpretation of the reconstruction [7].

3 Methodology

The following sections describe new machine-based methods and modifications to the ultramicrotome to automate the serial section acquisition for Array Tomography.

The first Section 3.1 describes a novel and first of its kind system for a machine-based sample advance prior to the sectioning process. The second Section 3.2 describes the machine-based section collection process. The process utilizes the properties of microfluidic channels to localize ribbons of sections on the carrier substrate. In these channels substrate and sections move in unison, which allows the separation of sections from the knife and a repositioning of sections with help of an automated substrate handling unit. The last Section 3.3 describes a machine-based section monitoring that is the first solution for an inline and quantitative measurement of section thickness variations.

3.1 Machine-based Sample Advance

The sample block face needs to be aligned and then advanced to the cutting plane before the sectioning process can start. In conventional ultramicrotomes, this is a manual step performed by the operator. During the alignment of the sample block face to the cutting plane, three rotational degrees of freedom need to be adjusted. With the trimming procedure described in Appendix A.1, the correct orientation of two rotational axes is enforced – the rotation of the sample block along the arm axis and the rotation of the sample block along the axis of the knife edge. The remaining axis that needs angular adjustment is the rotation of the knife edge around the vertical axis due to mounting tolerances after switching from the trimming knife to the sectioning knife. When the sample block face is correctly aligned to the cutting plane, the final advance of the sample towards the knife edge can be performed. The presented machine-based sample advance provides a numeric measurement of the angular misalignment that the operator uses to adjust the rotation of the knife stage. The final advance of the sample towards the knife edge is performed fully automated and then the sectioning process started.

The challenge in implementing the automated sample advance system is, among others, that a measurement between two planes takes place – on the one hand the virtual cutting plane of the diamond knife and on the other hand the sample block face. This complicates the installation of a direct measurement system [25]. The presented machine-based sample advance utilizes the reflection of the back light on the sample block face. The optical setup is illustrated in Figure 3.1A and similar to the conventional setup used during the visual sample advance performed by the operator. A camera mounted on the ultramicrotome’s stereo microscope is used for a machine-based observation of the back light reflection.

In the conventional sample advance the operator estimates the distance of the sample to the knife edge by the band of light that the reflection of the back light causes on the block face as described in Section 2.1.4. In Figure 3.1 the two light paths that define the width of the band of light are illustrated. One light path is the last possible ray that gets directly reflected at the knife edge. The other light

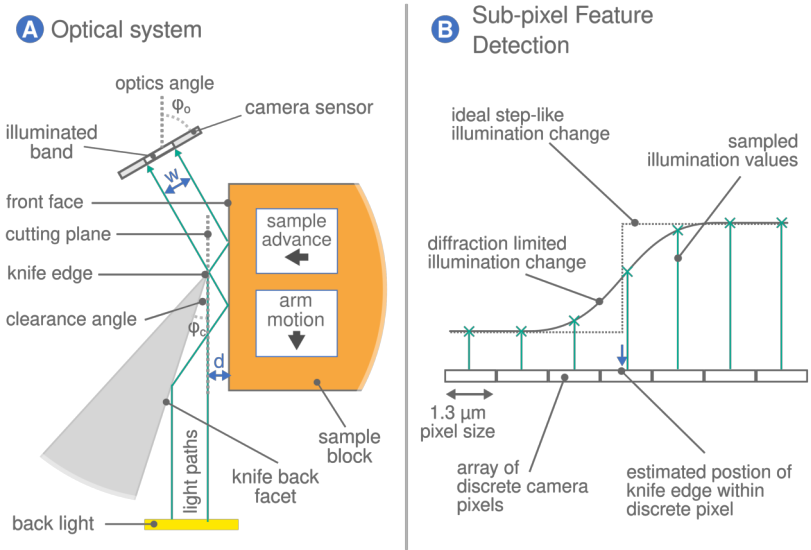


Figure 3.1: A) Back-light reflection light path. The gap between knife edge and block face allows only a portion of the light to reach the camera sensor. This is visible as a band of light that diminishes with decreasing distance between block and knife edge. B.) Diffraction limited illumination change. An interpolation based on the measurements of multiple pixels is used to estimate the position of the knife edge with sub-pixel accuracy.

path is the corner case where the ray gets reflected on the back facet of the knife and is just able to pass in front of the knife edge. These two paths define the width of the observable band of light illuminated by the back light. As the sample is advanced towards the knife edge, the width of the illuminated band gets smaller until it completely vanishes when the sample is in proximity of the knife edge. The operator exploits the light diffraction during the manual advance of the sample block by observing diffraction colors to achieve sub-micrometer precision. The observation of these diffraction colors requires a fine tuning of the optics angle to allow light to pass through the narrow gap. A machine-based identification of the diffraction colors in the light gap is thus difficult. The algorithm does therefore not rely on diffraction colors like the conventional manual sample advance but

uses an estimation algorithm to predict the exact point at which the sample gets into contact with the knife edge.

The angle of the optical lens system is important because it must allow light coming from the back light to pass through the narrow gap between block face and knife. Figure 3.1A shows the vertical light paths that originate from the back light. Knives can have an inbuilt clearance angle and are installed with an additional clearance angle set on the knife stage. For the light to pass from the back light through the narrow gap between knife and sample block face, the optics angle φ_o should be the twice the total clearance angle φ_c as defined by

$$\varphi_o = 2\varphi_c. \quad (3.1)$$

Diffraction imposes a principle limit on the resolution of any optical system [70]. To achieve the required sub-micrometer precision, an optical measurement must account for light diffraction. At the knife edge, diffraction causes continuous illumination changes in the margins of the illuminated band at scales beyond the Abbe resolution limit. Figure 3.1B illustrates an exemplary illumination change. The shape of the illumination change is defined by the Point Spread Function (PSF) of the optical system, which is sampled at discrete points by the camera's sensor pixels. By using previous knowledge of the PSF and knowing that the knife edge is a nearly ideal step-like image feature, the exact position of the edge can be reconstructed through interpolation of the discrete sample values of the camera pixels [71, 72].

The sample block is usually an inhomogeneous composition of different materials that can affect the brightness of the illumination. To remove features from the image that can potentially affect the measurement of the width of the illuminated band, several images are taken as the sample block passes the knife edge. The reflection is fixed in its position, while features on the block face move. By stacking these images, the inhomogeneities of the sample block are effectively averaged out, eliminating potential disturbances to the image feature detection. This allows for more accurate measurements of the width of the illuminated band.

The so obtained image of the back light reflection on the sample block face contains multiple features that represent physical system properties and is depicted in Figure 3.2A. When the knife edge is parallel to the sample block face, the edges of the illuminated band are parallel. The width of the illuminated band w is then proportional to the distance between knife edge and sample block face. A misalignment of the knife edge to the sample block face causes an angle ϵ_k between the edges of the illuminated band. While a rotation of the camera causes the edges of the reflection to be equally sloped. The camera rotation ϵ_c does not need to be corrected, but it is necessary to know for the calculation of the knife angle ϵ_k .

The width of the illuminated band w (Figure 3.1) is directly proportional to the distance d of the sample. The system measures the width of the band, advances the sample and performs the next measurement. A polynomial fit is performed for the nominal set advance and the measured width of the band of light. The fit model is capable to determine the advance at which the light vanishes because the sample is in proximity of the knife edge. Every obtained sample point improves the certainty of the estimate. When the model uncertainty (std. deviation) is lower than 250 nm, the software advances to the estimated contact point with a safety margin based on the standard deviation.

The feature extraction process, shown in Figure 3.2B, determines the positions and angles of the knife edge and its reflection on the block face with sub-pixel precision. It utilizes the knowledge that the knife edge and its reflection on the block face are almost perfectly straight image features. The process begins by capturing a grayscale raw image in which the pixel value corresponds to the illumination captured by the sensor. The image is then sliced horizontally into N slices, which are successively shifted by an increasing number of pixels in positive and negative direction (see Figure 3.2B Step 2). The number of slices N and thus the total number of shifting operations correspond to the performed image rotation. The rotated image is then collapsed into a line profile by calculating the mean illumination in each image row. This image rotation and collapsing is pre-calculated for a range of possible rotations. In the next step, a model fitting is

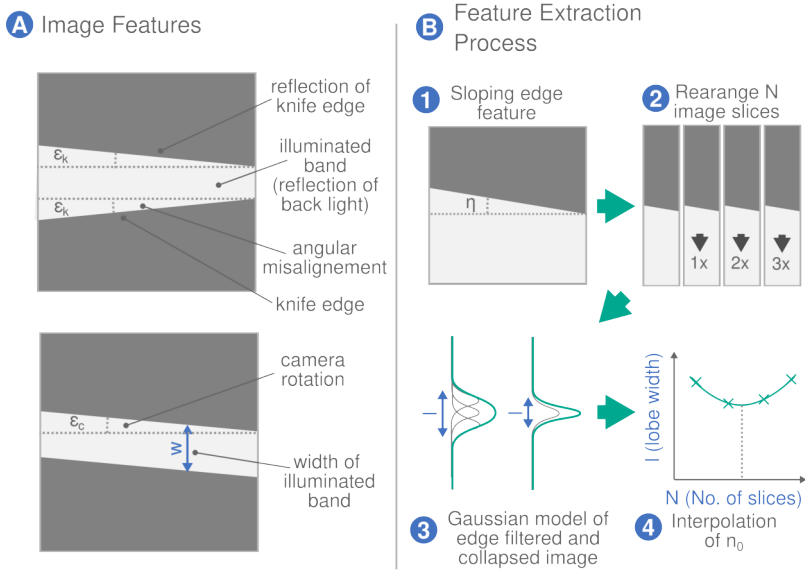


Figure 3.2: A) Depiction of an illuminated band caused by the reflection of the back light on the block face. Misalignment of the knife edge, camera rotation and block distance are detectable as features of the illuminated band. B) Feature extraction process which detects the position and angle of the edge features with sub-pixel precision (1). The image is sliced and rearranged to compensate for a slope of the edges (2). A collapsed line profile is then edge filtered. The lobe width is determined by fitting an Gaussian model (3). The Gaussian model with the smallest lobe corresponds to the angle of the feature in the image. Through interpolation of the model parameters, the position and angle of the edges can be measured with an accuracy smaller than the pixel size (4).

performed on these line profiles to determine position and rotation of the edges with sub pixel precision.

The sharp knife edge appears as a convolution of the step-like intensity change of the nearly perfect knife edge with the Point Spread Function (PSF) of the optical system due to light diffraction. A common model for the PSF of an optical system

is the Gaussian function [73]. For each of the pre-calculated intensity profiles, the Gaussian function

$$f(x) = a \cdot \exp\left(-\frac{(x - x_0)^2}{2l^2}\right) \quad (3.2)$$

is fit to the sampled values. In this model, the parameter x_0 corresponds to the position of the edge and the parameter l expresses the "sharpness" of the edge by the lobe width (see Figure 3.2B Step 3). The line profile with the smallest lobe width l corresponds to the rotation that best matches the angle of the feature, but the obtained rotation values are still limited by the discretisation of the image pixels. Therefore the lobe widths l are assigned to the corresponding number of discrete shifts N and fitted to a quadratic polynomial (see Figure 3.2B Step 4). The minimum n_0 of this quadratic fit corresponds, for a given image width b , to the feature rotation by

$$\eta_0 = \arctan\left(\frac{n_0}{b}\right). \quad (3.3)$$

The derived values for x_0 and η_0 measure the position and the rotation of the edge features with the required sub-micrometer precision. To fit the polynomial and Gaussian functions, the implementation uses the curve fitting functions from numpy and scipy libraries [74, 75]. The camera used (IMX252, Lt345RC, Lumen-era) has a pixel size of 3.45 μm which is in combination with the ultramicrotome's stereo microscope at maximal magnification able to resolve a sufficient number of sample points of the PSF.

The results of the machine-based sample advance are presented in Section 4.1.1, including for example the observation and also compensation of thermal drift affecting the sample advance.

3.2 Machine-based Serial Section Collection

As outlined in Section 2.3.2, so far ribbons are only deposited on unstructured substrates or on substrates with mechanically enclosed channels. These channels allow the manipulation of individual ribbons which are otherwise coupled together by surface tension forces [41, 62]. In the presented methodology chemically tailored solid/fluid/solid interface driven organization is utilized to acquire ultramicrotome sections in large numbers on solid substrates.

Forming channels that limit the amount of water surrounding the section and restrain possible movements, provides benefits for a machine-based section acquisition. The channel idea is developed further to allow a novel method to acquire serial sections on solid substrates which is still a challenge [4]. The key idea is the creation of microfluidic channels, in which water acts significantly more rigid due to the different scaling of inertial and viscous forces in a fluidic system. This rigidity is used to immobilize the section position relative to the carrier substrate. Through surface functionalization a contrast of wettability is created. Microfluidic channels form on the carrier substrate in areas that show a high wettability by the trough fluid. These channels integrate a deposition pattern for the ultramicrotome sections directly on the substrate.

By a site selective modification of the substrate's surface free energy, the fluid is contained in channels without a mechanical enclosure. Compared to a mechanical enclosure, the channels created by wettability contrast bring several benefits:

- A mechanical enclosure requires straight ribbons and wide channels as the sections stick to the enclosure on contact [41].
- The deposition of sections without wrinkles requires a hydrophilic carrier substrate as described in Section 2.1.5. On a hydrophilic substrate capillary forces between substrate surface and mechanical enclosure cause leakage [41].
- The height of the channels that form on the substrate by a contrast of wettability is a fraction of the immersion depth as described in Section 3.2.1.

This enables the usage of microfluidic effects for the section immobilization as shown in Section 3.2.2.

- Surface structuring methods allow finer channels compared to mechanical enclosures. Multiple parallel narrow hydrophilic channels can localize sections in a dense packing.

The machine-based acquisition requires a modified ultramicrotome sectioning knife. The modification consists of a wider trough to allow a lateral movement of a carrier substrate. The inner width of the trough is changed from 25 mm to 53 mm to allow a lateral movement of the carrier substrates with 22 mm width inside the trough across the 3 mm wide diamond. The ultramicrotome sectioning process itself, as described in Section 2.1.4, remains unchanged. An ionizer is used to reduce electric charges on the sample block face that impair the sectioning process. For a stable sectioning process the ambient humidity is around 50 % and the ambient temperature controlled at 20 °C.

A motorized carrier substrate manipulator is used for substrate positioning. The manipulator can be considered as a further evolution of third hand systems known from manual section collection as described in Section 2.1.5. The mechanical axis configuration is taken from Schmidt [76]. The movement range covers the translation in the three spatial axes and the rotation of the substrate along the axis of the knife edge. It is mounted on the knife stage and occupies a small installation space to provide good accessibility to the instrument. A picture of the device mounted on an ultramicrotome is shown in Figure 4.2.

The process of the developed machine-based collection forms a cycle as depicted in Figure 3.3. The process uses four steps:

- A) A ribbon is sectioned and pushed into a free channel on the carrier substrate.
- B) The ribbon is cleared from the knife edge.
- C) A protrusion is used to push the section ribbon completely into the channel.
- D) The substrate is re-positioned to collect the next ribbon.

During the steps that involve positioning the carrier substrate, the sections are immobilized on the carrier substrate by the microfluidic properties of the channels. Finally, when a substrate is filled with sections, it is lifted slowly to settle the section on the carrier substrate surface by removing the water.

In the first step section ribbons are formed by successive attachment of sections to each other during cutting. Section ribbons are beneficial as they are a structure with an inherent order. The stability of the ribbons is increased by the application of adhesive on the lower block side. A straight ribbon is desirable and created when left and right sides of the sections have equal length. This can be ensured by the trimming procedure described in Appendix A.1. A newly cut section attaches to the beginning of the ribbon and pushes the previous sections away from the knife edge (see Figure 3.3A). For properly trimmed samples, this natural movement of the ribbon is orthogonal to the knife edge. The natural motion of the section ribbon is used to place the beginning of the section ribbon inside a channel. The channels have a widening opening that assists the ribbon to enter the channel. The microfluidic channel constrains the lateral movement of the ribbon and enforces its position. The last cut section of the ribbon remains attached to the knife edge. Sections that encounter the channel boundary may become stuck and cause clogging of the channel. To reduce the risk of clogging, the substrate is moved back from the knife during the retract motion of the arm and then moves forward to the original position with a superimposed vibrational motion. This effectively releases sections that stick on the channel boundary.

In order to separate the section ribbon from the knife edge two fast strokes with a cutting speed of $10 \frac{\text{mm}}{\text{s}}$ and zero advance are performed. The strokes reduce the section adhesion to the knife edge by clearing overhanging material from the knife edge. The method is known to reduce the adhesion force, but not necessarily to cause a complete separation from the knife edge [41]. By a motion of the carrier substrate backwards, the drag on the section ribbon as a consequence of the viscous force is sufficient to separate the section ribbon from the knife edge. The process step is depicted in Figure 3.3B. To compensate for a thermal drift of the instrument, it is beneficial to perform not completely zero advance but a low advance, for example 8 nm which does not cause a section to be cut.

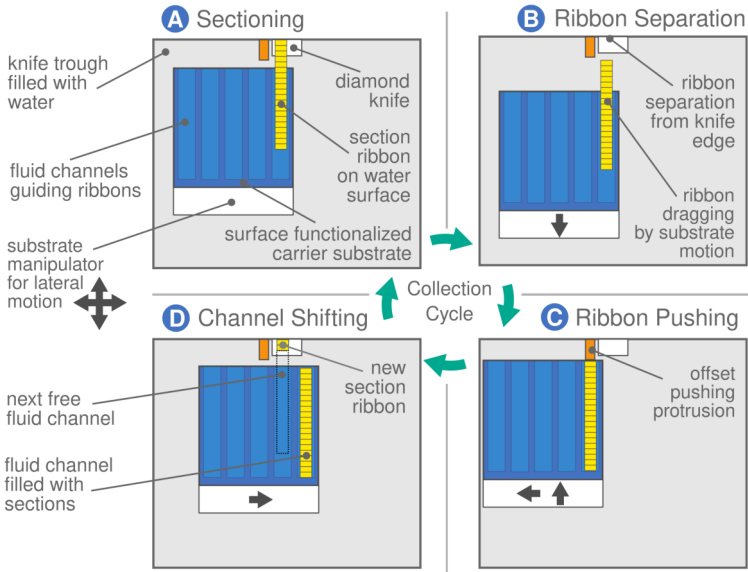


Figure 3.3: Schematic of the key steps of the machine-based section collection process as viewed from the top looking at the knife trough. Exemplary a functionalized substrate with five rectangular channels is depicted.

A thin protrusion made of Tetrafluorethylen-Hexafluorpropylen-Copolymer (FEP) foil is used to push the ribbon completely into the channels. FEP foil is known for its utilization in high-purity applications and the low surface free energy [77]. It is important that the protrusion does not cause a contamination of the trough fluid and the low surface free energy ensures that sections do not stick to it. The flexible foil allows it to slide over the substrate and to push the ribbons inside.

The microfluidic system with low Reynolds number immobilizes the position of the section ribbon inside the channel. This allows the substrate to be moved to the next collection position without a further position change of the section ribbon relative to the substrate. At this point a new collection cycle can start by sectioning a new ribbon.

When all channels on the substrate are filled with sections, the substrate is slowly lifted to ultimately define the section position. The lifting occurs with $10 \frac{\mu\text{m}}{\text{s}}$ for a period of 5 min. The sections settle on the substrate due to the evaporation of the remaining water film. The channel surface is hydrophilic which aides a wrinkle free deposition.

3.2.1 Model of the Channel Wetting

The presented microfluidic channels form on the carrier substrate by a site-selective wetting of hydrophilic areas with a hydrophobic surrounding containment as illustrated in Figure 3.4. This section provides a mathematical description of the channel wetting. First the dominating forces in the channel wetting are identified and the validity of the description shown. A model for a **straight part** of the channel is derived and the physical limitations shown. The last part deals with the effects that occur at the **channel opening and end**.

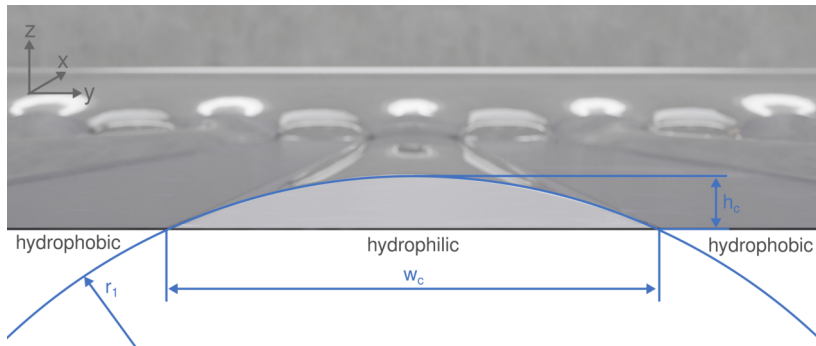


Figure 3.4: Cross section (blue) in a straight part of a water channel formed on a structured substrate with a hydrophilic channel (center) and a hydrophobic enclosure (left and right). The channel width in y direction is defined by the width of the hydrophilic area w_c . The first principal radius of curvature of the water surface lies r_1 in the y - z plane. The second principal radius is equal to infinity as the cross section does not change in a straight part of the channel and therefore no curvature exists along the x axis. For a constant pressure the water film takes the shape of a circular segment and the Young-Laplace equation can be used to calculate the curvature radius. The height of the fluid film h_c is defined by the circular segment with r_1 and w_c .

A central question is: What is the driving force that forms the water channels on the structured hydrophilic areas and which parameters influence the channel height? For simplification first a cross section is described that does not change over the length of a channel, this holds for the **straight part of a channel** as depicted in Figure 3.4. In this simplified model the channel cross section in the y - z -plane remains constant along the channel length in x direction and influences of the channel opening and end are neglected.

The channels can be wetted due to spontaneous capillary flow or through the hydrostatic pressure caused by an immersion of the substrate in the trough. For spontaneous capillary flow to occur, the resulting surface must be a minimal energy surface when the channel is wetted by the fluid. Berthier et al. describe the condition for spontaneous capillary flow (SCF) by

$$\frac{w_f}{w_s} < \cos \theta, \quad (3.4)$$

where w_f is the free part of the perimeter in contact with air, w_s the part of the perimeter wetting the surface and θ the contact angle of the fluid on the to be wetted surface [78].

Channels formed on the surface by a contrast of wettability do not have a physical lateral boundary that encloses the fluid. Thus the wetting surface w_s is equal to the channel width w_c and always smaller than w_f . It can be concluded, that the left side of Equation 3.4 always yields a value equal or greater than one. As the cosine can reach a maximum of one for an ideal contact angle of zero, the left side of the equation must always be equal or greater than the right side. Therefore the condition for spontaneous capillary flow results in a contradiction for surface structured channels as

$$\frac{w_f}{w_s} > 1 \quad \perp \quad \frac{w_f}{w_s} < \cos \theta. \quad (3.5)$$

As the channels are not wetted by spontaneous capillary flow, the driving force of the wetting must be the hydrostatic pressure caused by the immersion of the substrate below the trough fluid level. The hydrostatic pressure is defined by

$$\Delta p = \rho g h_i, \quad (3.6)$$

where ρ is the fluid density, g is the gravitational constant and h_i is the height distance of the substrate surface to the fluid level in the trough [79, 80].

The counter acting capillary pressure is given by the Young–Laplace Equation

$$\begin{aligned} \Delta p &= -\gamma \left(\frac{1}{r_1} + \frac{1}{r_2} \right) \\ &= -\gamma H_f, \end{aligned} \quad (3.7)$$

where Δp is the pressure difference, γ is the surface tension and r_1 and r_2 are the principal radii of curvature [79, 80].

The curvature can also be expressed by the mean curvature H_f or the principal curvatures k_1 and k_2 which are the reciprocal of the radii of curvature. All points on the fluid surface with the same pressure share the same mean curvature H_f . On the surface of a volume with constant pressure, a change in the principal curvature radius r_1 is accompanied by a change of r_2 , in order to keep the mean curvature constant. The definition of the mean curvature in microfluidics H_f differs from the mathematical mean curvature H by a factor of two

$$H_f = 2H = k_1 + k_2 = \left(\frac{1}{r_1} + \frac{1}{r_2} \right). \quad (3.8)$$

The gravitational force scales with the volume, while the surface tension force scales with the surface. Thus depending on the length scales either one or the other becomes the dominating force. The Eötvös number EO , also called the Bond number Bo , gives an indication whether the gravitational influence on the fluid shape can be neglected in a microfluidic description. The dimensionless

Eötvös number thereby compares gravitational forces of a volume to the tension forces of the surface. The Eötvös number is defined by

$$E_o = \frac{\rho g L^2}{\gamma}, \quad (3.9)$$

where L is the characteristic length [79, 80]. For the cross section of a channel, the characteristic length is given by the channel width w_c . The calculation of the Eötvös number for a typical channel with w_c of 1 mm and water as the wetting fluid gives a value of

$$E_o = \frac{\rho_{water} g L^2}{\gamma_{water}} = \frac{998.2 \frac{\text{kg}}{\text{m}^3} \times 9.81 \frac{\text{m}}{\text{s}^2} \times 1 \text{ mm}^2}{72.75 \times 10^{-3} \frac{\text{N}}{\text{m}}} \approx 0.135. \quad (3.10)$$

The value is much smaller than one and thus the surface tension force influence can be assumed to be much higher than the gravitation force influence of the contained volume. It is therefore valid to assume that the shape is dominated by the surface tension forces and the hydrostatic pressure does not change much in the contained volume. The hydrostatic pressure of Equation 3.6 and the capillary pressure of Equation 3.7 are then approximately equivalent and the equations can be combined to give the mean curvature of the fluid surface H_f by

$$H_f \approx \frac{\rho g h_i}{\gamma}. \quad (3.11)$$

This equation describes the shape of the fluid film formed on a channel as a surface with constant mean curvature H_f . The driving forces in this model are the hydrostatic pressure and the counter acting surface tension force.

While Equation 3.11 yields a valid approximation of the curvature of each point on the formed fluid film, the description of the shape requires the solution of the ordinary differential equation system for a three dimensional body under the constraints of the channel geometry.¹ A simple two dimensional solution for the

¹ A software like surface evolver can be used to find a numerical solution for the problem

shape problem can be found for a cross section in a straight part of the channel, as depicted in Figure 3.4. In this cross section, the first principal curvature radius r_1 is equal to the curvature of the water surface and the second principal curvature radius r_2 is equal to infinity as the cross section does not change in a straight part of the channel. Therefore no second principal curvature along the length of the channel is present and the mean curvature H_f is only defined by r_1 . Equation 3.11 then reduces to

$$r_c = r_1 = \frac{\gamma}{\rho g h_i}. \quad (3.12)$$

Thus the solution to the shape problem in a cross section is a simple circular segment. The curvature of the water surface r_c describes the radius of the circular segment and the channel width w_c defines the chord length by constraining the start and end points of the circular segment. The height h_c , width w_c and radius r_c of a circular segment are related by

$$r_c = \frac{4h_c^2 + w_c^2}{8h_c}. \quad (3.13)$$

The solution of this quadratic equation for the channel height h_c yields

$$h_c = r_c \pm \sqrt{r_c^2 - \left(\frac{w_c}{2}\right)^2}. \quad (3.14)$$

The two solutions of this equation represent two possible shapes of the fluid film cross section. The smaller solution represents a flat-shaped circular segment while the bigger solution represents a bulbous-shaped circular segment. Both solutions share the same curvature, as required by Equation 3.13. If the radius r_c is equal to half of the channel width w_c , the solutions coincide and the circular segment forms a semicircle with the highest possible curvature. The solutions of the two dimensional shape problem for a given curvature are depicted in Figure 3.5.

The hydrostatic pressure is defined by the immersion depth h_i . Therefore to assess the maximum achievable channel height, the maximum immersion depth is of importance. The maximum immersion depth $h_{i,max}$ is reached just before the

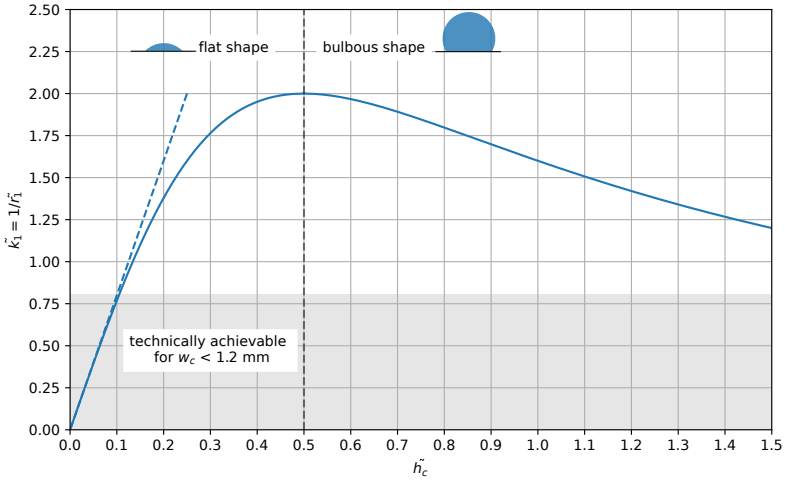


Figure 3.5: Plot of the dependency of the channel cross section curvature \tilde{k}_1 to the channel height \tilde{h}_c in a circular segment that models a fluid channel. The values are normalized to the channel width w_c . The grayed area shows the curvature that can be achieved by the immersion of 5 mm and proposes a technical limit for a 1.2 mm wide channel. The dashed line shows the series approximation of second order, which is visibly a good fit in the relevant region.

substrate is flooded from the substrate edges. An approximation of the theoretical maximal depth is given by the equivalent description as the height of a large puddle of fluid, before it starts to spread further laterally on a substrate given by

$$h_{i,max} = 2 \sin\left(\frac{\theta}{2}\right) \sqrt{\frac{\gamma}{\rho g}}, \quad (3.15)$$

where θ is the contact angle of the fluid on the substrate [79, 80]. The contact angle θ_{FDTS} of the used FDTS functionalization is given in literature with values

close to 116° [3]. Substrates coated with FDTS and submerged in water have a theoretical maximal immersion height of

$$\begin{aligned} h_{i,max} &= 2 \sin\left(\frac{\theta_{FDTS}}{2}\right) \sqrt{\frac{\gamma_{water}}{\rho g}} \\ &= 2 \sin\left(\frac{116^\circ}{2}\right) \sqrt{\frac{72.75 \times 10^{-3} \frac{\text{N}}{\text{m}}}{998.2 \frac{\text{kg}}{\text{m}^3} * 9.81 \frac{\text{m}}{\text{s}^2}}} = 4.62 \text{ mm} . \end{aligned} \quad (3.16)$$

The in reality achievable height is smaller than this theoretical maximum, as it is affected by the substrate geometry such that the substrate edges are flooded earlier.

The contact angle of the hydrophobic containment enforces another constraint on the channel height. The contact angles at the sides of the circular segment must be smaller than the contact angle of the hydrophobic containment. If the angle of the circular segment advances above the contact angle θ then the fluid starts to wet the containment as expressed by

$$h_{c,max} = \frac{w_c}{2} \tan\left(\frac{\theta}{2}\right) . \quad (3.17)$$

The channel height h_c must be smaller than the channel height $h_{c,max}$. For the flat-shaped solution of Equation 3.14 this holds always true. For the higher bulbous-shaped solution the condition is expressed by the inequality

$$\frac{w_c}{2} \tan\left(\frac{\theta}{2}\right) > r_c + \sqrt{r_c^2 - \left(\frac{w_c}{2}\right)^2} . \quad (3.18)$$

The solution of the inequality for the channel width w_c yields the condition

$$w_c > \frac{4r_c \tan\left(\frac{\theta}{2}\right)}{\tan^2\left(\frac{\theta}{2}\right) + 1} . \quad (3.19)$$

The evaluation of this condition for a maximal immersion height $h_{i,max}$ of 4.62 mm yields a condition of $w_c > 2.78$ mm. This implies that for the desired microfluidic channels, with a channel width close to 1 mm, the second bulbous-shaped solution can technically not be achieved in a straight part of the channel. Those constraints restrict, like indicated in Figure 3.5 by the highlighted area, that only channels with a normalized curvature $\tilde{k}_1 < 0.8$ can be achieved.

Equations 3.12 and 3.14 can be combined to calculate the possible solution of the channel height h_c for a given immersion depth h_i and channel width w_c by

$$h_c = \frac{\gamma}{\rho g h_i} - \sqrt{\left(\frac{\gamma}{\rho g h_i}\right)^2 - \left(\frac{w_c}{2}\right)^2}. \quad (3.20)$$

When the condition $r_c \gg w_c$ holds, which is true for the discussed channels, a series expansion of Equation 3.20 at $h_i = 0$ yields the approximation of the channel height

$$\begin{aligned} h_c &\approx \frac{w_c^2}{8r_c} \\ &\approx \frac{w_c^2 \rho g h_i}{8\gamma}. \end{aligned} \quad (3.21)$$

This approximation is valid for discussed channels and indicates that the channel height h_c is proportional to the square of the channel width w_c .

In the above used simplified description of a channel by a cross section, the effects of the **channel opening and end** are neglected. The discussed cross sections represent straight parts of the channel where no second principal curvature k_2 exists. This model does therefore not provide an accurate description of the channel height when the cross section changes. The capillary pressure inside the channels is still defined by the immersion dept h_i , but the resulting mean surface curvature in the Young–Laplace Equation 3.7 is the sum of both principal curvatures. When the channel width gets smaller, the second principal curvature k_2 takes a positive sign, respectively a negative sign when the width increases.

At the channel end, the channel width decreases and thus k_2 takes a positive sign. This implies that less curvature can be attributed to the first principal curvature k_1 . Therefore the channel height gets smaller at the channel ending as depicted in Figure 3.6C. Sharp corners at the channel end cause a high second principal curvature and thus a small first principal curvature. It is therefore beneficial to smooth the corners at the channel ending.

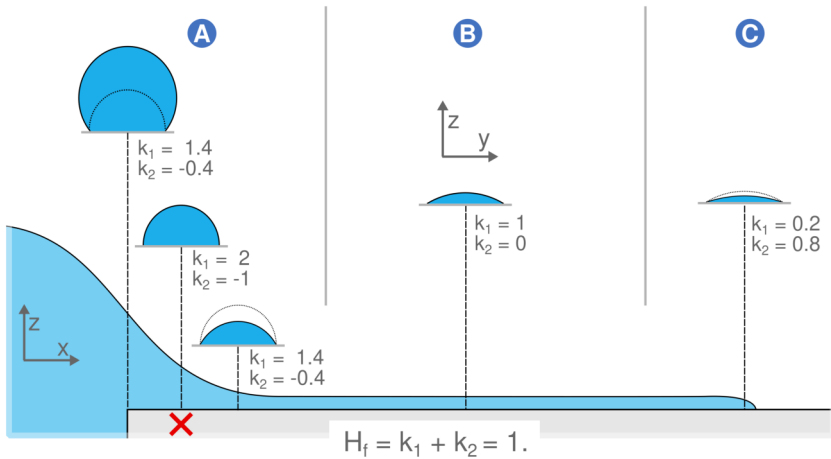


Figure 3.6: Cross section along the length of a channel in the xz -plane with relevant depictions of cross-sections in the yz -plane for: A) channel opening B) straight part and C) channel ending. Exemplary values for the first and second principal curvature are added. The mean curvature is assumed to be one. The cross section with the lowest second principal curvature (red cross) imposes a local minimum, that is the origin of a channel contraction and finally causes a separation between channel and fluid reservoir.

At the channel opening the situation is reversed. The channel width increases as the channel extends to the fluid reservoir. This causes a negative second principal curvature. To satisfy the Young–Laplace equation, more curvature must be attributed to the first principal curvature. This increases the channel height compared to the height observed in a straight part of the channel as depicted in Figure 3.6A. Nevertheless, for channels created by a contrast of wettability a drying of channels at the opening is observed [98]. The channels first start

to contract shortly behind the channel opening until the channel is completely separated from the fluid reservoir. Without further fluid inflow from the reservoir, the channels evaporate completely within minutes as discussed in Section 3.24. The contraction happens because the rectangular channel opening results in a surface with lower total energy in the dewetted state despite the channel being higher compared to the straight part. The channel is immersed below the trough fluid level by a multiple of the channel height. The channel height does not suddenly change but instead smoothly transit into the channel height of the straight channel part as shown in Figure 3.6B. The critical point in this transition is the semicircle shaped cross section as it requires the lowest second principal curvature to fulfil the Young–Laplace equation. Left of this point the cross section has a bulbous-shape and right of it a flat-shape. Both shapes have a lower curvature than the semicircle. This implies that the semicircle is the point with the lowest second principal curvature. This point is the origin from which a contraction of the channel starts that ends in a complete separation of the channel from the fluid reservoir.

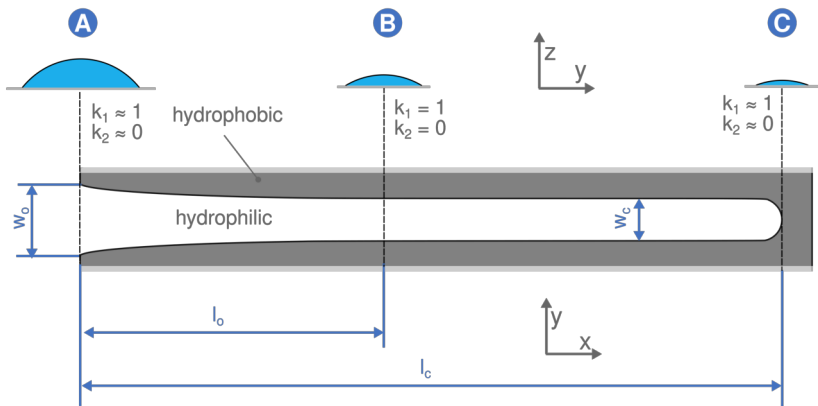


Figure 3.7: Cross section along the length of optimized channel in the xy -plane with relevant depictions of cross-sections in the yz -plane for: A) channel opening B) straight part and C) channel ending. Exemplary values for the first and second principal curvature are added. The mean curvature is assumed to be one. The cross section changes steadily in the first half and avoids a semicircle-shape that causes contraction.

The problem of channel contraction can be prevented by avoiding a semicircle shape for the cross section. For this reason the channels used for the deposition of ultramicrotome sections have a modified channel opening. The modified channel geometry is displayed in Figure 3.7. The channel opening has an elliptic beveling with an axis ratio of 20:1. The channels used for deposition have the following dimensions:

- $w_c = 1.2$ mm
- $l_c = 20.5$ mm
- $w_o = 2.1$ mm
- $l_o = 9$ mm
- $h_c < 121$ μm (by Equation 3.20)

These dimensions allow seven channels on a 22 mm wide carrier substrate. To further assist a smooth transition of the channel height, the substrate is tilted by 5° such that the channel openings lie closer to the water level in the trough. With a modified channel geometry and a tilted substrate, the stability of the channels is increased to more than 1 h in the wetted state. This time is sufficient for a machine-based section collection. The wider opening also supports the entering of the section ribbon.

The next Section 3.2.2 describes the fluidic properties of the channels based on the derived dimensions.

3.2.2 Description of the Fluid Mechanics inside Water Channels

The floating sections in the water channels form a fluidic system in which the movements of the components are influenced by fluidic forces. To utilize the properties of the channels created by a structured contrast of the wettability, it is important how the movement of the carrier substrate influences the movement of the collected sections. When the substrate is in motion relative to the sections, two scenarios are possible. Either the inertial forces dominate and permit a relative

motion between sections and substrate, or the viscous forces dominate and the section motion follows the substrate motion. The dimensionless Reynolds number relates both inertial and viscous forces in a fluidic system and indicates which force dominates. For $Re \ll 1$ the viscous forces dominate while for $Re \gg 1$ the inertial forces dominate the motion. A miniaturization tends to favor low Reynolds numbers [81] and thus small channels open up the possibility, that the sections can be coupled to the carrier substrate by dominating viscous forces. The Reynolds number is defined by

$$Re = \frac{\rho v L}{\mu}, \quad (3.22)$$

with the characteristic length L and the relative velocity v . The smallest length scale of the system should be chosen as the characteristic length as it will contribute strongest to stabilize the flow [80]. The small height of the channels is beneficial in this respect as it restrains the characteristic length to small values. The calculation of the Reynolds number for a typical channel height of $121 \mu\text{m}$ (derived in Section 3.2.1), and a relative velocity of $1 \frac{\text{mm}}{\text{s}}$ gives a value of,

$$Re = \frac{\rho_{water} v L}{\mu_{water}} = \frac{998.2 \frac{\text{kg}}{\text{m}^3} * 1 \frac{\text{mm}}{\text{s}} * 121 \mu\text{m}}{1 \frac{\text{kg}}{\text{m s}}} \approx 1.2 \times 10^{-4}. \quad (3.23)$$

The calculated Reynolds number can be put into context by comparing it with the Reynolds number of a moving bacterium (1×10^{-6}) and a human swimming in water (1×10^6). The order of magnitude of the calculated Reynolds number is much smaller than one and thus the viscous forces are dominant [80]. Hence, given the small dimensions of the fluidic system, the sections do in relation not have a significant inertia and follow the fluid motion. In contrast to freely floating sections the fluid acts significantly more rigid in the small channels. Compared to previous methods, the here presented shallow microfluidic channels created by a contrast of wettability open two interesting applications for the collection of sections. As the fluid acts rigid and is free of turbulent flow, no previous section fixation on the carrier substrate by a partial or complete physical attachment is

required. Secondly, as the section position follows the substrate movement due to the viscous forces, the sections can be re-positioned by the drag of the carrier substrate. These properties are exploited in the presented automated collection method to implement the tasks of section separation and section localization (compare to Section 2.3.2).

The reduced channel volume opens up new possibilities for the section collection but is also more effected by evaporation. In the next Section 3.2.3 a fluid evaporation model is used to assess the evaporation rate of microfluidic channels.

3.2.3 Fluid Evaporation

A fluid surface exposed to the ambient experiences evaporation. The shallow height of the fluid film in the microfluidic channels, although having positive properties that open new possibilities to the section collection problem, makes the evaporation problem prominent. The evaporation of a liquid depends on the vapor pressure, exposed surface area of the fluid as well as environmental conditions such as temperature, humidity and ventilation [82].

Hummel et al. develop a model for the evaporation of an open liquid surface

$$G = 8.68 * 10^{-7} * \frac{M^{0.833} * p_v * \sqrt{v_z} * (1/28.97 + 1/M)^{0.25}}{z * T^{0.05}}, \quad (3.24)$$

which yields the fluid evaporation rate G in $\frac{\text{g}}{\text{s cm}^2}$ and requires only the molar mass of the liquid M in $\frac{\text{g}}{\text{mol}}$, the vapor pressure p_v in kPa, the air flow speed v_z in $\frac{\text{cm}}{\text{s}}$, the absolute temperature T in K and the length of the air/liquid interface in the direction of the flow z in cm [83]. The model is based on a penetration model for diffusion of an evaporating liquid into a flowing gas using Fick's second law of diffusion and suitable for low air speeds smaller than $50 \frac{\text{cm}}{\text{s}}$ [82].

The time required for the evaporation of the channel volume V_c with the exposed surface area S_c is

$$t_e = \frac{V_c \rho}{G * S_c}. \quad (3.25)$$

The cross section area A_c of a channel is a circular segment defined by the channel width w_c and the channel height h_c . The channel height h_c can be well approximated by Equation 3.21 which gives

$$\begin{aligned} A_c &= \frac{2}{3} w_c h_c \\ &\approx \frac{w_c^3 \rho g h_i}{12 \gamma}. \end{aligned} \quad (3.26)$$

The length of the surface w_f in a cross section for the flat-shaped channels is approximately the channel width w_c and defined by

$$w_f \approx w_c. \quad (3.27)$$

The channel volume V_c can be calculated from Equation 3.26 by multiplication with the channel length l_c

$$V_c \approx w_c^3 l_c \frac{\rho g h_i}{12 \gamma} \quad (3.28)$$

respectively the surface area of a channel S_c from Equation 3.27 as

$$S_c \approx w_c l_c. \quad (3.29)$$

Equation 3.28 indicates that the channel volume scales cubed to the channel width w_c . On the contrary, Equation 3.29 shows that the channel surface area only scales linearly with the channel width w_c . The time required for evaporation is proportional to the volume and inversely proportional to the surface area. Therefore the channel width has a quadratic influence on the evaporation time. A half as wide channel evaporates in a quarter of the time without fluid inflow. The fluid inflow is defined by the cross section of the channel and accordingly also

affected by the cubic scaling of the cross section area. This indicates that a further miniaturization of the channels can cause an instability due to fast evaporation.

For an estimation of the problem, the evaporation model in Equation 3.24 is evaluated with the system parameters. During section acquisition the channels are surrounded by the water surface of the trough with a width of 53 mm and length of 58 mm. For the estimation of the evaporation rate the complete trough area is considered, as it defines the open fluid surface. Accordingly the length of the air/liquid interface z is chosen as the minimal dimension of the trough with a value of 53 mm. This also shows that the modification of the trough width is beneficial in regard to fluid evaporation. For the room air flow speed v_z a typical value of $2 \frac{\text{cm}}{\text{s}}$ is assumed [84]. The room temperature is assumed to be 20°C . The calculation of the model yields the values provided in Table 3.1 which also compares the values to another trough fluid.

Table 3.1: Comparison of the modeled evaporation for water and ethylene glycol for: $T = 20^\circ\text{C}$, $z = 53 \text{ mm}$, $v_z = 2 \frac{\text{cm}}{\text{s}}$, $h_i = 4.8 \text{ mm}$, $w_c = 1.2 \text{ mm}$

Property	Water	Ethylene Glycol
h_c	121 μm	224 μm
V_c	19.4 μL	35.85 μL
S_c	0.24 cm^2	0.24 cm^2
G	$2.48 \times 10^{-6} \frac{\text{g}}{\text{s cm}^2}$	$2.57 \times 10^{-8} \frac{\text{g}}{\text{s cm}^2}$
t_e	54 min	10 769 min

The model is calculated for a relative humidity of zero, so the evaporation rate is a worst case assumption and the real value will be lower. Also the model does not consider a fluid inflow that can compensate for an evaporation. It takes 54 min for an evaporation of the complete fluid volume of the used channels under this worst case scenario. A typical section collection takes approximately 30 min, so the evaporation does not limit the collection process. Figure 3.8 shows a plot of the estimated evaporation time over the channel width for different ambient

temperatures T . It is noticeable that for a channel width of 0.6 mm the evaporation time at an ambient temperature of 20 °C is only 14 min which is not sufficient for a collection of sections. The evaporation thus imposes a limit on the usable channel width at a normal room temperature of 20 °C. The evaporation time for the same channel width and an ambient temperature of only 10 °C is already 25 min, which is close to the time required for the section collection. The chosen channel width of 1.2 mm provides channels with a good stability at common room temperatures. Also at a higher ambient temperature of 25 °C the evaporation time for this channel width is still 40 min and above the required collection time.

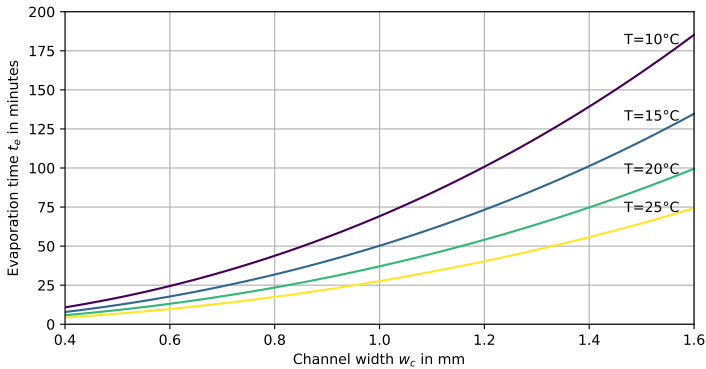


Figure 3.8: a) Plot of the expected evaporation time t_e over the channel width w_c for for different ambient temperatures $T = 10^\circ\text{C}$, 15°C , 20°C and 25°C . Other model parameters: $z = 53\text{ mm}$, $v_z = 2\frac{\text{cm}}{\text{s}}$, $h_i = 4.8\text{ mm}$. The source code of the plot is shown in Appendix A.3.

The channel stability to evaporation can be further improved by a locally increased ambient humidity and a shielding from air flow. This can be achieved by a small environmental chamber around the knife trough, as for example seen in Section 2.2.2. This also brings the benefit that other environmental influences like local cooling due to air flows can be reduced and thus the cutting quality increased. Because the automated acquisition does not require any manual manipulation, the environmental chamber can be a completely isolated system without holes for

manual access. In the here presented methodology the requirements are however directly compatible to recommended ambient conditions of the ultramicrotome and for the reason of easy accessibility during the development of the methods, no environmental chamber is used.

Another method to improve the stability could be the use of a different trough fluid. As seen in Table 3.1, the usage of ethylene glycol greatly improves the stability of the channels on the substrate. This is attributed to two properties of ethylene glycol. First, its surface tension is with a value of $48.02 \times 10^{-3} \frac{\text{N}}{\text{m}}$ smaller than that of water with $72.75 \times 10^{-3} \frac{\text{N}}{\text{m}}$. This increases the volume contained in the channels. Second, the vapor pressure of water is 2.34 kPa at room temperature, while that of ethylene glycol is only 0.01 kPa. This decreases the evaporation rate. For the reason of its better properties in the sectioning process, water is used in the presented methodology but ethylene glycol could also be an interesting fluid for the section collection in cryo-ultramicrotomy.

3.2.4 Site-selective Modification of Wettability

The wettability of a substrate surface depends on its surface roughness and its surface free energy (SFE). The SFE is an important property which can be modified for example by chemical functionalization to tailor the surface interaction with organic, inorganic or biological materials to the specific application. Depending on the task, a substrate surface is partly or entirely functionalized to create application specific patterns. A widely applied method to chemically modify the properties of oxidic or oxide-like substrate surfaces is silanization, where a molecular bond is formed by hydrolysis of a silane/siloxane and condensation with an OH-group on the substrate surface. This technique is used to form self-assembled monolayers (SAMs) or thin films with molecular thickness [85].

Perfluorodecyltrichlorosilane (FDTS) is used to obtain a well-defined difference in the SFE between hydrophilic and hydrophobic areas on the carrier substrate surface. FDTS is known to form self-assembled monolayers. The molecules form covalent silicon–oxygen bonds to free hydroxyl (–OH) groups, such as present

on the surfaces of glass, ceramics, metals or silica [86]. These materials are also common for carrier substrates in the acquisition of serial sections in Array Tomography. The fluorinated tail group is responsible for the chemical inertness and low surface energy.

Patterns can either be created in subtractive or additive processes. Subtractive processes facilitate silanization of the entire substrate surface by liquid or vapor phase deposition and subsequent patterning, e.g. by plasma or laser based processing [87]. Additive processes directly form the patterns on a substrate with inked stamps, e.g. micro contact printing [88, 89]. A comparison of different methods for the creation of patterns with well-defined difference in the SFE is found in [90, 98].

To create patterns with a contrast in the SFE on the carrier substrates, a subtractive process is used. The patterning process is based on gas phase silanization to form a thin hydrophobic FDTS monolayer followed by site selective oxygen plasma induced decomposition of the FDTS in unmasked regions to create hydrophilic areas. The deposition in vapor phase is selected because it is favourable in terms of uniformity and requires only minimal amounts of FDTS. Furthermore, unwanted growth of agglomerations, which has been observed after complete immersion in liquid phase, should be avoided [91].

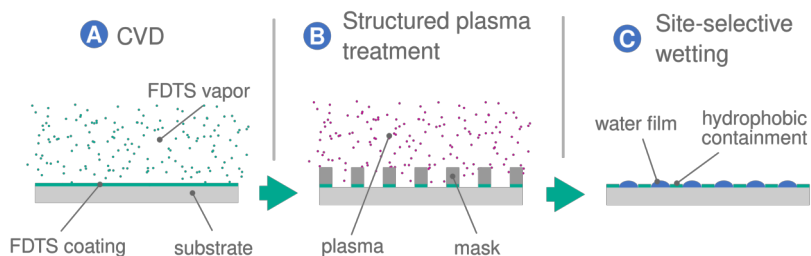


Figure 3.9: Process steps of vapor phase silanization, followed by structured plasma treatment to create patterns with different wettability.

A 10 % solution of FDTS in heptane is used for the preparation of a hydrophobic coating. The chemical functionalization is performed by chemical vapor deposition (CVD) as illustrated in Figure 3.9A. Complete silanization of the substrate surface is performed by arranging substrates vertically with 10 mm spacing in a sealed container with a volume of 900 cm³. The container is placed in an oven preheated to 55 °C to allow homogeneous heat distribution and then 150 μL of the silanization solution are added to perform vapor phase silanization for 60 min at 55 °C. Subsequently, the substrates are rinsed with DI water. The substrates are cleaned with isopropanol and a clean room tissue to remove a potential excess polymer layer on the substrate surface formed during silanization.

The silanized surface is then covered with a mask that protects the FDTS coating at the contact surfaces and allows plasma treatment at the exposed surfaces as illustrated in Fig. 3.9B. The plasma treatment is performed in a glow discharge system (PELCO easiGlow, Ted Pella) with a nominal current of 20 mA in positive glow discharge head polarity. The process time is 150 s at a chamber pressure of 0.25 mbar. The low pressure increases the mean free path, making the plasma treatment more directional and prevents a treatment of areas covered by the mask. The mask is manufactured from Polylactic acid (PLA) printed in Fused Filament Fabrication (FFF). FFF printing is used because of the fast manufacturing times which allow the testing of different mask designs and thus channel patterns on the carrier substrates. Different methods of masking the substrates are presented as an outlook in Section 4.4. As a process gas during the plasma treatment the composition of the room air is sufficient. For a better process control, it is also possible to use pure oxygen during the treatment [98].

After the plasma treatment the carrier substrate has the desired pattern with a well-defined difference in the SFE that forms the channels for the collection of section ribbons as depicted in Figure 3.9C. The plasma treated areas are hydrophilic because of a decomposition of the FDTS coating. Because of the reactive polar groups on the surface, the plasma treatment is an effect that decreases over time when exposed to the ambient air. For this reason the time between plasma treatment and submersion in the knife trough should be kept minimal. Immersed in water the hydrophilic areas remain hydrophilic.

3.3 Machine-based Section Monitoring

Sections are visually monitored during the section acquisition process by observation of the top light reflection on the water surface of the knife trough. The sections are visible in the reflection by the interference colors which occur at thin films. A simple model that is capable to monitor sections inline and does not rely on human interpretation is developed. Changes to the optic system of the ultramicrotome are realized that increase the signal to noise ratio for the algorithmic section monitoring but also improve the human-based visual monitoring.

Thin films and thus also the floating ultra-thin sections cause light interference through a optical path difference by passing through materials with different refractive index n . The electromagnetic wave character of light allows two waves to interfere, that are reflected at the top and the bottom interface of the thin film. The interference can either be constructive or destructive depending on the optical path difference. For interference to occur, the optical path difference must be within the coherence length of the interfering light. Therefore white light interferes only at thin films and for thicker films monochromatic light is required. An example for the interference of white light on thin films are the vibrant colors that occur when a thin oil film forms on top of a water surface.

For the description of thin film interference phenomena it is sufficient to describe light by its wave nature. The interference term

$$I = I_1 + I_2 + 2\sqrt{I_1 I_2} \cos(\delta) \quad (3.30)$$

describes the total irradiance I for two coherent light rays interfering with an optical path difference δ [70]. The cosine function in Equation 3.30, creates a periodic variation of the total irradiance as a function of the path difference δ which causes the typical periodic interference patterns with local minima respectively maxima.

The optical path of the machine-based section monitoring uses an arrangement of a top light source, which is reflected on the water surface of the knife trough and

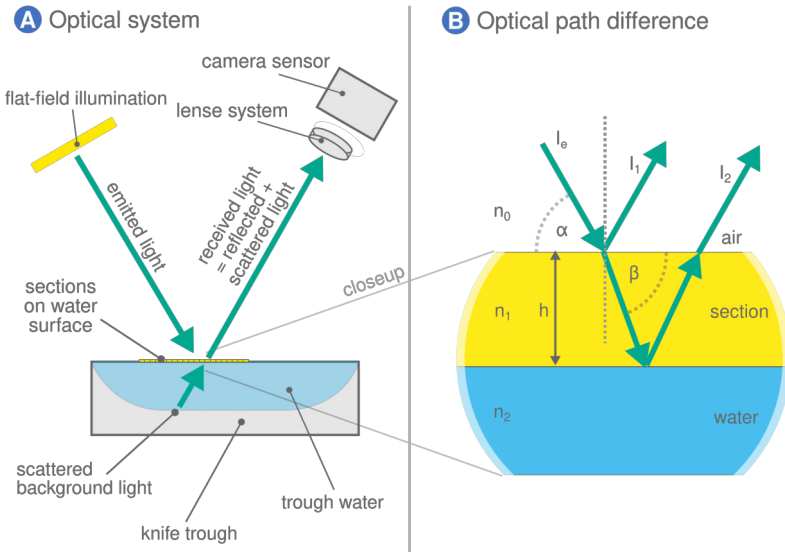


Figure 3.10: A) Optical system used to capture the interference colors of the ultra-thin sections. B) Ray paths causing the optical path difference by a first partial reflection on the air/section interface and a second partial reflection at the interface section/water.

captured by a camera mounted behind a microscope lens system. Figure 3.10B depicts the light paths for two reflected and interfering waves passing through an ultra-thin section and received by the camera. Additional light paths which are formed by multiple reflections on the upper and lower interface of the thin film can be neglected because they do not significantly contribute to the intensity of the reflected wave [92]. An amount of an initially emitted light ray I_e is reflected at the first interface between air and section and creates the first interfering light ray with intensity I_1 . The amount of light that is reflected at the interfaces is defined by the Fresnel equations. The factor depends on the incidence angle α , as well as the polarisation and the materials refractive index. For the presented algorithm the values are indirectly derived by the subsequent curve fitting algorithm and can be considered as system constants, as they do not depend on the section thickness h . The reflection term R_1 contributes for the amount of the light that is reflected

at the first interface. Similarly R_2 represents the portion of the initial emitted ray that passes through the section material and is reflected at the second interface from section material to the water below. An absorption in the section material can be neglected, as macroscopic epoxide sample blocks are almost transparent and the ultra-thin sections can thus not provide a substantial absorption.

The optical path difference between the two paths I_1 and I_2 is given by

$$\delta = \frac{4\pi n_1}{\lambda} \cos(\beta)h - \varphi_n, \quad (3.31)$$

where β is the angle of refraction which is derived from the angle of incidence α by Snell's law and φ_n is an additional phase shift at the interface of the reflections caused by the rays entering an optical thicker or thinner medium [70]. The additional phase shift for the transition to an optical thicker medium is π and not present for the transition to a thinner medium. For epoxide sections floating on water with a typical refractive bigger than that of water, an additional phase shift φ_n of π occurs. Equations 3.31 and 3.30 can be combined to yield the irradiance for a given section thickness and wavelength as

$$I(d, \lambda) = I_e \left(R_1 + R_2 + \sqrt{R_1 R_2} \cos\left(\frac{4\pi n_1}{\lambda} \cos(\beta)h - \varphi_n\right) \right). \quad (3.32)$$

The variables R_1 , R_2 , I_e , n_1 and λ can be considered as system specific and thus the irradiance model is reduced to

$$I(d, \lambda) = p_0 + p_1 \cos(p_2 d - \pi), \quad (3.33)$$

with the three parameters

$$\begin{aligned} p_0 &= I_e(R_1 + R_2), \\ p_1 &= I_e \sqrt{R_1 + R_2}, \\ p_2 &= \frac{4\pi n_1}{\lambda} \cos(\beta). \end{aligned} \quad (3.34)$$

The parameters p_0 and p_1 describe the allocation of the light to interfering and non interfering portions. The parameter p_0 describes the portion of the light that is reflected without interfering, while p_1 describes the contribution of the interfering light to the captured light. The parameter p_0 also includes scattered background light (see Figure 3.13A). The parameter p_2 depends on the wavelength λ , the angle of refraction β and the refractive index of the section material. For a given illumination setup and section material these model parameters are constant.

Equation 3.33 describes the interference for a single wavelength. Such an ideal light source does not exist, as also lasers consist of a, while still very narrow, frequency band. For a range of wavelengths, the integral of the irradiance must be taken into account, in which maxima and minima of the irradiance for individual wavelengths occur at different thicknesses. A broad spectrum light source can be approximated by a narrowband light source with a reduced capability for interference [49]. No change is required to the model as this effect can be attributed by the parameter p_1 in the introduced model.

The camera sensor consists of a Bayer filter which separates the received light into the spectral ranges associated with red, green and blue. Therefore Equation 3.33 can be used to model the irradiance I_r , I_g and I_b for the red, green and blue channel of the captured image. For a changing section thickness, the irradiance in each channel describes a curve in the three-dimensional RGB color space. A similar model has been used to estimate the thickness of sections deposited on silicon wafers [41], but requires calibration points to estimate the model parameters.

The parameters p_0 , p_1 and p_2 exist independently for each channel of the captured irradiances in red, green and blue ($p_{0,r}, p_{0,b} \dots p_{2,g}$). For the estimation of the model parameters without prior calibration, color samples for different section thicknesses are taken, without the requirement that the exact section thickness is known. These samples form a point cloud in the three-dimensional RGB color space. To estimate the model parameters, a curve fitting algorithm is used that adjusts the model parameters in such a way, that all the color samples lie as close as possible to the model curve. This curve fitting algorithm can estimate the parameters p_0 and p_1 but contains an ambiguity in the parameter p_2 . This can

be understood in the sense that p_2 is part of the parametric representation of the curve. For example all parameters p_2 can be multiplied with the same factor to give a different parametric representation of the curve that still has the same shape as the original curve.

To generate the samples for the estimation algorithm, a series of sections with increasing thickness can be obtained before the section acquisition is started. The set thickness of the instrument is not guaranteed to represent the actual thickness, but can be used to provide an estimated absolute reference for the relative thickness variations the algorithm delivers.

The camera images are captured in raw mode to provide the full 12 bit resolution depth of the camera sensor used (IMX252, Lt345RC, Lumenera) and to avoid information loss in the commonly used 8 bit non-linear sRGB format.

To estimate the model parameters the Limited-memory BFGS algorithm provided by the Python Scipy library is used with random starting points to avoid the trapping in local minima [75]. In the implementation the parameter $p_{2,g}$ is chosen as 0.030 to attribute for the ambiguity in the parameterisation. This value is close to real values determined from the nominal section thicknesses set on the instrument. Without this preset, the thickness estimation algorithm provides only relative numbers.

For interference to occur, the optical path difference δ must be lower than the coherence length of the interfering light source. If the path difference falls above the coherence length of the emitted light, the interference effect washes out and the resulting intensity is solely the sum of I_1 and I_2 [70]. The observation of interference is thus limited by the coherence of the light source and by the optical path difference δ . An approximation at which the diminishing of the interference effect occurs for a given film height h is given by

$$h \geq \frac{\lambda_1 \lambda_2}{\lambda_1 - \lambda_2}, \quad (3.35)$$

with λ_1 and λ_2 being the start and end of a uniform frequency spectrum [49]. For a typical blue LED with a FWHM (Full Width at Half Maximum) of 20 nm

around a wavelength of 450 nm the interference effect diminishes for film thicknesses greater than 10 μm . The presented thickness estimation algorithm neglects the modeling of the washing out due to non distinct wavelengths, as the effect is not dominant for the typical section thicknesses of less than 200 nm, which are a factor of 50 below this limit, in favor of a simple model.

The allocation of the reflected light into a part which is interfering and a non interfering part is given by the spectrum of the emitting light source. A spectrum with a narrower wavelength band allocates more of the reflected light to the interfering part. Non interfering light does not contain information that can be used to estimate the section thickness, thus a higher ratio of the interfering portion p_1 is desirable. An optimal light source should thus have narrow wavelength bands and scattered background light reduced. It is further beneficial that the wavelength bands are far away from each other.

A light source with a narrow frequency spectrum thus creates more distinct interference colors than a broad band light source [49]. As the emitting light source, a LED light with three local maxima in the spectrum for red, green and blue is chosen. The amplitude of the cosine function is however damped to a beat like pattern [49] due to the reduced capability of the short coherence length in thicker sections. As a homogeneous and bright flatfield illumination an edge lit display (Iphone 6 Backlight) is used. The spectrum of the used illumination is displayed in Figure 3.11. The spectrum shows distinct lobes for the red, green and blue wavelengths. Compared to fluorescence bulbs that were used in early ultramicrotomes, the spectrum is not as distinct, but favourable in terms of uniformity and thermal radiation. Thermal drift caused by the waste heat of the illumination has a negative impact on the cutting process and should therefore be minimal. The peak of the spectrum for the blue wavelength lies at 450 nm compared to 465 nm of a conventional ultramicrotome top light. The further gap to the peak of the green wavelength at 550 nm increases the spreading of the interference color curve, but is again not as good as the distinct peak in the blue spectrum for the fluorescence bulb at 440 nm.

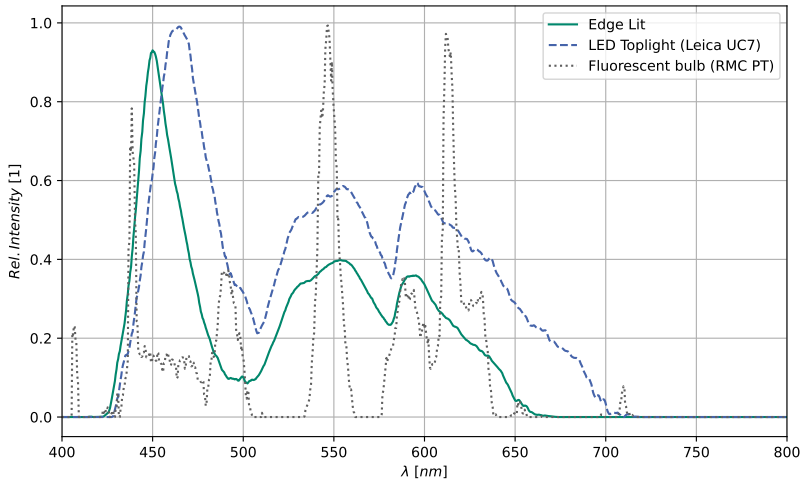


Figure 3.11: Spectrum of different top lights used for the section monitoring. The spectra are obtained from a custom top light built from an edge lit display illumination (Iphone 6), an ultramicrotome LED top light (Leica, UC7) and an ultramicrotome fluorescent bulb top light (RMC, Powerome). The edge lit display shows local maxima in the spectrum for blue, green and red perceived wavelengths and is comparable to the ultramicrotome LED top light. The spectrum of the fluorescent bulb shows the most distinct maxima in the spectrum.

A computer model is not affected by non-linearities in the perceived color difference that humans experience. Therefore an evaluation of the interference colors by a computer algorithm yields more precise section thickness estimations. A computer takes each color channel individually into account and compensates flat slopes in the by humans perceived color difference with channels that have steeper slope. Figure 3.12 shows a comparison of the perceived color difference for a "warm" and a "cold" light source. The interference colors are noticeably different for a cold and a warm light source. Further it is noticeable that the perceptual color difference is not uniform. A cold light source is more uniform in the range of 80 nm to 140 nm but shows a strong peak at 180 nm to 230 nm. An operator must be aware of these effects to estimate the thickness correctly.

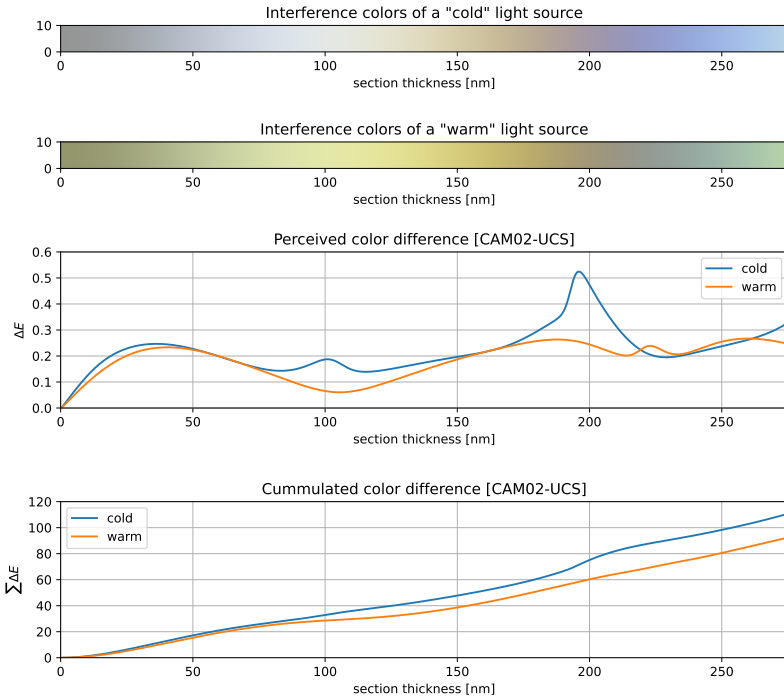


Figure 3.12: The two color bars in the top show the simulated interference colors of epoxide sections for a top light source with a "cold" color temperature of 6000 K and a "warm" light source of 3000 K. The lower part displays the perceived color difference according to the CAM02 color perception model [93]. An ideal light source for human visual section thickness estimation would show a flat curve. The cold light source (blue) shows a better performance at a section thickness of 100 nm as the curve stays closer to the value of $0.2\Delta E$, but has a strong peak at 190 nm, where the color quickly changes from yellow to purple to blue. This difference might also effect the judgement of a ultramicrotome operator, who is not aware of this change observing sections under a different color temperature. The last plot shows that the cold light source provides a bigger total space of perceived color difference.

The sections are only visible in the reflection of the light source. Therefore it is important to have a uniformly illuminated light source. The edge lit display has imprinted wave guides that emit light mostly perpendicular to the plane of

the light source. This decreases the amount of omnidirectional light that can be scattered by the background and superimposes with the reflected light. Figure 3.13 shows a comparison of the used flatfield illumination to a conventional top light. The picture taken with the flatfield illumination shows noticeably less background structure of the knife trough overlaying the reflection on the water surface. Another measure to reduce the light scattered in the knife trough is by changing the light absorption of the trough surface. The developed custom knives used for the automated section collection have a black coating to decrease the amount of background scattered light.

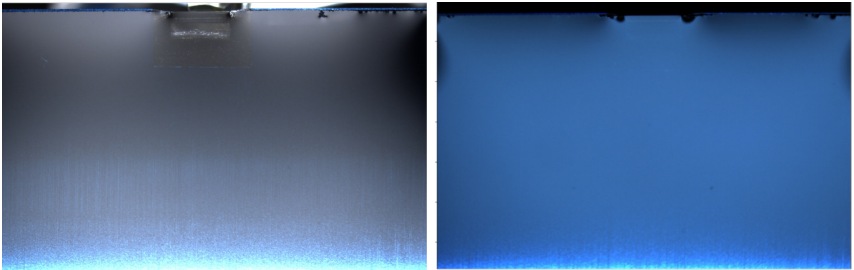


Figure 3.13: Left: Reflection of a fluorescent lamp with diffuser plate on the water surface of the trough. Right: Reflection of an edge lit illumination under similar conditions. The edge lit illumination is noticeably more uniform and less scattered light from the background of the knife trough is visible.

When a model is trained to represent the interference colors, a reverse operation is possible to determine a relative thickness information for a given captured color value. The implemented algorithm performs this operation by calculating the point on the curve that has the least geometric distance to the captured color. Through the calculation of the minimal distance, the captured color values do not need to lie exactly on the color model curve. This allows for a deviation from the model values for example caused by background objects or scattered light. The results of the algorithm are presented in Section 4.1.3.

4 Results & Discussion

This chapter summarizes and discusses the results of the developed machine-based section acquisition in Array Tomography. The first Section 4.1 describes the developed system by its components – a machine-based sample advance, section collection and section monitoring. Further, the developed methods are compared to the current state of the art. The second Section 4.2 evaluates the system performance on two representative samples from life science and material science. A conclusion is provided in Section 4.3. The last Section 4.4 gives an outlook to possible extensions of the developed acquisition method, for example the application in cryo ultramicrotomy or the collection of section arrays for TEM imaging.

4.1 Integrated System for Machine-based Section Acquisition

Based on the developed and selected methods a system for the machine-based section acquisition in Array Tomography is integrated into an ultramicrotome. The system is a retrofittable extension to an existing ultramicrotome. The following three Sections describe the system oriented on the conceptual separation of the Array Tomography workflow into the tasks of pre-sectioning sample alignment and advance, section collection and section monitoring as illustrated in Figure 4.1. The developed machine-based section acquisition for Array Tomography includes changes to the ultramicrotome, adaptations of existing methods and novel methods to provide a versatile but highly automated and integrated solution for the Array Tomography workflow.

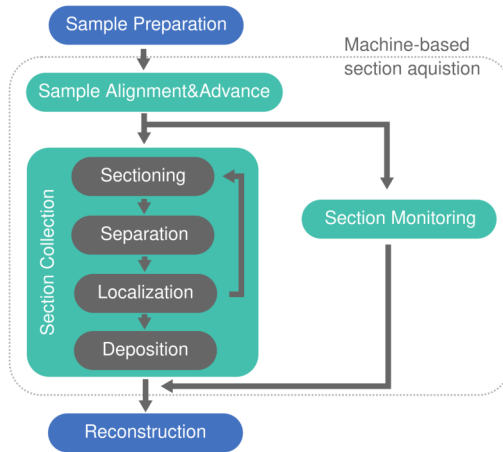


Figure 4.1: Machine-based section acquisition process.

The novel machine-based sample alignment and advance is described in the first Section 4.1.1, with the key element being the challenging and unique integration of a closed loop advance mechanism. The machine-based sample advance eliminates a potential point of failure by incorrect operation, which might cause permanent

damage to the sectioning knife and requires well trained operators to be performed safely.

The distinguishing feature of the system is the novel method for the machine-based section collection presented in Section 4.1.2. The method utilizes a structured water surface, which acts as the transportation medium during the float-off process after sectioning. Compared to other section collection methods a deposition pattern is integrated by surface functionalization onto the carrier substrate. In combination with a computer controllable four-axis substrate manipulator a fully automated section collection is accomplished. The manipulator is a custom design to avoid transmission of environmental vibrations into the system and does itself not generate vibrations during the sensitive sectioning process. The functional integration of a deposition pattern on the carrier substrate by surface functionalization is a unique property of the developed acquisition method and the first to allow the machine-based collection of large numbers (>1000) of serial sections on solid carrier substrates. An unprecedented package density is achieved with more than 400 section deposited on the size of 22 mm × 22 mm carrier substrates. The choice of possible carrier substrates and the deposition pattern increase the image modalities.

Section 4.1.3 covers the task of section monitoring, for which the illumination of the instrument is improved and a computer program for the section thickness estimation implemented. The developed algorithm calculates a quantitative measure of the relative section thickness. The resulting thickness is displayed as a two dimensional thickness map calculated from a captured image.

A fully integrated system for the machine-based acquisition of large numbers of sections, as displayed in Figure 4.2, has been implemented based on methods presented in Chapter 3. Parts of the system hardware have been improved, such as the top light to create a better visibility of the sections. A modified boat with black anodized background is used to improve the visibility of the sections and to provide more leeway for the substrate position.



Figure 4.2: Integrated system for the machine-based acquisition of serial sections. The edge lit top light is visible overhanging above. The custom black anodized ultra wide knife is mounted on the ultramicrotome. The automated four-axis substrate manipulator is engaged in the knife trough.

For automated section acquisition, the system is designed to reduce the overall influence of the operator on the process. This is accomplished by allowing a motorized and partly automated remote control of the instrument. The remote control reduces the contact of the operator to the instrument and thus the risk of transferring vibrations to the instrument. As vibrations manifest as chatter in the section thickness, as described in 2.1.4, the sectioning quality of the system is improved. Further, as outlined in 2.1.5, the collection of large numbers of serial ultramicrotome sections is a very demanding task even for skilled operators. The operators must be mentally focused on the process monitoring through the stereo microscope and the muscles need to remain tensed for the precise and low tremor manual manipulation of the delicate sub-millimeter sized sections. This demanding working conditions last for extended periods of the overall process

time. Due to the developed remote operation and machine-based collection, the stress on the operator is lower and the overall process time reduced.

The processes control is realized on a Raspberry Pi based controller platform using existing open source software and also novel developed libraries. An overview schema of the software architecture is shown in Appendix A.4. The platform consists of a Raspberry Pi 4 Model B and a custom designed PCB which interfaces six low vibration stepper motor drivers. The controller platform controls the ultramicrotome via a serial USB interface, captures camera frames, controls the illumination and drives the synchronous movement of four stepper motors, with two spare drivers for further automation tasks.

The performance of the developed methods and the resulting integrated system are demonstrated on the example of two case studies from material science and life science in Section 4.2. The system is able to collect more sections, in higher package density, in less time and with a lower section loss rate than conventional Array Tomography section acquisition.

4.1.1 Machine-based Sample Advance

The instrument setup prior to sectioning is a challenging part of the Array Tomography workflow, which requires experienced operators as possible mistakes can cause costly damage to the instrument, cutting tools and samples. The in Section 3.1 presented machine-based advance is the first closed loop sample advance of an ultramicrotome and a step towards the solution of the "half a century old restart issue" [27] which arises from thermal drift and relaxations in the instrument. The machine-based sample advance assists the operator, reduces the required skill level and is a safe procedure for the instrument setup.

A sample advance requires a challenging measurement between two planes – on the one hand the virtual cutting plane of the diamond knife and on the other hand the sample block face. The integration of measurement devices is difficult because none of the two planes can integrate any device directly. The integration of an indirect measurement device, offset from the two planes, is possible, but still error prone due to mounting tolerances and thermal drift [25]. The measurement includes the distance between the sample block face and the knife edge, as well as the correct orientation of the two planes.

The machine-based advance relies on pre-conditions to reduce the complexity of the alignment problem. With the trimming procedure described in Appendix A.1 the correct alignment of the sample block face is enforced along two axes – The rotation of the sample block about the arm axis and the rotation of the sample block about the axis of the knife edge. Initially the block face is positioned 100 μm to 150 μm away from the knife edge by moving the knife stage forward. This course advance is done manually by the operator, but can also be achieved by mechanical end stops with low mechanical tolerance. For example the switching from a trimming knife to the sectioning knife with a built-in offset can ensure the initial distance.

The reflection of the back light, which is also used in the manually performed sample advance, is used to measure the sample misalignment and distance. Thus the machine-based sample advance requires the presence of a reliable reflection

of the back light on the block face. An analysis of the system revealed further potential to improve the optical properties. For the sectioning knives used (ultra knives, Diatome), the clearance angle is indicated with 10° .¹ According to Equation 3.1 an optimal optics angle is twice the clearance angle. Thus an optics angle of 20° is required which can not be set on the ultramicrotome used (Powertome, RMC). The ultramicrotome is modified with an wedge installed into the turret to achieve the optimal optics angle. This change does not only improve the optical properties for the machine-based sample advance, but also improves the visibility of the back light reflection in a conventional sample advance. Especially it improves the visual observation of diffraction colors.

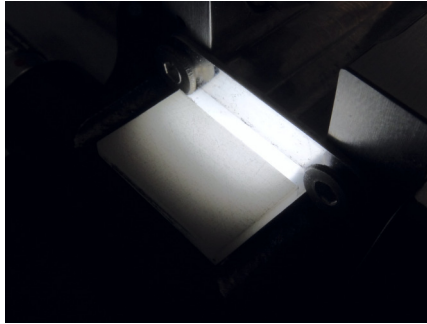


Figure 4.3: Image of the back light diffuser. The two different lighting zones with different material thickness are visible on the back.

The machine-based feature detection of the reflection band benefits from a uniform illumination. A diffuser plate, as displayed in Figure 4.3, is mounted on the back light to provide this uniformity. The diffuser consists of two different lighting zones. The bright zone is 3 mm wide and close to the knife. Light from this zone causes the observable reflection on the block face. The wider and dimmer zone provides a bright background in front of which the knife edge is clearly visible. This setup with a defined illumination does not only improve the machine-based

¹ Diatome ultra knives have an inbuilt clearance angle of 4° and are installed with an additional 6° , Diatome ultra jumbo knives have already 10° clearance angle inbuilt

feature detection but also the visual perception of the back light reflection by the operator.

The machine-based sample advance is integrated in a setup wizard which guides the user through the steps of the system setup. A screenshot of the wizard's user interface is displayed in Figure 4.4. The wizard reduces the risk that steps in the setup are skipped or performed in the wrong order. During the wizard, the correct setting of the cutting window and the correction of a knife rotation to the cutting plane are performed in a guided process. Some steps in the wizard bear further automation potential as described as an outlook in Section 4.4.

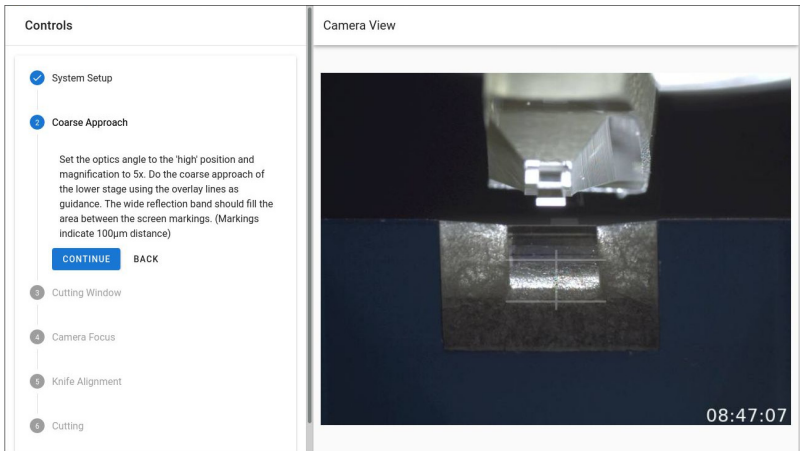


Figure 4.4: Screenshot of the web-based user interface for machine-based sample advance and alignment. The left part of the interface contains a six step wizard to guide the operator through the instrument setup. The camera image on the right is used to perform the coarse advance of the knife edge. The overlay cross-hair indicates the initial distance of $100\ \mu\text{m}$ between sample block face and knife edge

The plane of the sample block face and the cutting plane need to be parallel before the machine-based sample advance can start. This is accomplished by adjusting the remaining axis of the knife rotation. The machine-based sample alignment is able to measure the angular error, but because the knife rotation is

not motorized, the operator needs to manually adjust the rotation based on the indicated value. This measurement is performed in real time and the adjustments of the knife rotation can be performed from a safe distance between sample and knife edge. In contrast, the sample has to approach the knife edge multiple times in the conventional manual alignment procedure because the misalignment can only be observed when the knife edge is in proximity to the sample. This repeated approach is necessary because a rotation of the knife also causes a change of the knife position due to the offset pivot point of the stage. The machine-based advance saves time of the operator because the knife alignment can be performed in a single step from a safe distance between knife and sample. The angular error is measured with a resolution of 0.01° sufficiently precise to achieve a completely cut section with the first cut from a $500\ \mu\text{m}$ wide block for $100\ \text{nm}$ thick sections. When the knife edge is oriented to the sample block face, the machine performs the rest of the sample advance autonomously and starts the sectioning. An overview of the observed performance values for measurements of sample advance and angular error is given in Table 4.1.

Figure 4.5 displays the measurements of the sample distance over a period of 5 h for 122 repetitions. The ultramicrotome is powered on 2 h before the experiment is started and at thermal equilibrium. The required advance is known to be exactly $101\ \mu\text{m}$ at the start of the experiment. It is clearly visible that after a delay of 15 min, the estimated distance shows a steady increase of about $100\ \text{nm}$ per estimation run, respectively $42\ \text{nm}$ per minute. The increase of the sample distance declines over the period of 5 h slowly to $20\ \text{nm}$ per estimation run, respectively $8.5\ \text{nm}$ per minute. After 5 h the sectioning was started to verify the estimated sample contact distance.

The displayed evolution of the sample distance is typical for a system that undergoes thermal expansion. The image acquisition requires an arm movement which is powered by an electric motor. It is plausible that the waste heat of the motor requires 15 min to heat up the frame of the arm support. The caused thermal expansion then increases the sample distance. The expansion decreases over time until a new steady state is reached at thermal equilibrium. The experiment is also an assessment of thickness variations caused by thermal expansion, as the

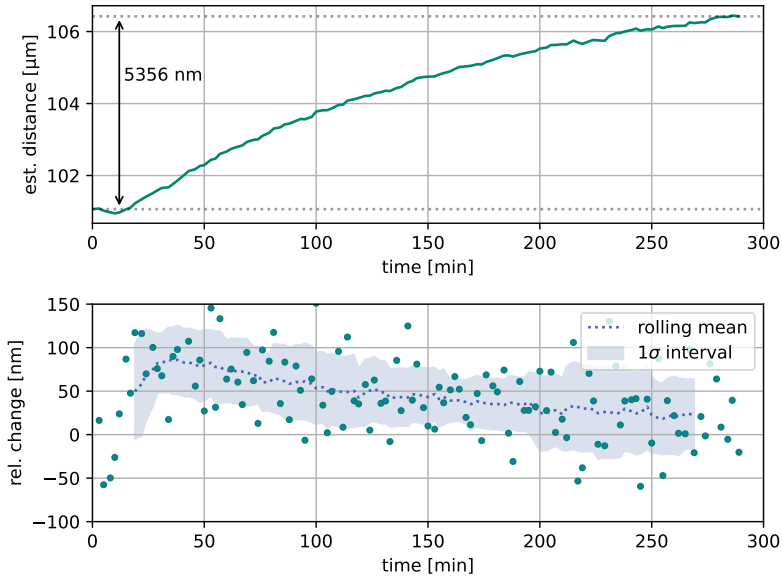


Figure 4.5: Repetitive calculation of the contact point in 122 successive measurement runs. Initially the knife edge is positioned 101 μm away from the sample. The ambient temperature is nearly constant at 21°. The top image shows the estimated distance over a period of 5 h. The lower graph displays the relative change between two following estimates as a scatter plot. The rolling mean of 16 values is displayed as a dotted line. The deviations follow a normal distribution with a probability of 0.92 for the hypothesis test (Pearson's two-sided chi squared probability)[94]. The blue colored area represents the 1σ -interval of the estimates. A measurement run requires 140 s.

sectioning also requires an arm movement which generates waste heat. Over a period of 5 h, the thermal expansion caused by the operation of the ultramicrotome reduces the sample advance by 5356 nm. This variations are also visible in the section thickness over the period of the ultramicrotome operation. Sections at the beginning of the operation are thinner than sections obtained after a long operation of the ultramicrotome. If the operation is interrupted for a longer period, the thermal contraction acts in the opposite direction. For example an interruption of 5 min with a comparable thermal contraction of 42 nm per minute causes 210 nm of additional sample advance. If the sectioning is continued, the additional feed

is above the maximum section thickness of 200 nm of ultramicrotome knives and causes excessive wear or damage. This is known as the restart issue and requires the attention of the operator [7, 27]. Interruptions of the sectioning process occur for example during the section collection. The machine-based sample advance allows a safe restart of the sectioning after extended interruptions.

To assess the performance of the machine-based advance in terms of the achievable resolution, the second graph in Figure 4.5 shows a rolling statistical analysis of 16 successive measurements to reduce the influence of the thermal expansion on the assessment. The std. deviation of the measurements stays in the range of 50 nm to 80 nm. The deviations follow a normal distribution with a probability of 0.92 for the hypothesis test (Pearson's two-sided chi squared probability) [94].² The system performs the final sample advance with a safety margin of five times the observed standard deviation. This corresponds to a total distance of 250 nm to 400 nm. The distance is comparable to the final distance of less than 1 μm that an experienced operator can achieve by observing the diffraction colors. The 5σ confidence interval ensures that the set section thickness is not exceeded with an error probability of only 2.8×10^{-7} . The measured std. deviation is low enough to ensure a safe and quick restart of sectioning after an interruption. It is however not low enough to allow a restart with the first section equal to the desired section thickness. This would require a std. deviation of less than approximately 10 nm. Through further improvements as described in Section 4.4 the machine-based advance can potentially meet this requirement too. An overview of the performance values for the sample advance is provided in Table 4.1.

As the knife edge is a delicate part that is easily damaged by an excessive sample advance, the algorithm ensures that no damage occurs. A common mistake that also effects the manual visual sample advance arises when the operator observes the wrong reflection on the block face and advances the sample too far. The algorithm continuously verifies that the observed reflection matches the derived internal model. If the model deviation of the sample points exceeds 250 nm, the

² The test is performed using Scipy's "normaltest" function [75]

machine-based advance is interrupted. Repeated tests similar to the one presented in Figure 4.5 show that the limits of the safe operation were not exceeded for different block materials and knives.

Table 4.1: Performance values for the machine-based sample alignment

	sample advance	angular error
Measurement range	75 μm to 150 μm	$\pm 5^\circ$
Resolution	80 nm	$<0.01^\circ$
Abs. accuracy	<500 nm	$<0.03^\circ$
Acquisition time	140 s	125 ms

4.1.2 Machine-based Serial Section Collection

The automated serial section collection is accomplished by the use of surface structured deposition patterns and a computer controlled substrate handling unit. The deposition pattern is created by surface functionalization and forms water channels that collect and guide the serial sections after they are cut. Sensitive ultramicrotome sections with nanometer thickness are immobilized by solid/fluid/solid interface driven interactions on the carrier substrate. The water channels form when the substrate is immersed in the water trough and are, according to Equation 3.21, approx. 121 μm high. The miniaturization of the channels does not only increase the achievable density of deposited sections but also changes physical properties. The fluidic system has a low Reynolds number of $<2 \times 10^{-4}$, as shown in Section 3.2.2, due to the small dimensions of the water channels. In this microfluidic system the viscous force between the interfaces of the sections and the substrate is dominant over the inertial force. The fluid in the channel acts more rigidly than for freely floating sections, which causes the sections and substrate to move in unison. This allows the sections to stay in position when the carrier substrate is moved laterally to create space for following sections to be collected. The collection process forms a cycle of sectioning, separation, pushing and shifting as shown in Figure 4.6. A scientific novelty is the functional integration of the section collection by chemical surface functionalization into the carrier substrate as described in Section 3.2.4.

The sectioning is an automated process performed by the ultramicrotome. The most difficult part for the operator is to remain still in front of the instrument, in such a way that air streams, vibrations or heat transfer from the operator do not influence the sectioning. These adverse influences are reduced by the machine-based section collection which allows remote operation and only requires manual intervention to resolve issues. The sectioning process itself is identical to the standard procedure. For example water level control, cutting speed and clearance angle are identical to the conventional section acquisition process. The risk of decalcification of section material is reduced as the section is only in contact to a small volume of water ($<20 \mu\text{L}$) inside the channel.

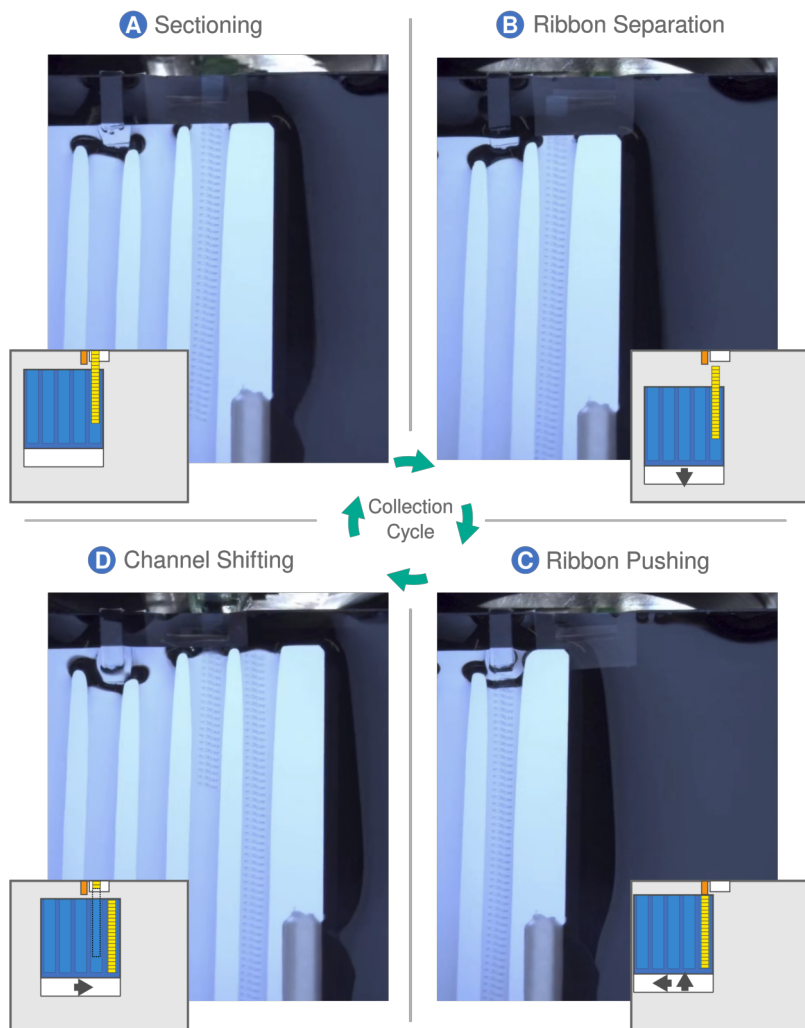


Figure 4.6: Key steps of the machine-based section collection cycle observed from a top view of the knife trough. The diamond knife is visible in the top of the images and a functionalized silicon substrate with seven channels positioned adjacent A) A Section ribbon is created and pushed into a water channel formed on the carrier substrate. B) The ribbon is separated by empty cuts. C) The ribbon is pushed completely inside the channel with an offset protrusion. D) The substrate is shifted to collect a next ribbon in an empty channel. A video of the collection cycle is included in the electronic appendix.

The machine-based section collection does not require manual operation of the ultramicrotome by the operator. Therefore human tremor does not negatively influence the process quality. The user interface is web based to allow remote operation and monitoring of the process. A hand controller allows the precise positioning of the substrate during the setup phase. The sectioning, section separation and deposition processes are completely automated.

The pushing force of the sectioning process is sufficient to move sections into the channel as the sections slide along the channel edges on a thin water film. It is possible to fill a 20 mm long channel, as seen in Figure 4.6A, over its complete length without sections starting to fold due to interaction with the channel boundary. The sliding of sections inside the channels requires that the channel boundary does not contain imperfections as these obstruct section movement. A vibrational motion of the substrate during the arm retract is used to re-mobilize sections that stick to the channel boundary. Other methods that collect section ribbons rely on the straightness of the section ribbon to define the position accuracy of the deposition result (compare to Section 2.2.2). In the here presented method, the section ribbons follow the path that is defined by the pre-structured deposition pattern. The sections can thus be positioned in a more dense packing. Also no lateral position manipulation is required as the channels define the position.

The sections are separated by two arm strokes with zero advance. Due to the thermal expansion of the instrument (compare to Figure 4.5) during the operation, it is beneficial to advance by a small amount to compensate for the expansion. In experiments an advance of 8 nm shows good results in lowering the adhesion to the knife edge sufficiently for a complete section detachment. This small advance does not cause a new section to form on the knife edge. The adhesion to the knife edge causes an immobilization of the sections. The immobilization is lost after the detachment. In the presented method the sections are further immobilized in the channels after they are separated. This prevents freely floating and difficult to control sections. Since only a thin water film wets the channels, the drag on the section ribbon caused by moving the substrate back, is sufficient to separate the ribbon from the knife edge. A separated section ribbon is shown in Figure 4.6B. The implemented section separation method allows the complete collection of the

sectioned volume, as no sections remain on the knife or are lost in the process. This also implies that sections do not need to be manually cleared from the trough or the diamond knife after sectioning. The sectioning can also be interrupted and continued the next day. The machine-based sample advance can ensure safe continuation.

After the section ribbon is separated from the knife edge, the ribbon needs to be placed completely above the carrier substrate. An protrusion placed left of the diamond knife is used to push the section ribbon inside the channel, as shown in Figure 4.6C. The offset protrusion made of FEP foil with a low surface-free-energy prevents sections from adhering and does not impair the sectioning process.

The immobilization of the section ribbon inside the microfluidic channel allows the substrate to be moved to the next collection position without a further position change of the section ribbon relative to the substrate. Further the sections are effectively shielded from turbulence inside the water reservoir of the knife boat e.g. caused by a lateral movement of the substrate. That way a switching to the next empty channel is possible without the requirement to pin the sections in already filled channels. Compared to manipulation methods that require a physical contact, the risk of section damage is reduced. Also sections do not have to be deposited after each ribbon. In previous methodologies the sections are immobilized by either a partial or a complete attachment of the sections to the carrier substrate (compare to Section 2.3.2). This immobilization interrupts the sectioning process and meanwhile the instrument may undergo a thermal drift. The resulting thermal expansion changes the feed of the instrument and thus affects the consistency of the section thickness during interruptions. In contrast, the presented process greatly reduces the time before the next ribbon can be sectioned. Thus, the thermal instability of the instrument has less effect before the next section is cut.

Retrieval of the completed, section-filled substrate is done by slowly lifting the substrate from the knife trough using the integrated four-axis substrate handling system. For a wrinkle-free deposition of sections, the carrier substrate must be hydrophilic to allow a retraction of the water meniscus with shallow angle.

Plasma treatment of the carrier substrates with air (oxygen) plasma is an established method in Array Tomography for the creation of hydrophilic substrates as described in Section 2.3.2. The hydrophilic properties of the channels on the functionalized carrier substrates after the plasma induced structuring thus allow deposition of sections without wrinkles. After the substrate is lifted out of the knife trough, the remaining water film evaporates and the sections settle on the substrate surface.

The resulting pattern of the deposited sections follows a straight alignment and preserves the section order by storing them in separated, pre-selected rows. That way the order and orientation of sections is easily traceable which is a requirement for Array Tomography. It is beneficial if the section locations follow a defined pattern, as this makes the later localization during the imaging process easier. The ribbons are precisely aligned in a predefined pattern. This defined section pattern simplifies the localisation of individual sections during the subsequent imaging and enables automated section detection. The seven channels allow the collection of seven ribbons which is more than approximately five ribbons that a skilled operator can collect on a single carrier substrate in the conventional Array Tomography workflow. The deposition has been demonstrated for silicon wafer pieces and glass cover slips in the form factor of 22 mm × 22 mm.

The presented section collection process does not require manual section manipulation by the operator and thus reduces the risk of section loss by handling errors. A lossless section collection is a requirement for an artefact free reconstruction of the sample volume [28]. By the novel acquisition method, a reliable method with low section loss that enables the analysis of large sample volumes in Array Tomography is presented.

4.1.3 Machine-based Section Monitoring

The novel machine-based section monitoring is the first inline capable quantitative section thickness estimation algorithm for ultramicrotome sections. The in Section 3.1 introduced model is based on physical properties of the light interference at thin films.

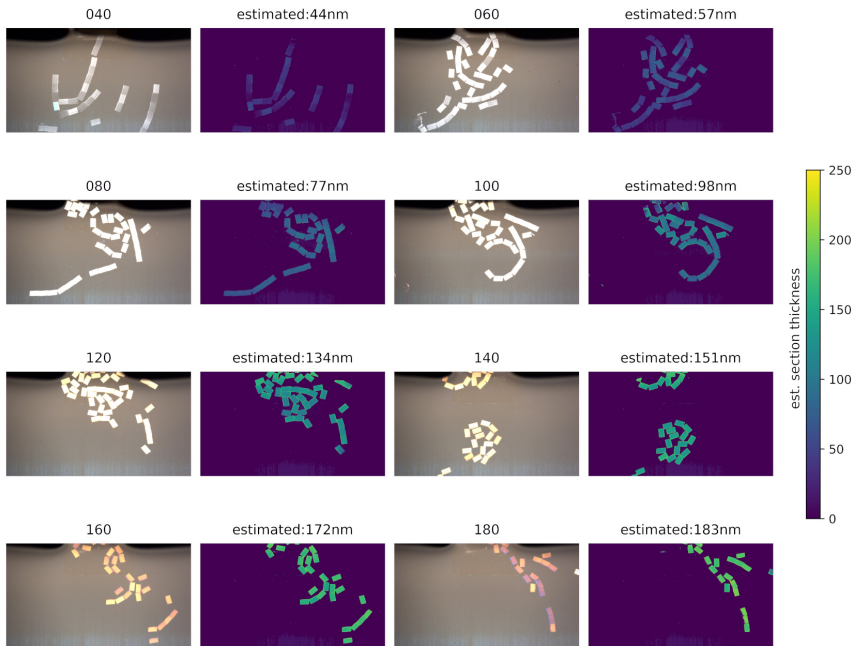


Figure 4.7: A panel of captured camera images (left) for 40 nm to 180 nm thick sections of empty epoxide blocks and the corresponding false color mappings (right) of the thickness estimation algorithm. The indicated section thickness is the set nominal value. In the lower part of each image the negative influence of light scattered from the background of the blue knife trough can be observed.

Figure 4.7 shows the performance of the thickness estimation algorithm for ultramicrotome sections floating on the water surface of the knife trough with different

thickness. The interference color model is obtained from a set of sections with increasing section thickness in the range from 40 nm to 200 nm. The absolute values of the section thickness are obtained by a global scaling of the parameterisation to correspond to the nominal thickness on average. The estimation algorithm assigns a thickness of zero to the water surface as the limit of the color model for a thickness of zero is equal to the color of the sole reflection of the top light on the water surface. This opens up the possibility to perform a machine-based section detection based on the thickness estimation as described in Section 4.4. The section shapes correspond to the visually perceived shapes which indicates that the sections are correctly identified. The maximal deviation of the estimated section thickness is observed for 120 nm thick sections with a difference of 14 nm and corresponds to a deviation of 11.6 %. This deviation can also be caused by relaxation processes in the sample material and needs to be verified by a subsequent thickness measurement of deposited sections. The meniscus of the water surface causes a vanishing of the reflection on the top of the image. This change in the reflection hides sections from the algorithmic as well as the visual perception of the sections (see 120 nm sections in Figure 4.7), but does not cause artefacts in the section thickness estimation. Artefacts can be observed in the lower part of the image and arise from light scattering in the blue knife trough. The light scattering can likely be reduced by a change of the trough color. A black anodized knife trough has less light scattering that contributes to the background image. Despite these small artefacts the estimation algorithm reliably associates only a section thickness to areas that are truly section material and is not disturbed by background objects like the diamond knife's encapsulation material.

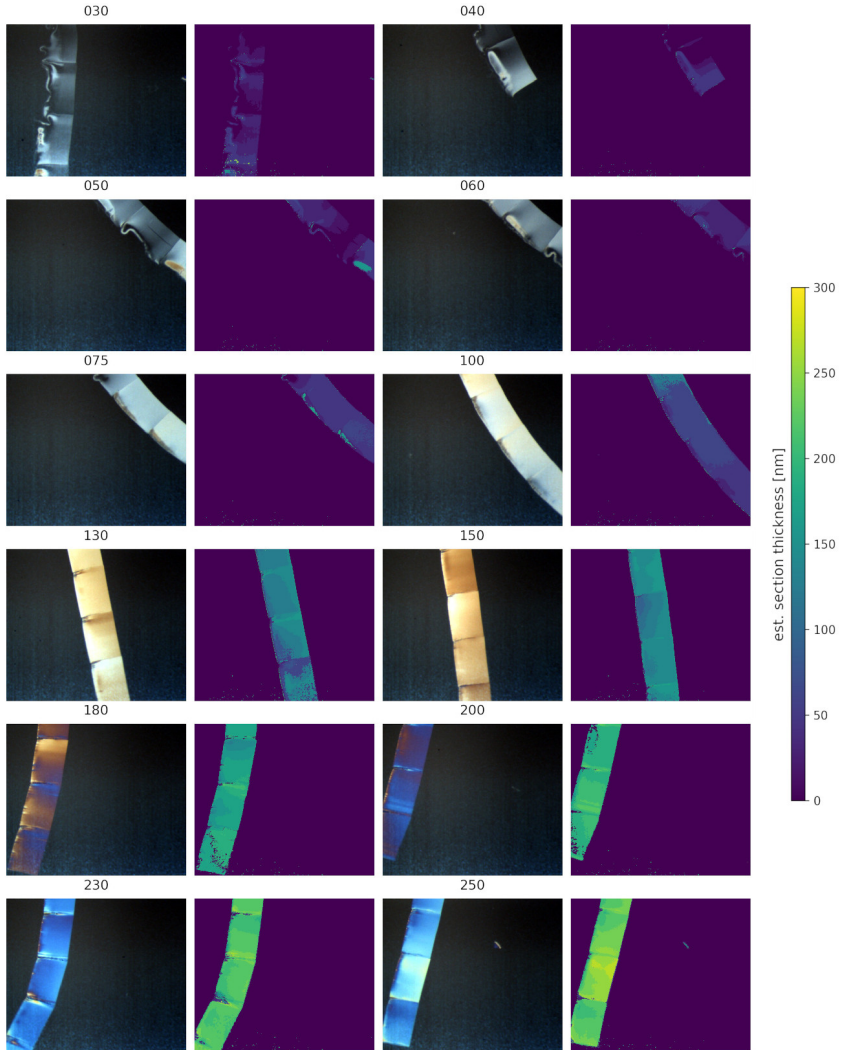


Figure 4.8: Ultra-thin sections obtained from a sample of PET embedded in Epofix. Thickness variations within sections arise from variations in the material properties, thermal expansion, block relaxation, elasticity and backlash. For thin sections (<75 nm) delamination can be observed as only every second section contains a piece of PET. This is due to the different material properties of PET and Epofix.

The estimation algorithm provides a quantitative means for the inline monitoring of the sectioning process. Chatter for example can be early detected and quantified. A closeup view of sections is shown in Figure 4.8. The human perception of color changes is not uniform and for some thickness ranges, the deviation in the thickness provides a more obvious change in the hue than for other thickness ranges (see Figure 3.12). The process monitoring can possibly also be performed by the machine in a fully automated system to alert the operator if the thickness deviations exceed a threshold. Another possible application is a closed loop feedback control of the section thickness. The sample advance of conventional ultramicrotomes is not directly measured and subject to sample block relaxation and thermal expansion as described in Section 2.3.1.

The methodology can also be used to estimate the thickness of deposited sections without necessary prior calibration (compare to Section 2.3.3). The relative thickness estimation can then be used to improve three dimensional reconstruction in Array Tomography. A correction of thickness variations preserves the proportions and prevents dilatation effects. Absolute thickness values can also be derived from reference structures. Such structures are common in biological samples, for example the regular spacing of muscle filament is commonly used to re scale images [69]. This method is also better if the used staining and embedding methods cause a shrinkage compared to the volume the cell had "in vivo".

If absolute thickness information is required, a calibration of the estimation algorithm must be performed. This can be achieved by the subsequent measurement of the section thickness. Ellipsometry, white light interferometry or Atomic Force Microscopy are established tools to provide the required calibration information. In principle only a single measurement of a single section thickness is required to calibrate the complete estimation range of the algorithm.

For the implementation, the ultramicrotome is improved to provide a better illumination for the observation of the interference colors. Also the human based section monitoring profits from these changes:

- The presented top light produces a uniform reflection on the water surface with less light scattered in the knife trough (see Figure 3.13).
- The spectrum is slightly optimized compared to conventional LED top lights to provide contrast richer interference colors (see Figure 3.11).
- Compared to a fluorescence bulb the top light radiates less heat that negatively influences the sectioning process.

4.2 Section Deposition Results – Case Studies

The machine-based section acquisition is validated on two different sample types from material science and life sciences. The first sample type is a carbonized cellulose origami structure, the second sample type is a mouse brain organoid. From the origami sample two blocks are prepared with modified block geometries. The sample blocks are trimmed by the procedure described in Appendix A.1 with an adhesive coating to improve ribbon formation. The samples are placed centered in the trimmed block face to avoid curved ribbons caused by a different compression between sample and embedding material. Sections of the sample are obtained with a cutting speed of $1 \frac{\text{mm}}{\text{s}}$. The channel width on the carrier substrates is 1.2 mm with seven channels structured on 22 mm wide square carrier substrates of glass and silicon wafer as described in Section 3.2.4.

In the case studies the machine-based section acquisition is capable to acquire 400 sections per hour. Even for an experienced operator it is challenging to manually acquire this number of sections per hour. The fact that ribbons do not need to be attached to the substrate, but are temporally immobilized in the channels, saves a significant amount of process time. In comparison, the section acquisition time is much faster than the time that is required for imaging. The LM used (Axio Imager) with 720 nm resolution requires one working day of imaging time for

1045 sections of the origami sample. An EM requires a significant amount of time more depending on the ROI and imaging parameters. Because the sections are collected on individual carrier substrates, it is possible that multiple machines can image simultaneously.

The sectioning cycle is only shortly interrupted for 30 s to 45 s to push the ribbons inside the channel. The sections show thickness variations at the beginning of the ribbon, which are likely caused by thermal expansion during the interruption. The thickness variations are visible in Figure 4.9B as a variation of the section color. In Section 4.1.1 it is shown that the instrument requires more than 5 h before a thermal equilibrium is reached. On the basis of the observed thermal expansion of 42 nm per minute this equals an additional feed of 21 nm to 32 nm during the interruptions.

For the application of the developed machine-based section acquisition, the scope of the processable volume is interesting. The volume is defined by the depth of the trimmed block and by the area of the block face. The highest currently achievable depth of acquired sample volume is approx. 210 μm . The depth is not limited by the machine-based acquisition, but by the preparation of the sample. With current trimming knives the block can only be trimmed approx. 250 μm deep before the trimmed sides show a noticeable degeneration of the quality. A poor quality of the lateral block faces impairs the sectioning process. For the acquisition of serial sections the blocks are trimmed 250 μm deep as a reliable sectioning process is desired. A safety margin is added to prevent the damage of the sectioning knife in case that excessive material is cut below the trimmed depth.

Surface structured channels can show a limited stability which results in a drying of the channels [98]. The here used channels have a widening opening to increase the stability. A drying of channels has not been observed in the 30 min long collection period for an ambient humidity between 40 % to 55 %. The modified channel opening improves the channel stability sufficiently to allow the complete filling of the substrate with sections.

So far, four machine-based section acquisitions with real samples were performed to assess the section collection performance. An overview of the results is given in Table 4.2. The results of each experiment are discussed below.

The carbonized origami sample is a large and porous structure. The sample is embedded in Spurr firm epoxide, which shows good infiltration properties because of the low viscosity. The first material sample is trimmed to a block face height of 440 μm and width of 885 μm . The sample spans across the width of the sample block due to the large dimensions. The block face height allows a collection of ribbons with 45 sections inside the 20 mm long channels on the carrier substrates. The sections are obtained with a nominal thickness of 200 nm. A total of 14 ribbons is collected on two carrier substrates. The first seven ribbons are deposited on a glass substrate. The last seven ribbons are deposited on silicon wafer. The acquisition required manual intervention because of sections jamming the channel.

For a smooth gliding of the sections inside the channel, a tangential encounter of the sections to the channel boundary is desirable. This is not sufficiently enforced by 885 μm wide sections, which have enough space in 1200 μm wide channels to rotate. A steep encounter by the sections can penetrate the channel boundary and causes sections to stick on the dry substrate. Sticking sections prevent a further filling of the channels and require manual intervention. Sections that stick to the substrate can be manually re-mobilized with an eye lash tool.

To reduce the risk of sections clogging the channel, a second block of the origami structure is prepared with a block width of 1050 μm . The block height is decreased to 410 μm in order to place more sections in a ribbon of equal length. The 20 mm long channels collect 55 sections per ribbon. The block face is displayed in Figure 4.9A.

The number of sections per channel is higher than expected from the block face height of 410 μm . The discrepancy is explained by the section compression. Section compression causes the cut sections to have a smaller height than the block face. The 20 mm long channels can thus accommodate 55 sections instead of the nominal 48 sections. The discrepancy corresponds to a section compression

of 15%. Section compression can reach values up to 25% [7]. While the compression is beneficial in regards of the number of sections per channel, the distortion of the shape impairs the reconstruction. Means to remove the section compression such as the treatment with chloroform or heat are known [7]. Because the sections are collected on a water film these methods can also be potentially applied to the machine-based section collection.

The organoid sample was reused and not embedded specifically for the experiment. The embedding of the organoid showed some degradation possibly due to aging. The embedding material of the organoid was soft and sticky which caused occasional section loss due to section pullback during sectioning. To improve the stability of the sectioning process, the organoid was carefully trimmed and re-embedded in Spurr firm epoxide. Also with the re-embedding the sectioning quality was poor for this sample. A machine-based acquisition of serial sections was still attempted. The section pullback made the collection of serial sections difficult, as it separates the ribbon and fragments of the ribbon require manual manipulation. The eye lash tool can be used to push ribbon fragments into the collecting channels. The section pullback occurred for both 100 nm and 200 nm thick sections. While it is possible to use the machine-based section acquisition with samples that are difficult to section, it is advisable to ensure that the sample sections nicely as it greatly reduces the manual work.

Three wafers filled with serial sections of the origami structure have been imaged in a Zeiss Axio Imager.³ An ROI of $662\ \mu\text{m} \times 464\ \mu\text{m}$ at 720 nm resolution was imaged in 1044 sections. The CAT software is used to automate the image acquisition for Array Tomography. The software has been able to detect most of the sections because of the defined arrangement on the substrate and section shape. The chamfers, that are added to the block face during the block trimming to assist the sliding process in the channels, are features which uniquely define the orientation and are independent of the embedded sample. These features are beneficial in the automated section detection and increase the chance of a correct

³ The imaging and registration was performed at Heidelberg University, Centre for Advanced Materials (CAM), with kind assistance by Prof. Dr. Rasmus Schröder and Dr. Irene Wacker

identification by the imaging program. Based on the section detection the ROI in each section is copied automatically into the detected section shape. For some sections a manual correction of the detected ROI was necessary.

The image stack is registered and aligned using the Fiji image processing package [95]. The registered images are segmented in 3D Slicer using threshold and then watershed segmentation. The segmented volume is exported as an STL and rendered in Blender to produce a three-dimensional representation of the sample. A video showing a virtual flight through the sample is included in the electronic appendix. A picture of the rendering is shown in Figure 4.9C.

Table 4.2: Characteristics of acquired sections for 4 samples. A carbonized cellulose origami structure and a model organoid of a mouse brain.

	Origami 1	Origami 2	Organoid 1	Organoid 2
width	900 μm	1050 μm	1060 μm	1060 μm
height	440 μm	410 μm	400 μm	400 μm
thickness	200 nm	200 nm	100 nm	200 nm
ribbons	14	19	11	12
ribbon length	45	55	55	55
substrates	2	3	2	2
total sections	630	1045	605	660
sliced depth	120 μm	209 μm	60.5 μm	132 μm
acquisition time	1.5 h	2.5 h	1.5 h	1.7 h

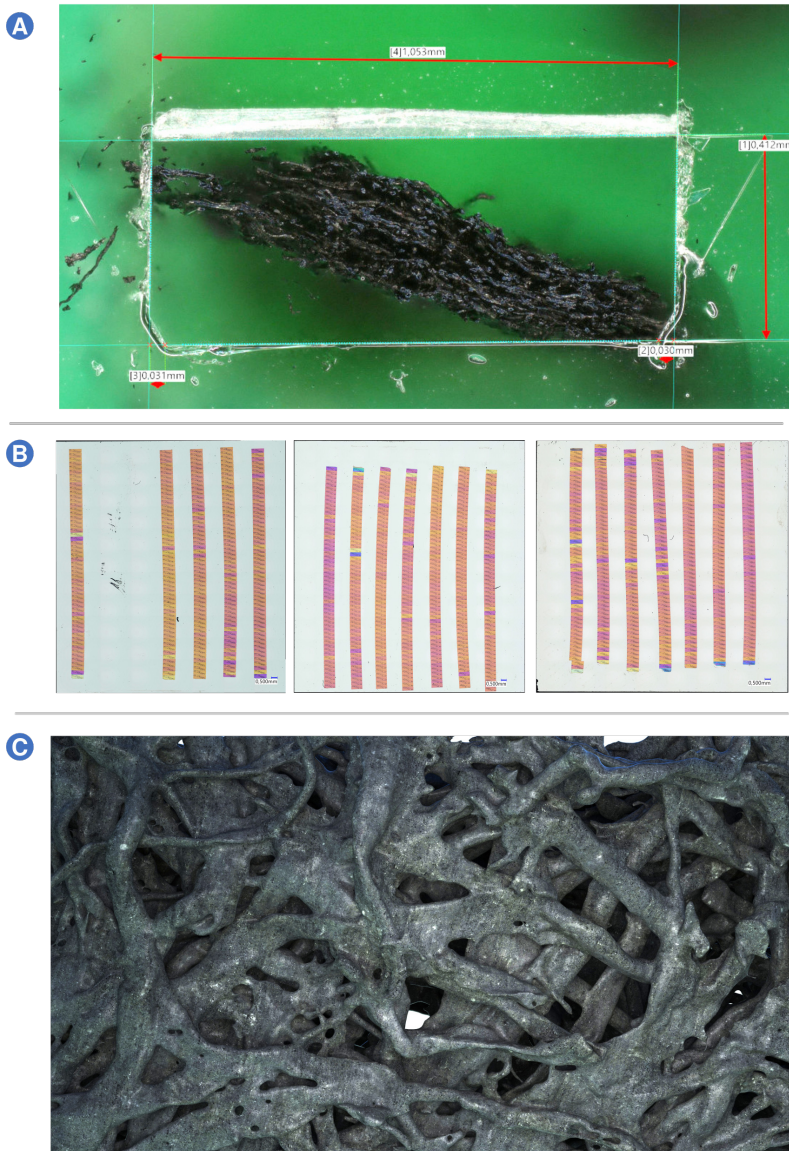


Figure 4.9: A) Topview of a block face with a carbonized origami structure embedded. B) 1045 sections obtained from the sample block and collected on three silicon wafers with each an area of 22 mm × 22 mm. C) Rendering of the reconstructed sample in Blender.

4.3 Conclusion

With the presented system a highly integrated solution for the machine-based acquisition of large numbers of sections for Array Tomography is achieved. At the same time, the characteristic versatility of the applicable imaging modalities of the conventional Array Tomography is preserved. This distinguishes the solution from other systems as described in Section 2.2. The deposition is demonstrated for solid substrates of glass and silicon and can potentially be extended to other substrates.

The system is able to collect more sections, in a higher package density, in less time and with a lower error rate compared to the conventional Array Tomography section acquisition. For the substrate positioning a motorized version of a substrate manipulator is implemented that can be considered as an evolution of existing third hand systems. The collection task is integrated onto the carrier substrate through surface functionalization.

Array Tomography offers great potential to enable new scientific insights in the ultrastructure of large volumes. This potential is now made accessible by a machine-based section acquisition. The efficient acquisition of large numbers of sample sections allows for bigger sample volumes and can provide new insights in scientific research. The developed solution is characterized by the following properties:

- The developed machine-based section acquisition is a **retrofitable extension** to existing ultramicrotomes.
- The acquisition can also be **performed by less trained personal** as the complexity of sample alignment and sample advance are significantly reduced and no skill for section manipulation is required.
- The **operator influence on the section quality is reduced** as the system can be remotely operated and does not require a presence of the operator in front of the instrument. Vibrations induced by the operator do thus not impair the cutting process.

- The **manual workload is reduced**, as the machine-based section collection is largely automated and does not require a section manipulation by the operator.
- The **risk of section loss is significantly reduced**, as no physical contact to the section is required to manipulate the section position for deposition.
- The **economical acquisition of large numbers of sections is improved**, as more than 1000 section can be acquired during a process time of 2.5 h.
- The **risk of damage to the system is significantly decreased**, as especially the diamond knives are well protected. The machine-based guided alignment and automated advance is highly reliable with a model based verification. Further no manual manipulation tasks in proximity to the knife edge are required.
- An **automated image acquisition** is possible, as the sections are collected in a way that is compatible with automated imaging procedures in conventional microscopes.
- The **versatility of the imaging modalities** compared to the conventional section acquisition in Array Tomography is preserved, as the deposition has been demonstrated on the most commonly used carrier substrates in Array Tomography. The carrier substrates have dimensions that are compatible with available microscopes and procedures.

4.4 Outlook

The system is designed as an extension to an existing ultramicrotome. This leaves room for improvements by further modifications to the ultramicrotome itself. This section provides a possible outlook separated into the tasks of machine-based **sample advance**, **section collection** and **section monitoring**.

In the current implementation of the machine-based **sample advance** the standard stereo microscope of the ultramicrotome is used. The optical system is thus not specifically designed for the machine-based measurement of the block distance. A

dedicated camera system can be used for the machine-based sample advance. The camera system can be mounted with fixed angle, position, focus and magnification. A tuning of back light wavelength, magnification and pixel size offers further improvement of the accuracy. With the currently achievable accuracy a safe start of the sectioning process is accomplished. A further improvement of the accuracy can allow a restart of sectioning with the first section equal to the desired section thickness. Although there are principle limitations because relaxation in the block causes bending of the block face which yield partial cuts also for a perfect advance of the sample. Some steps of the setup wizard can potentially be further automated. A motorized stage for example can correct the rotation of the knife automatically. The developed control platform has two more motor drivers available, that can be used to motorize the knife rotation.

In the machine-based **section collection** occasionally section ribbons stick to the channel boundary and require manual release to continue the machine-based section collection. The assistance by vibrational motion during the section collection can potentially be further improved, as vibrations with a higher frequency are likely to reduced the friction further and thus lower the chance of a section to clog the channel. A vibration motor or a piezo actuator can for example be installed in the substrate holder to generate vibrations with a higher frequency.

The time required to push the ribbons inside the channel has the potential to be further reduced as the thermal expansion during the interruption causes thickness variations in the sections. Also the thermal stability of the ultramicrotome can be improved by providing an external heat sink to the electrical motors or by using more efficient drives.

To date the maximum depth of sectionable volume is limited by the available trimming knives. Modified trimming knives can potentially prepare deeper blocks. An aspect ratio of block cross section to the trimmed depth may be a requirement in case of trimming depths below 250 μm to prevent bending of the sample block during the sectioning. In terms of the block face area, wider blocks than 1050 μm are possible by extending the channel width. Smaller channels are problematic because they decrease the cross section for a fluid inflow more than

the exposed surface and thus make the evaporation of the contained fluid more likely as described in Section 3.2.3. For too wide channels the control of the water height might be a problem. The height of the block face is a potential free parameter. Block faces with a more extreme aspect ratio than demonstrated are possible. Bigger block faces increase the occupied section area and thus less sections can be deposited on a single carrier substrate. Bigger substrates provide more deposition space to accommodate more sections.

The deposition is demonstrated for glass and silicon substrates. These substrates are suitable for the imaging in light and also scanning electron microscopes. It is likely that the same methodology to functionalize the carrier substrates is applicable to indium-tin-oxide (ITO) coated substrates. IN AT-TEM, the sections are collected on glass substrates that are coated with a support film [96, 97]. The sections are transferred to the TEM grids, by a float-off process of the support film and subsequent placing of TEM grids from the top on the desired regions of interest in the floating section ribbons. With a suitable functionalization of the support film also these substrates can be used in the presented machine-based section acquisition. The structuring is performed by applying a mask on a previously silanized carrier substrate. Laser cut foils with PDMS coating have been tested in first experiments successfully as an alternative to the applied masks. Pre-silanized carrier substrates could be made available as consumables to ease the structuring process further.

In the machine-based **section monitoring** the information content of the captured light can be further increased by a reduction of the background light. It is known that reflected light shows polarization. This effect can be used to further improve the signal to noise ratio by the utilization of a polarization filter.

As the sections are clearly differentiated from other background image objects, the estimation algorithm can be a powerful pre-processing step for a further machine based section detection. The algorithm can also provide a confidence value based on the distance of the color value to the color model. The training of neural networks to correctly identify sections in front of background structures is known to be challenging [24, 61].

The calibration needs to be performed for every sample with a different refractive index. It is possible that the instrument is pre-calibrated for certain embedding materials. The model is also depending on the angle of incidence of the reflected light rays. Conventional microtomes allow a free positioning of the stereo microscope used for monitoring. A fixed dedicated camera or reference marks to achieve reproducible conditions can benefit the estimation algorithm to allow for a precalibration. A differential image of the pure water surface can yield the non interfering part k_1 . The optic assembly is not fixed, thus a differential image is not obtained here to improve the resilience against background scattered light. In a new integration, the optic assembly can be fixed to produce more reliable conditions. A change of the water level will also change the reflection. In that case the differential image would not improve but rather disturb the thickness estimation.

List of Figures

1.1	Array Tomography process with a schematic depiction of the two characteristic steps. "Tomography" meaning a slicing of the sample and "Array" from the arrangement of the slices in an array on a carrier substrate used for imaging.	2
1.2	Picture taken through the microscope of an ultramicrotome. The picture shows freely floating sections in the water trough of an ultramicrotome knife. Blue interference colors occur for 200 nm and silverish/golden colors for 80 nm to 100 nm thick sections. The last section ribbon is still attached to the diamond knife. The sections have a width of approx. 800 μm	5
2.1	Side-view of an ultramicrotome with annotations of the main components. The arm motions are indicated with dashed blue lines.	17
2.2	Diffraction colors visible in the vicinity of the knife edge for a diminishing gap between block face and knife edge. The back light is reflected on the block face and passes through the gap between sample and knife edge. The knife edge is slightly misaligned to the sample block face and the decreasing gap creates a rainbow like color pattern. On the left side a blue hue is visible before the light vanishes completely. A gap is still present on the left side but too small to allow light to pass. The correct identification of these reflections can be difficult for operators.	20
2.3	A) Formation of section ribbon by successive attachment of new to previous sections. B) Section ribbon curvature caused by imperfect trimming or compression.	25

2.4 Operator performing the tasks to collect serial sections on a piece of silicon wafer from Spomer [41]. A) Knife with immersed substrate and handheld manipulation tool to collect a section ribbon. B) A ribbon is separated from the knife edge by a stroking motion. C) Dragging of a section ribbon. D) Pinning of the end of a section ribbon to immobilize it during the deposition. 27

2.5 A) Picture of third hand proposed by Spomer with seven degrees of freedom to control the substrate position [12, 43]. Sections are deposited on the substrate by a manually controlled lifting motion. B) Picture of the Advanced Substrate Holder (ASH) II sold by RMC Boeckeler Instruments [44]. The ASH II has only three degrees of freedom to position the substrate but is directly mounted on the knife stage. 29

2.6 Diatome ATS knife presented by Burel et al. [45, 46]. The carrier substrate is placed in the bottom of the knife boat. After the section ribbons are positioned above the substrate, the water is drained from the boat using a syringe or valve. 30

2.7 A) Panel of nine exemplary views through the stereo microscope of the ultramicrotome. Floating sections with varying thickness from 50 nm to 200 nm can be observed. The ultramicrotome knife used in the image is of an old type which produces a curved water surface, thereby making it specially difficult to observe the section in the reflection. Also ambient light scattered on the bottom surface of the boat superimposes with the reflected light on the water surface and makes it difficult to see the sections. The first two images of the panel show the irregular illumination of the light source used (chess board like structure). B) Typical interference color reference chart for ultramicrotome sections. 31

2.8 ATUMtome system to collect serial sections on a flexible tape [29]. The tape collection system is mounted on the front side of the antivibration table and reaches into the knife trough on the ultramicrotome (PT-XL). 33

-
- 2.9 A) Side view of the Leica ARTOS 3D [23]. Visible is the knife trough installed inside an acrylic environmental housing with an access to operate the draining valve for a controlled fluid outflow. The three pictures on the right side are extracted from a Leica video, showing the steps of collecting 150 serial sections contained in three ribbons observed through the stereo microscope [56]. B.) Three ribbons (gray : 60 nm) for later analysis sectioned from the right to the left are attached to the extra wide diamond knife. C.) Sacrificial sections (gold : 100 nm) push the sections for analysis (gray) above the carrier substrate. D.) The trough water is drained to settle the sections on the carrier substrate. 35
- 3.1 A) Back-light reflection light path. The gap between knife edge and block face allows only a portion of the light to reach the camera sensor. This is visible as a band of light that diminishes with decreasing distance between block and knife edge. B.) Diffraction limited illumination change. An interpolation based on the measurements of multiple pixels is used to estimate the position of the knife edge with sub-pixel accuracy. 49
- 3.2 A) Depiction of an illuminated band caused by the reflection of the back light on the block face. Misalignment of the knife edge, camera rotation and block distance are detectable as features of the illuminated band. B) Feature extraction process which detects the position and angle of the edge features with sub-pixel precision (1). The image is sliced and rearranged to compensate for a slope of the edges (2). A collapsed line profile is then edge filtered. The lobe width is determined by fitting an Gaussian model (3). The Gaussian model with the smallest lobe corresponds to the angle of the feature in the image. Through interpolation of the model parameters, the position and angle of the edges can be measured with an accuracy smaller than the pixel size (4). 52

3.3 Schematic of the key steps of the machine-based section collection process as viewed from the top looking at the knife trough. Exemplary a functionalized substrate with five rectangular channels is depicted. 57

3.4 Cross section (blue) in a straight part of a water channel formed on a structured substrate with a hydrophilic channel (center) and a hydrophobic enclosure (left and right). The channel width in y direction is defined by the width of the hydrophilic area w_c . The first principal radius of curvature of the water surface lies r_1 in the y-z plane. The second principal radius is equal to infinity as the cross section does not change in a straight part of the channel and therefore no curvature exists along the x axis. For a constant pressure the water film takes the shape of a circular segment and the Young-Laplace equation can be used to calculate the curvature radius. The height of the fluid film h_c is defined by the circular segment with r_1 and w_c 58

3.5 Plot of the dependency of the channel cross section curvature \tilde{k}_1 to the channel height \tilde{h}_c in a circular segment that models a fluid channel. The values are normalized to the channel width w_c . The grayed area shows the curvature that can be achieved by the immersion of 5 mm and proposes a technical limit for a 1.2 mm wide channel. The dashed line shows the series approximation of second order, which is visibly a good fit in the relevant region. . . . 63

3.6 Cross section along the length of a channel in the xz-plane with relevant depictions of cross-sections in the yz-plane for: A) channel opening B) straight part and C) channel ending. Exemplary values for the first and second principal curvature are added. The mean curvature is assumed to be one. The cross section with the lowest second principal curvature (red cross) imposes a local minimum, that is the origin of a channel contraction and finally causes a separation between channel and fluid reservoir. 66

3.7	Cross section along the length of optimized channel in the xy-plane with relevant depictions of cross-sections in the yz-plane for: A) channel opening B) straight part and C) channel ending. Exemplary values for the first and second principal curvature are added. The mean curvature is assumed to be one. The cross section changes steadily in the first half and avoids a semicircle-shape that causes contraction.	67
3.8	a) Plot of the expected evaporation time t_e over the channel width w_c for for different ambient temperatures $T = 10^\circ\text{C}$, 15°C , 20°C and 25°C . Other model parameters: $z = 53\text{ mm}$, $v_z = 2\frac{\text{cm}}{\text{s}}$, $h_i = 4.8\text{ mm}$. The source code of the plot is shown in Appendix A.3.	73
3.9	Process steps of vapor phase silanization, followed by structured plasma treatment to create patterns with different wettability.	75
3.10	A) Optical system used to capture the interference colors of the ultra-thin sections. B) Ray paths causing the optical path difference by a first partial reflection on the air/section interface and a second partial reflection at the interface section/water.	78
3.11	Spectrum of different top lights used for the section monitoring. The spectra are obtained from a custom top light built from an edge lit display illumination (Iphone 6), an ultramicrotome LED top light (Leica, UC7) and an ultramicrotome fluorescent bulb top light (RMC, Powerome). The edge lit display shows local maxima in the spectrum for blue, green and red perceived wavelengths and is comparable to the ultramicrotome LED top light. The spectrum of the fluorescent bulb shows the most distinct maxima in the spectrum.	83

3.12 The two color bars in the top show the simulated interference colors of epoxide sections for a top light source with a "cold" color temperature of 6000 K and a "warm" light source of 3000 K. The lower part displays the perceived color difference according to the CAM02 color perception model [93]. An ideal light source for human visual section thickness estimation would show a flat curve. The cold light source (blue) shows a better performance at a section thickness of 100 nm as the curve stays closer to the value of $0.2\Delta E$, but has a strong peak at 190 nm, where the color quickly changes from yellow to purple to blue. This difference might also effect the judgement of a ultramicrotome operator, who is not aware of this change observing sections under a different color temperature. The last plot shows that the cold light source provides a bigger total space of perceived color difference. 84

3.13 Left: Reflection of a fluorescent lamp with diffuser plate on the water surface of the trough. Right: Reflection of an edge lit illumination under similar conditions. The edge lit illumination is noticeably more uniform and and less scattered light from the background of the knife trough is visible. 85

4.1 Machine-based section acquisition process. 88

4.2 Integrated system for the machine-based acquisition of serial sections. The edge lit top light is visible overhanging above. The custom black anodized ultra wide knife is mounted on the ultramicrotome. The automated four-axis substrate manipulator is engaged in the knife trough. 90

4.3 Image of the back light diffuser. The two different lighting zones with different material thickness are visible on the back. 93

-
- 4.4 Screenshot of the web-based user interface for machine-based sample advance and alignment. The left part of the interface contains a six step wizard to guide the operator through the instrument setup. The camera image on the right is used to perform the coarse advance of the knife edge. The overlay cross-hair indicates the initial distance of 100 μm between sample block face and knife edge 94
- 4.5 Repetitive calculation of the contact point in 122 successive measurement runs. Initially the knife edge is positioned 101 μm away from the sample. The ambient temperature is nearly constant at 21°. The top image shows the estimated distance over a period of 5 h. The lower graph displays the relative change between two following estimates as a scatter plot. The rolling mean of 16 values is displayed as a dotted line. The deviations follow a normal distribution with a probability of 0.92 for the hypothesis test (Pearson's two-sided chi squared probability)[94]. The blue colored area represents the 1σ -interval of the estimates. A measurement run requires 140 s. 96
- 4.6 Key steps of the machine-based section collection cycle observed from a top view of the knife trough. The diamond knife is visible in the top of the images and a functionalized silicon substrate with seven channels positioned adjacent A) A Section ribbon is created and pushed into a water channel formed on the carrier substrate. B) The ribbon is separated by empty cuts. C) The ribbon is pushed completely inside the channel with an offset protrusion. D) The substrate is shifted to collect a next ribbon in an empty channel. A video of the collection cycle is included in the electronic appendix. 100
- 4.7 A panel of captured camera images (left) for 40 nm to 180 nm thick sections of empty epoxide blocks and the corresponding false color mappings (right) of the thickness estimation algorithm. The indicated section thickness is the set nominal value. In the lower part of each image the negative influence of light scattered from the background of the blue knife trough can be observed. 104

4.8 Ultra-thin sections obtained from a sample of PET embedded in Epofix. Thickness variations within sections arise from variations in the material properties, thermal expansion, block relaxation, elasticity and backlash. For thin sections (<75 nm) delamination can be observed as only every second section contains a piece of PET. This is due to the different material properties of PET and Epofix. 106

4.9 A) Topview of a block face with a carbonized origami structure embedded. B) 1045 sections obtained from the sample block and collected on three silicon wafers with each an area of 22 mm × 22 mm. C) Rendering of the reconstructed sample in Blender. . . . 113

A.1 Trimming Process. 1-4) Orientation of the block face shown like observed through the stereo microscope of the ultramicrotome. Hatched lines indicate areas that are removed through trimming. 5) Section ribbon attached to knife edge. 149

A.2 Illustration of the ribbon curvature caused by unequal lengths of the left and right sides of the block face. 153

A.3 Software architecture and system components 157

List of Tables

1.1	Comparison of the three commonly used tomography techniques used in life and material science	9
3.1	Comparison of the modeled evaporation for water and ethylene glycol for: $T = 20^\circ\text{C}, z = 53\text{ mm}, v_z = 2 \frac{\text{cm}}{\text{s}}, h_i = 4.8\text{ mm}, w_c = 1.2\text{ mm}$. . .	72
4.1	Performance values for the machine-based sample alignment	98
4.2	Characteristics of acquired sections for 4 samples. A carbonized cellulose origami structure and a model organoid of a mouse brain. . .	112

Bibliography

- [1] Irene Wacker, Eric Hummel, Steffen Burgold, and Rasmus Schröder, editors. *Volume Microscopy: Multiscale Imaging with Photons, Electrons, and Ions*. Neuromethods. Springer US, New York, 2020. ISBN 978-1-07-160690-2. doi: 10.1007/978-1-0716-0691-9. URL <https://www.springer.com/gp/book/9781071606902>.
- [2] W. M. Haynes, David R. Lide, and Thomas J. Bruno. *CRC Handbook of Chemistry and Physics*. CRC Press Inc, Boca Raton, 97th edition edition, 2016. ISBN 978-1-4987-5429-3.
- [3] Yanxin Zhuang, Ole Hansen, Thomas Knieling, Christian Wang, Pirmin Rombach, Walter Lang, Wolfgang Benecke, Markus Kehlenbeck, and Jörn Koblitz. Thermal stability of vapor phase deposited self-assembled monolayers for MEMS anti-stiction. *Journal of Micromechanics and Microengineering*, 16:2259, September 2006. doi: 10.1088/0960-1317/16/11/002.
- [4] Stephen J. Smith. Q&A: Array tomography. *BMC Biology*, 16(1):98, September 2018. ISSN 1741-7007. doi: 10.1186/s12915-018-0560-1. URL <https://doi.org/10.1186/s12915-018-0560-1>.
- [5] Kristina D. Micheva and Stephen J. Smith. Array tomography: a new tool for imaging the molecular architecture and ultrastructure of neural circuits. *Neuron*, 55(1):25–36, July 2007. ISSN 0896-6273. doi: 10.1016/j.neuron.2007.06.014.
- [6] Daisuke Koga, Satoshi Kusumi, Tatsuo Ushiki, and Tsuyoshi Watanabe. Integrative method for three-dimensional imaging of the entire Golgi apparatus

- by combining thiamine pyrophosphatase cytochemistry and array tomography using backscattered electron-mode scanning electron microscopy. *Biomedical Research*, 38(5):285–296, 2017. doi: 10.2220/biomedres.38.285.
- [7] M. A. Hayat. *Principles and Techniques of Electron Microscopy: Biological Applications*. Cambridge University Press, Cambridge, UK, 4. edition edition, April 2000. ISBN 978-0-521-63287-4.
- [8] Lis Melo, Adam Hitchcock, Viatcheslav Berejnov, Darija Susac, Juergen Stumper, and Gianluigi Botton. Evaluating focused ion beam and ultramicrotome sample preparation for analytical microscopies of the cathode layer of a polymer electrolyte membrane fuel cell. *Journal of Power Sources*, 312:23–35, April 2016. doi: 10.1016/j.powsour.2016.02.019.
- [9] G. McMahon and T. Malis. Ultramicrotomy of nanocrystalline materials. *Microscopy Research and Technique*, 31(4):267–274, 1995. ISSN 1097-0029. doi: 10.1002/jemt.1070310403. URL <https://onlinelibrary.wiley.com/doi/abs/10.1002/jemt.1070310403>.
- [10] Peter W. Hawkes. *The Beginnings of Electron Microscopy*. Academic Press, Orlando, 1985. ISBN 978-1-4832-8465-1.
- [11] Yoshiyuki Kubota, Jaerin Sohn, Sayuri Hatada, Meike Schurr, Jakob Straehle, Anjali Gour, Ralph Neujahr, Takafumi Miki, Shawn Mikula, and Yasuo Kawaguchi. A carbon nanotube tape for serial-section electron microscopy of brain ultrastructure. *Nature Communications*, 9(1):437, January 2018. ISSN 2041-1723. doi: 10.1038/s41467-017-02768-7. URL <https://www.nature.com/articles/s41467-017-02768-7>.
- [12] Irene Wacker, Waldemar Spomer, Andreas Hofmann, Marlene Thaler, Stefan Hillmer, Ulrich Gengenbach, and Rasmus R. Schröder. Hierarchical imaging: a new concept for targeted imaging of large volumes from cells to tissues. *BMC Cell Biology*, 17, December 2016. ISSN 1471-2121. doi: 10.1186/s12860-016-0122-8. URL <https://www.ncbi.nlm.nih.gov/pmc/articles/PMC5154069/>.

-
- [13] Christopher J. Peddie, Nalan Liv, Jacob P. Hoogenboom, and Lucy M. Collinson. Integrated light and scanning electron microscopy of GFP-expressing cells. *Methods in Cell Biology*, 124:363–389, 2014. ISSN 0091-679X. doi: 10.1016/B978-0-12-801075-4.00017-3.
- [14] Thomas Muller-Reichert and Paul Verkade. *Correlative Light and Electron Microscopy III*. Academic Press, Cambridge, MA, 2017. ISBN 978-0-12-809975-9.
- [15] Kristina D. Micheva and Marcel P. Bruchez. The Gain in Brain: Novel Imaging Techniques and Multiplexed Proteomic Imaging of Brain Tissue Ultrastructure. *Current Opinion in Neurobiology*, 22(1):94–100, February 2012. ISSN 0959-4388. doi: 10.1016/j.conb.2011.08.004. URL <https://www.ncbi.nlm.nih.gov/pmc/articles/PMC3265692/>.
- [16] Winfried Denk and Heinz Horstmann. Serial Block-Face Scanning Electron Microscopy to Reconstruct Three-Dimensional Tissue Nanostructure. *PLoS Biology*, 2(11), November 2004. ISSN 1544-9173. doi: 10.1371/journal.pbio.0020329. URL <https://www.ncbi.nlm.nih.gov/pmc/articles/PMC524270/>.
- [17] Dilawar Hassan, Sidra Amin, Amber Rehana Solangi, and Saima Q. Memon. Focused ion beam tomography. In Ishaq Ahmad and Tingkai Zhao, editors, *Ion Beam Techniques and Applications*, chapter 5. IntechOpen, London, 2020. ISBN 978-1-78984-571-6. doi: 10.5772/intechopen.88937. URL <https://doi.org/10.5772/intechopen.88937>.
- [18] Taro Koike and Hisao Yamada. Methods for array tomography with correlative light and electron microscopy. *Medical Molecular Morphology*, 52(1): 8–14, March 2019. ISSN 1860-1499. doi: 10.1007/s00795-018-0194-y. URL <https://doi.org/10.1007/s00795-018-0194-y>.
- [19] Irene U. Wacker, Lisa Veith, Waldemar Spomer, Andreas Hofmann, Marlene Thaler, Stefan Hillmer, Ulrich Gengenbach, and Rasmus R. Schröder. Multimodal Hierarchical Imaging of Serial Sections for Finding Specific

- Cellular Targets within Large Volumes. *Journal of Visualized Experiments: JoVE*, (133), March 2018. ISSN 1940-087X. doi: 10.3791/57059.
- [20] Doory Kim, Thomas J. Deerinck, Yaron M. Sigal, Hazen P. Babcock, Mark H. Ellisman, and Xiaowei Zhuang. Correlative Stochastic Optical Reconstruction Microscopy and Electron Microscopy. *PLOS ONE*, 10(4):e0124581, April 2015. ISSN 1932-6203. doi: 10.1371/journal.pone.0124581. URL <https://journals.plos.org/plosone/article?id=10.1371/journal.pone.0124581>.
- [21] Kenneth J. Hayworth, C. Shan Xu, Zhiyuan Lu, Graham W. Knott, Richard D. Fetter, Juan Carlos Tapia, Jeff W. Lichtman, and Harald F. Hess. Ultrastructurally smooth thick partitioning and volume stitching for large-scale connectomics. *Nature Methods*, 12(4):319–322, April 2015. ISSN 1548-7105. doi: 10.1038/nmeth.3292. URL <https://www.nature.com/articles/nmeth.3292>.
- [22] R. Schalek, A. Wilson, J. Lichtman, M. Josh, N. Kasthuri, D. Berger, S. Seung, P. Anger, K. Hayworth, and D. Aderhold. ATUM-based SEM for High-Speed Large-Volume Biological Reconstructions. *Microscopy and Microanalysis*, 18(S2):572–573, July 2012. ISSN 1431-9276, 1435-8115. doi: 10.1017/S1431927612004710. URL <https://www.cambridge.org/core/journals/microscopy-and-microanalysis/article/atumbased-sem-for-highspeed-largevolume-biological-reconstructions/E9928BFFFA737D80FE8EE1ACA3BC16ED>.
- [23] Leica Microsystems. ARTOS 3D Brochure, 2018. URL https://downloads.leica-microsystems.com/ARTOS%203D/Brochures/ARTOS_3D_Brochure_11_18_EN_RGB.pdf. Last Accessed: November 8th 2021.
- [24] Long Cheng, Weizhou Liu, Chao Zhou, Yongxiang Zou, and Zeng-Guang Hou. Automated Silicon-Substrate Ultra-Microtome for Automating the Collection of Brain Sections in Array Tomography. *IEEE/CAA Journal of Automatica Sinica*, 8(2):389–401, February 2021. ISSN 2329-9274. doi: 10.1109/JAS.2021.1003829.

-
- [25] Harald F. Hess, David Peale, and Patrick R. Lee. Sectioning volume samples, May 2015. Pat. No. US20150135917A1.
- [26] Timothy J. Lee, Aditi Kumar, Aishwarya H. Balwani, Derrick Brittain, Sam Kinn, Craig A. Tovey, Eva L. Dyer, Nuno M. da Costa, R. Clay Reid, Craig R. Forest, and Daniel J. Bumbarger. Large-scale neuroanatomy using LASSO: Loop-based Automated Serial Sectioning Operation. *PLOS ONE*, 13(10): e0206172, October 2018. ISSN 1932-6203. doi: 10.1371/journal.pone.0206172. URL <https://journals.plos.org/plosone/article?id=10.1371/journal.pone.0206172>.
- [27] Thomas Templier. MagC, magnetic collection of ultrathin sections for volumetric correlative light and electron microscopy. *eLife*, 8:e45696, July 2019. ISSN 2050-084X. doi: 10.7554/eLife.45696. URL <https://doi.org/10.7554/eLife.45696>.
- [28] Timothy J. Lee, Mighten C. Yip, Aditi Kumar, Colby F. Lewallen, Daniel J. Bumbarger, R. Clay Reid, and Craig R. Forest. Capillary-Based and Stokes-Based Trapping of Serial Sections for Scalable 3D-EM Connectomics. *eNeuro*, 7(2), March 2020. ISSN 2373-2822. doi: 10.1523/ENEURO.0328-19.2019. URL <https://www.eneuro.org/content/7/2/ENEURO.0328-19.2019>.
- [29] RMC Boeckeler. ATUMtome Automated Tape Collection System, 2021. URL <https://www.boeckeler.com/solutions/ultramicrotomes/atumtome--automated-tape-collecting-ultramicrotome>. Last Accessed: June 1st 2021.
- [30] M. A. Gorycki. Simple and rapid block face alignment methods for the ultramicrotome. *Stain Technology*, 52(5):255–260, September 1977. ISSN 0038-9153.
- [31] Boeckeler Instruments. Datasheet - PTXL, 2021. URL <https://boeckeler.com/sample-preparation/ultramicrotomy/ptxl--powertome>. Last Accessed: September 9th 2021.

- [32] Dieter Frösch, Christel Westphal, and Karlheinz Bachhuber. A determination of thickness and surface relief in reembedded sections of an epoxy- and a melamine-resin containing ferritin as size standard. *Ultramicroscopy*, 17(2):141–146, 1985. ISSN 0304-3991. doi: 10.1016/0304-3991(85)90007-5. URL <https://www.sciencedirect.com/science/article/pii/0304399185900075>.
- [33] Sebastian M. Markert, Vivien Bauer, Thomas S. Muenz, Nicola G. Jones, Frederik Helmprobst, Sebastian Britz, Markus Sauer, Wolfgang Rössler, Markus Engstler, and Christian Stigloher. 3D subcellular localization with superresolution array tomography on ultrathin sections of various species. *Methods in Cell Biology*, 140:21–47, 2017. ISSN 0091-679X. doi: 10.1016/bs.mcb.2017.03.004.
- [34] Hilton H. Mollenhauer. Artifacts caused by dehydration and epoxy embedding in transmission electron microscopy. *Microscopy Research and Technique*, 26(6):496–512, 1993. ISSN 1097-0029. doi: <https://doi.org/10.1002/jemt.1070260604>. URL <https://analyticalsciencejournals.onlinelibrary.wiley.com/doi/abs/10.1002/jemt.1070260604>.
- [35] Didima M. D. De Groot. Comparison of methods for the estimation of the thickness of ultrathin tissue sections. *Journal of Microscopy*, 151(1): 23–42, 1988. ISSN 1365-2818. doi: <https://doi.org/10.1111/j.1365-2818.1988.tb04610.x>. URL <https://onlinelibrary.wiley.com/doi/abs/10.1111/j.1365-2818.1988.tb04610.x>.
- [36] T. Kaneko, H. Sato, Y. Tani, and M. O-hori. Self-Excited Chatter and its Marks in Turning. *Journal of Engineering for Industry*, 106(3):222–228, August 1984. ISSN 0022-0817. doi: 10.1115/1.3185937. URL <https://doi.org/10.1115/1.3185937>.
- [37] Günter Spur. *Handbuch Spanen*. Carl Hanser Verlag GmbH & Co. KG, München, 2. edition edition, 2014. ISBN 978-3-446-42826-3.
- [38] J. Rostgaard and K. Qvortrup. Ultrathin sectioning for electron microscopy: The distilled water in the knife trough may extract phosphatase reaction

- products from the sections. *Journal of Microscopy*, 156(2):253–257, 1989. ISSN 1365-2818. doi: <https://doi.org/10.1111/j.1365-2818.1989.tb02924.x>. URL <https://onlinelibrary.wiley.com/doi/abs/10.1111/j.1365-2818.1989.tb02924.x>.
- [39] Dimitri Vanhecke, Luca Studer, and Daniel Studer. Cryoultramicrotomy. In John Kuo, editor, *Electron Microscopy: Methods and Protocols*, Methods in Molecular Biology™, pages 175–197. Humana Press, Totowa, 2007. ISBN 978-1-59745-294-6. doi: 10.1007/978-1-59745-294-6_9. URL https://doi.org/10.1007/978-1-59745-294-6_9.
- [40] Wolf H. Fahrenbach. Continuous serial thin sectioning for electron microscopy. *Journal of Electron Microscopy Technique*, 1(4):387–398, 1984. ISSN 1553-0817. doi: 10.1002/jemt.1060010407. URL <https://onlinelibrary.wiley.com/doi/abs/10.1002/jemt.1060010407>.
- [41] Waldemar Spomer. *Neues Konzept zur automatisierten Handhabung von Ultramikrotomproben*. Dissertation, Karlsruhe Institute of Technology, 2017.
- [42] Eduardo Couve. Controlled mounting of serial sections for electron microscopy. *Journal of Electron Microscopy Technique*, 3(4):453–454, 1986. ISSN 1553-0817. doi: <https://doi.org/10.1002/jemt.1060030408>. URL <https://onlinelibrary.wiley.com/doi/abs/10.1002/jemt.1060030408>.
- [43] Waldemar Spomer, Andreas Hofmann, Irene Wacker, Len Ness, Pat Brey, Rasmus R. Schroder, and Ulrich Gengenbach. Advanced substrate holder and multi-axis manipulation tool for ultramicrotomy. *Microscopy and Microanalysis*, 21:1277–1278, 2015. ISSN 1431-9276, 1435-8115. doi: 10.1017/S1431927615007175. URL <https://www.cambridge.org/core/journals/microscopy-and-microanalysis/article/advanced-substrate-holder-and-multiaxis-manipulation-tool-for-ultramicrotomy/E1814676CBC41BD29557A809CD2E43FC>.

- [44] Boeckeler Instruments. ASH2 Data Sheet, 2021. URL <https://boeckeler.com/sample-preparation/ultramicrotomy/ash2--advanced-substrate-holder-attachment-for-serial-sectioning>. Last Accessed: June 13th 2021.
- [45] Agnes Burel, Marie-Thérèse Lavault, Clément Chevalier, Helmut Gnaegi, Sylvain Prigent, Antonio Mucciolo, Stéphanie Dutertre, Bruno M. Humbel, Thierry Guillaudeux, and Irina Kolotuev. A targeted 3D EM and correlative microscopy method using SEM array tomography. *Development*, 145(12), June 2018. ISSN 0950-1991, 1477-9129. doi: 10.1242/dev.160879. URL <https://dev.biologists.org/content/145/12/dev160879>.
- [46] Science Services. DiATOME diamantmesser, ultra ats 35°, 3,0mm, 2022. URL <https://www.scienceservices.de/diatome-diamantmesser-ultra-ats-35-3-0mm.html>. Last Accessed: February 9th 2022.
- [47] L. D. Peachey. Thin sections. I. A study of section thickness and physical distortion produced during microtomy. *The Journal of Biophysical and Biochemical Cytology*, 4(3):233–242, May 1958. ISSN 0095-9901. doi: 10.1083/jcb.4.3.233.
- [48] Toshio SAKAI. Relation between Thickness and Interference Colors of Biological Ultrathin Section. *Journal of Electron Microscopy*, 29(4):369–375, January 1980. ISSN 0022-0744. doi: 10.1093/oxfordjournals.jmicr.o.a050254. URL <https://doi.org/10.1093/oxfordjournals.jmicr.o.a050254>.
- [49] Leslie J. Atkins and Richard C. Elliott. Investigating thin film interference with a digital camera. *American Journal of Physics*, 78(12):1248–1253, November 2010. ISSN 0002-9505. doi: 10.1119/1.3490011. URL <https://aapt.scitacion.org/doi/10.1119/1.3490011>.

-
- [50] Johannes Cyrill Matenaers. *Praktikable Methoden zur Dickenmessung histologischer Kunststoffschnittpräparate in quantitativ-stereologischen Analysen mit der physikalischen Disektormethode*. Dissertation, Ludwig-Maximilians-Universität München, July 2020. URL <https://edoc.ub.uni-muenchen.de/27072/>.
- [51] Kenneth J. Hayworth, David Peale, Michał Januszewski, Graham W. Knott, Zhiyuan Lu, C. Shan Xu, and Harald F. Hess. Gas cluster ion beam SEM for imaging of large tissue samples with 10 nm isotropic resolution. *Nature Methods*, 17(1):68–71, January 2020. ISSN 1548-7105. doi: 10.1038/s41592-019-0641-2. URL <https://www.nature.com/articles/s41592-019-0641-2>.
- [52] Kenneth Jeffrey Hayworth, Richard Schalek, Juan Carlos Tapia, Narayanan Kasthuri, and Jeff Lichtman. Methods, apparatuses and systems for collection of tissue sections, January 2014. Pat. No. US20140026683A1.
- [53] Kenneth J. Hayworth, Josh L. Morgan, Richard Schalek, Daniel R. Berger, David G. C. Hildebrand, and Jeff W. Lichtman. Imaging ATUM ultrathin section libraries with WaferMapper: a multi-scale approach to EM reconstruction of neural circuits. *Frontiers in Neural Circuits*, 8: 68, June 2014. ISSN 1662-5110. doi: 10.3389/fncir.2014.00068. URL <https://www.ncbi.nlm.nih.gov/pmc/articles/PMC4073626/>.
- [54] K. J. Hayworth, N. Kasthuri, R. Schalek, and J. W. Lichtman. Automating the Collection of Ultrathin Serial Sections for Large Volume TEM Reconstructions. *Microscopy and Microanalysis*, 12(S02):86–87, August 2006. ISSN 1435-8115, 1431-9276. doi: 10.1017/S1431927606066268. URL <https://www.cambridge.org/core/journals/microscopy-and-microanalysis/article/automating-the-collection-of-ultrathin-serial-sections-for-large-volume-tem-reconstructions/EBDFF85F5E7A2D10F95602B6E1ADDE91>.
- [55] Brett J. Graham, David Grant Colburn Hildebrand, Aaron T. Kuan, Jasper T. Maniates-Selvin, Logan A. Thomas, Brendan L. Shanny, and Wei-Chung Allen Lee. High-throughput transmission electron microscopy with

- automated serial sectioning. *bioRxiv*, 2019. doi: 10.1101/657346. URL <https://www.biorxiv.org/content/early/2019/06/02/657346>.
- [56] Leica Microsystems. Fast, Precise Serial Sectioning for Array Tomography: the new ARTOS 3D Ultramicrotome, September 2018. URL <https://www.youtube.com/watch?v=V4XIqdRjc28>. Last Accessed: November 11th 2021.
- [57] Brian Carroll Tabb and Keith Rogers. Block alignment for microtomes, December 2011. Pat. No. US8074545B1.
- [58] Hwai-Jyh Michael Yang and Xuan S. Bui. Microtome with surface orientation sensor to sense orientation of surface of sample, May 2016. Pat. No. US9347857B2.
- [59] Kevin L. Briggman. Miniature serial sectioning microtome for block-face imaging, November 2015. Pat. No. WO2015175525A1.
- [60] Janelia Research Campus HHMI. iTome Movie 4x Speed Improvement, August 2016. URL <https://vimeo.com/179387741>. Last Accessed: December 1st 2021.
- [61] Long Cheng and Weizhou Liu. An Effective Microscopic Detection Method for Automated Silicon-Substrate Ultra-microtome (ASUM). *Neural Processing Letters*, 53(3):1723–1740, November 2019. ISSN 1573-773X. doi: 10.1007/s11063-019-10134-5. URL <https://doi.org/10.1007/s11063-019-10134-5>.
- [62] Richard D. Campbell. A Method for Making Ribbons of Semithin Plastic Sections. *Stain Technology*, 56(4), January 1981. ISSN 0038-9153. doi: 10.3109/10520298109067319. URL <https://doi.org/10.3109/10520298109067319>.
- [63] K. S. Bedi. A simple method of measuring the thickness of semi-thin and ultra-thin sections. *Journal of Microscopy*, 148(1):107–111, 1987. ISSN 1365-2818. doi: <https://doi.org/10.1111/j.1365-2818.1987.tb02858>.

- x. URL <https://onlinelibrary.wiley.com/doi/abs/10.1111/j.1365-2818.1987.tb02858.x>.
- [64] Cyrill Matenaers, Bastian Popper, Alexandra Rieger, Rüdiger Wanke, and Andreas Blutke. Practicable methods for histological section thickness measurement in quantitative stereological analyses. *PLOS ONE*, 13(2): e0192879, February 2018. ISSN 1932-6203. doi: 10.1371/journal.pone.0192879. URL <https://journals.plos.org/plosone/article?id=10.1371/journal.pone.0192879>.
- [65] M. A. Williams and G. A. Meek. Studies on thickness variation in ultrathin sections for electron microscopy. *Journal of the Royal Microscopical Society*, 85(3):337–352, 1966. ISSN 1365-2818. doi: <https://doi.org/10.1111/j.1365-2818.1966.tb02193.x>. URL <https://onlinelibrary.wiley.com/doi/abs/10.1111/j.1365-2818.1966.tb02193.x>.
- [66] Tony Flaherty and Gerard M. O’Connor. Application of spectral reflectivity to the measurement of thin-film thickness. In Vincent Toal, Norman Douglas McMillan, Gerard M. O’Connor, Eon O’Mongain, Austin F. Duke, John F. Donegan, James A. McLaughlin, Brian D. MacCraith, and Werner J. Blau, editors, *Opto-Ireland 2002: Optics and Photonics Technologies and Applications*, volume 4876, pages 976 – 983, Galway, 2003. International Society for Optics and Photonics, SPIE. doi: 10.1117/12.464264. URL <https://doi.org/10.1117/12.464264>.
- [67] Lloyd Silverman, Berit Schreiner, and David Glick. Measurement of thickness within sections by quantitative electron microscopy. *Journal of Cell Biology*, 40(3):768–772, March 1969. ISSN 0021-9525. doi: 10.1083/jcb.40.3.768. URL <https://doi.org/10.1083/jcb.40.3.768>.
- [68] Jon Sparring, Mahdieh Khanmohammadi, Sune Darkner, Nicoletta Nava, Jens Rondel Nyengaard, and Eva Bjørn Wedel Jensen. Estimating the thickness of ultra thin sections for electron microscopy by image statistics. In *2014 IEEE 11th International Symposium on Biomedical Imaging (ISBI)*, pages 157–160, Beijing, April 2014. doi: 10.1109/ISBI.2014.6867833.

- [69] H. E. Huxley. The double array of filaments in cross-striated muscle. *The Journal of Biophysical and Biochemical Cytology*, 3(5):631–648, September 1957. ISSN 0095-9901. URL <https://www.ncbi.nlm.nih.gov/pmc/articles/PMC2224118/>.
- [70] Eugene Hecht. *Optics, Global Edition*. Pearson Education Limited, London, 5. edition edition, 2016. ISBN 978-1-292-09693-3.
- [71] K. Jensen and D. Anastassiou. Subpixel edge localization and the interpolation of still images. *IEEE Transactions on Image Processing*, 4(3):285–295, March 1995. ISSN 1941-0042. doi: 10.1109/83.366477.
- [72] T. Hermosilla, E. Bermejo, A. Balaguer, and L. A. Ruiz. Non-linear fourth-order image interpolation for subpixel edge detection and localization. *Image and Vision Computing*, 26(9):1240–1248, September 2008. ISSN 0262-8856. doi: 10.1016/j.imavis.2008.02.012. URL <https://www.sciencedirect.com/science/article/pii/S0262885608000577>.
- [73] Bo Zhang, Josiane Zerubia, and Jean-Christophe Olivo-Marin. Gaussian approximations of fluorescence microscope point-spread function models. *Applied Optics*, 46(10):1819–1829, April 2007. ISSN 2155-3165. doi: 10.1364/AO.46.001819. URL <https://www.osapublishing.org/ao/abstract.cfm?uri=ao-46-10-1819>.
- [74] Charles R. Harris, K. Jarrod Millman, Stéfan J. van der Walt, Ralf Gommers, Pauli Virtanen, David Cournapeau, Eric Wieser, Julian Taylor, Sebastian Berg, Nathaniel J. Smith, Robert Kern, Matti Picus, Stephan Hoyer, Marten H. van Kerkwijk, Matthew Brett, Allan Haldane, Jaime Fernández del Río, Mark Wiebe, Pearu Peterson, Pierre Gérard-Marchant, Kevin Sheppard, Tyler Reddy, Warren Weckesser, Hameer Abbasi, Christoph Gohlke, and Travis E. Oliphant. Array programming with NumPy. *Nature*, 585(7825):357–362, September 2020. doi: 10.1038/s41586-020-2649-2. URL <https://doi.org/10.1038/s41586-020-2649-2>.

-
- [75] Pauli Virtanen, Ralf Gommers, Travis E. Oliphant, Matt Haberland, Tyler Reddy, David Cournapeau, Evgeni Burovski, Pearu Peterson, Warren Weckesser, Jonathan Bright, Stéfan J. van der Walt, Matthew Brett, Joshua Wilson, K. Jarrod Millman, Nikolay Mayorov, Andrew R. J. Nelson, Eric Jones, Robert Kern, Eric Larson, C J Carey, İlhan Polat, Yu Feng, Eric W. Moore, Jake VanderPlas, Denis Laxalde, Josef Perktold, Robert Cimrman, Ian Henriksen, E. A. Quintero, Charles R. Harris, Anne M. Archibald, Antônio H. Ribeiro, Fabian Pedregosa, Paul van Mulbregt, and SciPy 1.0 Contributors. SciPy 1.0: Fundamental Algorithms for Scientific Computing in Python. *Nature Methods*, 17:261–272, 2020. doi: 10.1038/s41592-019-0686-2.
- [76] Philipp Schmidt. Entwicklung einer mikrofluidischen Vorrichtung zur Handhabung von ultradünnen lamellaren Objekten, 2020. Master Thesis. Karlsruhe Institut of Technology (unpublished).
- [77] Sangwha Lee, Joon-Seo Park, and T. Randall Lee. The Wettability of Fluoropolymer Surfaces: Influence of Surface Dipoles. *Langmuir*, 24(9): 4817–4826, May 2008. ISSN 0743-7463. doi: 10.1021/la700902h. URL <https://doi.org/10.1021/la700902h>.
- [78] Jean Berthier, Kenneth A. Brakke, and Erwin Berthier. *Open Microfluidics*. Scrivener Publishing, Beverly, 1st edition, July 2016. ISBN 978-1-118-72080-6.
- [79] Pierre-Gilles de Gennes, Françoise Brochard-Wyart, and David Quere. *Capillarity and Wetting Phenomena: Drops, Bubbles, Pearls, Waves*. Springer, New York, 2004. ISBN 978-0-387-00592-8. doi: 10.1007/978-0-387-21656-0. URL <https://www.springer.com/de/book/9780387005928>.
- [80] Bastian E. Rapp. *Microfluidics: Modeling, Mechanics and Mathematics*. Elsevier, Amsterdam, 2016. ISBN 978-1-4557-3141-1.
- [81] Wei-Chang Tian and Erin Finehout. Introduction to Microfluidics. In *Microfluidics for Biological Applications*, pages 1–34. Springer US, Boston,

2009. ISBN 978-0-387-09480-9. doi: 10.1007/978-0-387-09480-9_1. URL https://doi.org/10.1007/978-0-387-09480-9_1.
- [82] Fredric C. Arnold and Alfred J. Engel. Evaporation of Pure Liquids from Open Surfaces. In Jan B. H. J. Linders, editor, *Modelling of Environmental Chemical Exposure and Risk*, NATO ASI Series, pages 61–71. Springer Netherlands, Dordrecht, 2001. ISBN 978-94-010-0884-6. doi: 10.1007/978-94-010-0884-6_6. URL https://doi.org/10.1007/978-94-010-0884-6_6.
- [83] Albert A. Hummel, Karl O. Braun, and M. Catherine Fehrenbacher. Evaporation of a liquid in a flowing airstream. *American Industrial Hygiene Association Journal*, 57(6):519–525, 1996. ISSN 0002-8894. doi: 10.1080/15428119691014729. URL <https://doi.org/10.1080/15428119691014729>.
- [84] P. T. Wasiolek, J. J. Whicker, H. Gong, and J. C. Rodgers. Room airflow studies using sonic anemometry. *Indoor Air*, 9(2):125–133, 1999. ISSN 0905-6947. doi: 10.1111/j.1600-0668.1999.t01-2-00007.x.
- [85] Abraham Ulman. Formation and structure of self-assembled monolayers. *Chemical Reviews*, 96(4):1533–1554, January 1996. ISSN 0009-2665, 1520-6890. doi: 10.1021/cr9502357. URL <https://pubs.acs.org/doi/10.1021/cr9502357>.
- [86] Jiri Cech and Rafael Taboryski. Stability of FDTS monolayer coating on aluminum injection molding tools. *Applied Surface Science*, 259:538–541, 2012. ISSN 0169-4332. doi: 10.1016/j.apsusc.2012.07.078. URL <https://www.sciencedirect.com/science/article/pii/S0169433212012688>.
- [87] Wenqian Feng, Erica Ueda, and Pavel A. Levkin. Droplet Microarrays: From Surface Patterning to High-Throughput Applications. *Advanced Materials*, 30(20):1706111, 2018. ISSN 1521-4095. doi: 10.1002/adma.201706111. URL <https://onlinelibrary.wiley.com/doi/abs/10.1002/adma.201706111>.

-
- [88] Xiaozhu Zhou, Freddy Boey, Fengwei Huo, Ling Huang, and Hua Zhang. Chemically Functionalized Surface Patterning. *Small*, 7(16):2273–2289, 2011. ISSN 1613-6829. doi: 10.1002/smll.201002381. URL <https://onlinelibrary.wiley.com/doi/abs/10.1002/smll.201002381>.
- [89] Younan Xia, Milan Mrksich, Enoch Kim, and George M. Whitesides. Microcontact Printing of Octadecylsiloxane on the Surface of Silicon Dioxide and Its Application in Microfabrication. *Journal of the American Chemical Society*, 117(37):9576–9577, September 1995. ISSN 0002-7863. doi: 10.1021/ja00142a031. URL <https://doi.org/10.1021/ja00142a031>.
- [90] Sofia Madrigal Gamboa. Manipulation of ultra-thin sections in microfluidic channels generated by surface functionalization methods, 2018. Bachelor Thesis. Karlsruher Institut of Technology (unpublished).
- [91] Christine Chapeau and Dr CLAUDE Gagnon. Nitrocellulose and Polyvinyl Coatings Prevent Sperm Adhesion to Glass Without Affecting the Motility of Intact and Demembrated Human Spermatozoa. *Journal of Andrology*, 8(1):34–40, 1987. ISSN 1939-4640. doi: 10.1002/j.1939-4640.1987.tb02416.x. URL <https://onlinelibrary.wiley.com/doi/abs/10.1002/j.1939-4640.1987.tb02416.x>.
- [92] O. S. Heavens. *The Optical Properties of Thin Solid Films*. Dover Publications Inc., New York, 2nd revised edition, February 2011. ISBN 978-0-486-66924-3.
- [93] M. Ronnier Luo, Guihua Cui, and Changjun Li. Uniform colour spaces based on CIECAM02 colour appearance model. *Color Research & Application*, 31(4):320–330, 2006. doi: <https://doi.org/10.1002/col.20227>. URL <https://onlinelibrary.wiley.com/doi/abs/10.1002/col.20227>.
- [94] Ralph D’Agostino and E. S. Pearson. Tests for Departure from Normality. Empirical Results for the Distributions of b_2 and b_1 . *Biometrika*, 60(3): 613–622, 1973. ISSN 0006-3444. doi: 10.2307/2335012. URL <https://www.jstor.org/stable/2335012>.

- [95] Johannes Schindelin, Ignacio Arganda-Carreras, Erwin Frise, Verena Kaynig, Mark Longair, Tobias Pietzsch, Stephan Preibisch, Curtis Rueden, Stephan Saalfeld, Benjamin Schmid, Jean-Yves Tinevez, Daniel James White, Volker Hartenstein, Kevin Eliceiri, Pavel Tomancak, and Albert Cardona. Fiji: an open-source platform for biological-image analysis. *Nature Methods*, 9(7):676–682, 2012. ISSN 1548-7105. doi: 10.1038/nmeth.2019. URL <https://www.nature.com/articles/nmeth.2019>.
- [96] Erik B. Bloss, Mark S. Cembrowski, Bill Karsh, Jennifer Colonell, Richard D. Fetter, and Nelson Spruston. Structured Dendritic Inhibition Supports Branch-Selective Integration in CA1 Pyramidal Cells. *Neuron*, 89(5):1016–1030, March 2016. ISSN 0896-6273. doi: 10.1016/j.neuron.2016.01.029. URL [https://www.cell.com/neuron/abstract/S0896-6273\(16\)00054-4](https://www.cell.com/neuron/abstract/S0896-6273(16)00054-4).
- [97] Jong-Cheol Rah, Erhan Bas, Jennifer Colonell, Yuriy Mishchenko, Bill Karsh, Richard Fetter, Eugene Myers, Dmitri Chklovskii, Karel Svoboda, Timothy Harris, and John Isaac. Thalamocortical input onto layer 5 pyramidal neurons measured using quantitative large-scale array tomography. *Frontiers in Neural Circuits*, 7:177, 2013. ISSN 1662-5110. doi: 10.3389/fncir.2013.00177. URL <https://www.frontiersin.org/article/10.3389/fncir.2013.00177>.

List of Publications

Journal articles

- [98] Julian Hoffmann, Sofia Madrigal Gamboa, Andreas Hofmann, Hartmut Gliemann, Alexander Welle, Irene Wacker, Rasmus R. Schröder, Len Ness, Veit Hagenmeyer, and Ulrich Gengenbach. Siloxane-functionalised surface patterns as templates for the ordered deposition of thin lamellar objects. *Scientific Reports*, 9(1):17952, November 2019. ISSN 2045-2322. doi: 10.1038/s41598-019-54507-1. URL <https://www.nature.com/articles/s41598-019-54507-1>.

Patents

- [99] Ulrich Gengenbach, Julian Hoffmann, Andreas Hofmann, Waldemar Spomer, Rasmus Schröder, Irene Wacker-Schröder, Leonard J. Ness, and Warren J. P. Brey. Mikrotom und Verfahren zum Herstellen von Dünnschnitten aus einer Probe mit Hilfe eines Mikrotoms, June 2019. URL <https://depatinet.dpma.de/DepatisNet/depatinet?action=bibdat&docid=DE102017129537A1>. Pat. No. DE102017129537A1.
- [100] Olaf Simon and Julian Hoffmann. System mit einer vorzugsweise binären Codierung und einem Mobilteil mit Lesekopf zur Positionsbestimmung, April 2018. URL <https://depatinet.dpma.de/Depati>

- sNet/depatismet?action=bibdat&docid=DE102017009331A1. Pat. No. DE102017009331A1.
- [101] Olaf Simon, Steffen Quadt, Michael Müller, and Julian Hoffmann. Dekodierung eines manchester codes ohne PLL für kurze Datensequenzen, December 2013. URL <https://depatismet.dpma.de/Depatismet/depatismet?action=bibdat&docid=W0002013178318A1>. Pat. No. WO2013178318A1.
- [102] Olaf Simon, Julian Hoffmann, Gunnar Meyrowitz, Christian Schaaf, and Christian Enderle. Anordnung zur Datenübertragung über einen Datenbus und Verfahren zur Datenübertragung bei einer Anordnung zur Datenübertragung über einen Datenbus, March 2016. URL <https://depatismet.dpma.de/Depatismet/depatismet?action=bibdat&docid=W0002016045766A1>. Pat. No. WO2016045766A1.
- [103] Olaf Simon, Julian Hoffmann, and Valentin Ehmman. Verfahren zur Übermittlung von Telegrammen, Bussystem und Verfahren zur Vergabe von Kennungen, May 2017. URL <https://depatismet.dpma.de/Depatismet/depatismet?action=bibdat&docid=DE102016006428B4>. Pat. No. DE102016006428B4.
- [104] Olaf Simon, Christian Enderle, Julian Hoffmann, and Tino Schwilk. Verfahren zur Bestimmung der Position, insbesondere Winkelstellung, einer zu Sensoren relativ bewegbar angeordneten Maßverkörperung, und Anordnung zur Durchführung eines solchen Verfahrens, September 2018. URL <https://depatismet.dpma.de/Depatismet/depatismet?action=bibdat&docid=DE102018001851A1>. Pat. No. DE102018001851A1.
- [105] Olaf Simon, Dennis Rädle, Julian Hoffmann, and Daniel Simon Fuchs. Vorrichtung, insbesondere Maschine, zum Herstellen von Wieganddraht aus einem Draht, insbesondere Impulsdraht, und Verfahren zum Betreiben der Vorrichtung, July 2018. URL <https://depatismet.dpma.de/Depatismet/depatismet?action=bibdat&docid=DE102017002939B3>. Pat. No. DE102017002939B3.

- [106] Olaf Simon, Julian Hoffmann, and Gunnar Meyrowitz. Verfahren und system zum Betreiben einer elektrischen Schnittstelle, February 2020. URL <https://depatisnet.dpma.de/DepatisNet/depatisnet?action=bibdat&docid=EP000003295574B1>. Pat. No. EP3295574B1.

A Appendix

A.1 Preparation of the sample block

The handling approach relies on the formation of sturdy and straight ribbons. Following the steps to obtain such ribbons as depicted in Figure A.1 Step 5 are described.

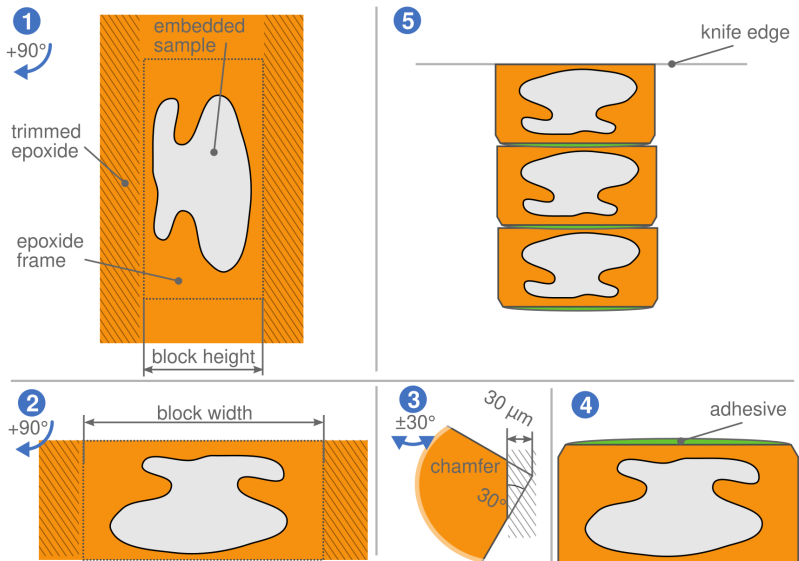


Figure A.1: Trimming Process. 1-4) Orientation of the block face shown like observed through the stereo microscope of the ultramicrotome. Hatched lines indicate areas that are removed through trimming. 5) Section ribbon attached to knife edge.

The sample block is trimmed with a 90° trimming knife (Trim 90, Diatome) and an ultramicrotome (Powertome, RMC Boeckeler Instruments). The 90° trimming knife allows a trimming of the block face which does not increase during the sectioning. A consistent block face is beneficial for the machine-based section collection. All sides are trimmed 250 µm deep. This depth is limited due to the current trimming knives. Beyond that limit, the lateral sides show a noticeable degradation of the surface quality which also impairs the sectioning process. The trimming follows the general best practice, e.g. the sample should be mounted firmly, the coarse trimming is performed with a razor blade and trimmed sections are removed by air blow [7]. The block is trimmed in rectangular profile with two chamfers added on the lower side of the block as illustrated in Figure A.1 Step 3. To visually support the trimming process for the operator, the developed software displays a length adjustable overlay on top of the camera image. This overlay is used to measure and adjust the distances of the sides during the trimming procedure by providing a reference where the trimming knife edge must be positioned. Alternatively, an eyepiece with measuring scale can be used or a motorized stage with position feedback.

Prior to the trimming, the sample is oriented inside the desired block profile by turning the arc segment holder around the arm axis. This resulting orientation around the arm axis defines the positions of lower, upper, left and right side of the block during trimming and sectioning. The orientation should be chosen carefully to have the sample centered and symmetrically inside the block face for good sectioning qualities. Afterwards, the front of the block is trimmed until the sample lies just beneath the surface. In the next steps, the sides of the block are trimmed that define the block face dimensions. The precise rotation required in the following steps can be achieved by observing markings on the rotation scale with 5x magnification through the stereo microscope.

The block is rotated 90° clockwise around the arm axis, as depicted in Figure A.1 **Step 1**. This step defines the height of the block face. Upper and lower side of the block are trimmed with the left respectively right side of the trimming knife. Both sides of the block face are trimmed in the same step by laterally shifting the trimming knife without altering the rotation of the specimen holder. This way

the upper and lower side of the block are guaranteed to be parallel, which is a requirement for the desired formation of straight ribbons [19]. The height of the block, defined by the distance between upper and lower side of the block, is a potential free parameter and can be chosen to fit the sample dimensions. A higher block face is more difficult to section and decreases the number of sections that can be collected on a single piece of carrier substrate. Thus, the smallest possible block height is desirable. In some cases a small frame of epoxide around the sample can be beneficial for not well infiltrated or inhomogeneous samples as it increases the section stability.

The block is rotated another 90° clockwise such that the sample rests upside down to the intended sectioning direction, as depicted in Figure A.1 **Step 2**. This step defines the width of the block face. The rotation must be accurately performed to create orthogonal block sides. An incorrect rotation results in an inclination of the sides and creates a non rectangular block face. For a non rectangular block face, the upper and lower sides of the section do not match and the non overlapping parts are not properly separated from the knife edge which impairs the sectioning process [7]. As the sample is ideally positioned in the center of the block face, it is desirable to trim both sides so that the sample is embedded symmetrically. During sectioning, this prevents bending of the ribbon due to inhomogeneous compression of the left and the right sides of the sections [7]. The width of the block should be approximately 10 % to 15 % smaller than the channel width of the deposition pattern. For a typical channel width of 1200 μm, the block width should be 1050 μm. This limits the maximum rotation of section inside the channel and thus also the angle under which the channel boundary is encountered. If a section can rotate too much inside the channels, the risk of channel jamming is significantly increased.

In the next step chamfers are added to the block, as depicted in in Figure A.1 **Step 3**. The chamfers are added to reduce the risk of channel jamming further. The block is rotated 30° clockwise and the knife aligned to the left/right lower edge of the block. The knife is then moved by 30 μm inward and the chamfer is trimmed. This step is repeated for both edges on the lower side of the block. The chamfer provides a side at which the first section of the ribbon can slide along the

walls of the channel. The trimming of the chamfers can cause the formation of burrs at the lower side of the sample block. These burrs can impair the section process and should be removed with a piece of wetted lens cleaning tissue.

In the last step, adhesive is added to the lower side of the block face to facilitate the formation of section ribbons, as depicted in Figure A.1 **Step 4**. For the adhesive application the block face is turned 180°, so that the application can be monitored through the stereo microscope. An established method uses an adhesive (Patex) diluted with xylene [19]. The mixture ratio differs greatly in literature. Here a ratio of 1:8 is used which is a rather low-viscosity mixture. The low-viscosity improves the complete wetting of the lower side of the block with adhesive. Special care has to be taken that no excess adhesive reaches in particular the upper side of the block face, as this can cause sections to stick to the block face and be dragged over the knife edge. The retraction of sections causes extreme wear on the diamond edge and if observed, the cutting process should be stopped immediately. Further adhesive on the wrong side of the block increases the adhesion to the knife edge and impairs the machine-based section separation from the knife edge. The low concentration of adhesive in the mixture ensures that only a thin film of adhesive is deposited on the upper side of the block. The bonding strength can be increased by applying the adhesive a second time. For the automated section acquisition it is advised to apply adhesive two to three times as a strong ribbon is beneficial when the section ribbon slides along the channel walls.

A.2 Ribbon Curvature

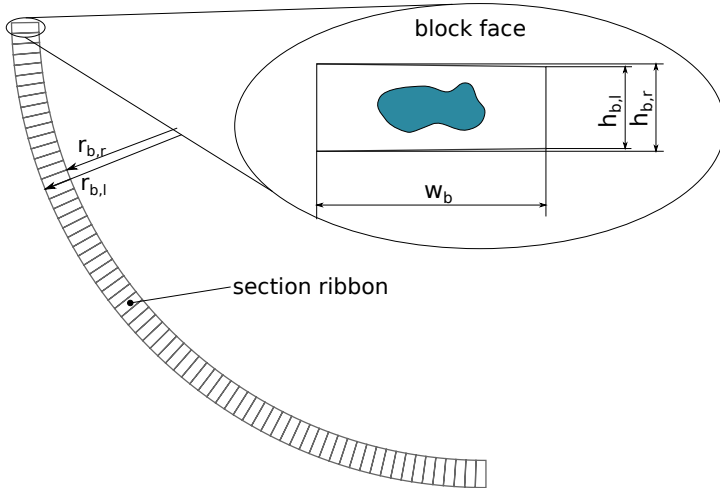


Figure A.2: Illustration of the ribbon curvature caused by unequal lengths of the left and right sides of the block face.

Figure A.2 depicts the formation of a curved ribbon. The relation between the section geometry and the ribbon radius r_s is given by

$$r_s = \frac{w_b}{1 - \frac{h_{b,r}}{h_{b,l}}} \quad (\text{A.1})$$

A.3 Evaporation Model

```
1 %pylab notebook
2
3 # Parameters
4 z = 53e-3*100      # Trough
5 vz = 2             # Air Flow speed [cm/s] 1.6 ..6
6 g = 9.81          # Gravitational Constant
7 h_i = 4.8e-3      # Immersion Depth
8
9 # Channel geometry
10 w_c = linspace(0.4,1.6,100)/10 # Width in cm
11 l_c = 20e-3 *100          # Length in cm
12
13
14 M = 18 # Molar Mass of Water
15 L_T = [10,15,20,25] # Ambient Temperature T in C
16 L_pv = [1.23, 1.71, 2.34, 3.17] # Vapor Pressure of Water at different T
17 L_rho = [999.7, 999.1, 998.2,997.0] # Density of Water at different T
18 L_gamma = [74.22e-3, 73.50e-3, 72.75e-3,71.97e-3] # Surface Tension of
    Water at different T
19
20 # Color Map
21 mpl.rcParams['axes.prop_cycle'] = cycler('color', pyplot.cm.viridis(np.
    linspace(0, 1,4)))
22
23 # Figure for plot
24 f = figure(figsize=(8,4))
25 grid(which='both')
26 xlabel('Channel width $w_c$ in mm')
27 ylabel('Evaporation time $t_e$ in minutes')
28 xlim(0.4,1.6)
29 ylim(0,200)
30
31
32 for Tc, pv, rho, gamma in zip(L_T,L_pv,L_rho,L_gamma):
33     T = Tc + 273.15 # to Kelvin
34
35     # Channel wetting geometry
36     r_c = gamma/(rho*g*h_i)
37     h_c = r_c - sqrt(r_c**2 - (w_c/2/100)**2)
38     h_c *= 100
39
40     # Volume and Surface
41     A_c = 2/3*w_c*h_c
42     V_c = A_c*l_c
43     S_c = w_c*l_c
44
```

```

45     # Evaporation Model
46     G = 8.68e-7*(M**0.833*pv**sqrt(vz))*(1/28.97+1/M)**0.25/(z*T**0.05)
47     t_e = V_c*(rho/1000)/(G*S_c)
48
49     # Plot and Annotations
50     plot(w_c*10, t_e/60)
51     plt.text(w_c[-13]*10, t_e[-3]/60, f'T={Tc:2.0f} C')
52
53     f.savefig('evaporation-time.pdf')
54
55
56     # Calculation for Etyhlene Gycol
57     rho = 1113.5      # glycol 1113.5
58     gamma = 48e-3    # glycol 48e-3
59     M = 62           # glycol 62 g/mol
60     pv = 0.01       # glycol at 25C
61     w_c = 1.2/10    # Width in cm
62
63     # Channel wetting geometry
64     r_c = gamma/(rho*g*h_i)
65     h_c = r_c - sqrt(r_c**2 - (w_c/2/100)**2)
66     h_c *= 100
67
68     # Volume and Surface
69     A_c = 2/3*w_c*h_c
70     V_c = A_c*l_c
71     S_c = w_c*l_c
72
73     # Evaporation Model
74     G = 8.68e-7*(M**0.833*pv**sqrt(vz))*(1/28.97+1/M)**0.25/(z*T**0.05)
75     t_e = V_c*(rho/1000)/(G*S_c)
76
77     print(f'hc: {h_c*1e4:3.2f} um')
78     print(f'Vc: {V_c*1e4:3.2f} ul')
79     print(f'Sc: {S_c:3.2f} cm2')
80     print(f'G : {G:3.2e} g/cm2/s')
81     print(f'te: {t_e/60:3.0f} min')

```

Python source code of the evaporation model [82] applied to the microfluidic channels created by a contrast in wettability for Jupyter notebooks. The code displays a plot of the evaporation time of water for different channel widths w_c and ambient temperatures T . For etylene glycol the evaporation of a 1.2 mm wide channel is calculated. The material constants are taken from [2].

A.4 Software Architecture and System components

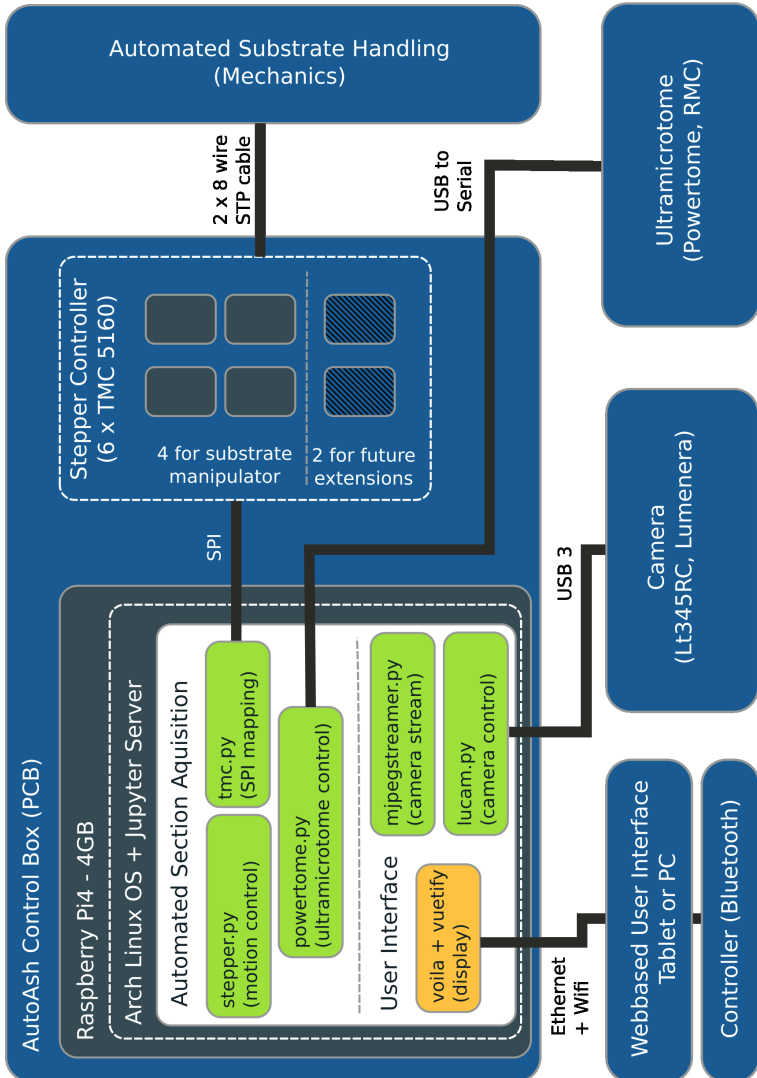


Figure A.3: Software architecture and system components

